La borsa di dottorato è stata cofinanziata con risorse del
PON Ricerca e Innovazione 2014-2020, Asse IV "Istruzione e ricerca per il recupero",
Azione IV.4-"Dottorati e contratti di ricerca su tematiche dell'innovazione"

UNIVERSITY OF CALABRIA

Department of Pharmacy, Health and Nutritional Sciences

PhD Course
Life Science and Technology

With the support of

Macrofarm s.r.l.

CYCLE

XXXVII

Targeting systems for the treatment of infectious diseases

SSD: CHEM-08/A

Coordinator:

Prof. Tommaso Angelone

Tommaso Angelone
25.02.2025
11:58:53
GMT+01:00

Supervisor/Tutor:

Prof. Francesco Puoci

Francesco Puoci
24.02.2025 16:05:55
GMT+01:00

Ph.D. Candidate:

Francesco Patitucci

Dr. Ortensia Ilaria Parisi

Ortensia Ilaria Parisi
24.02.2025 16:43:19
GMT+01:00

CONTENT

INTRODUCTION

Zoonoses are diseases that can be transmitted from vertebrate animals, excluding humans, to people, and they represent a primary source of emerging viruses.[1] Mammals, birds, reptiles, and possibly amphibians can act as reservoirs or amplifying hosts for zoonotic viruses.[2] These viruses often cause few or no evident symptoms in the non-human vertebrates that carry them. Some zoonotic viruses have very limited host ranges, while others can infect a variety of vertebrates. Human infection can range from asymptomatic cases to fatal disease. Viral zoonoses, both new and known, play a crucial role in emerging and re-emerging viral diseases.[3,4]

The transmission of zoonotic viruses can occur through various routes (Figure 1), including "direct contact" (as with rabies virus), "indirect contact" (as with hantavirus), "nosocomial transmission" (as with the Ebola virus), "aerosol transmission" (as with the SARS coronavirus), "vertical transmission" (in utero, as with Zika virus), and "via vectors or arthropods" (such as yellow fever virus and West Nile virus).

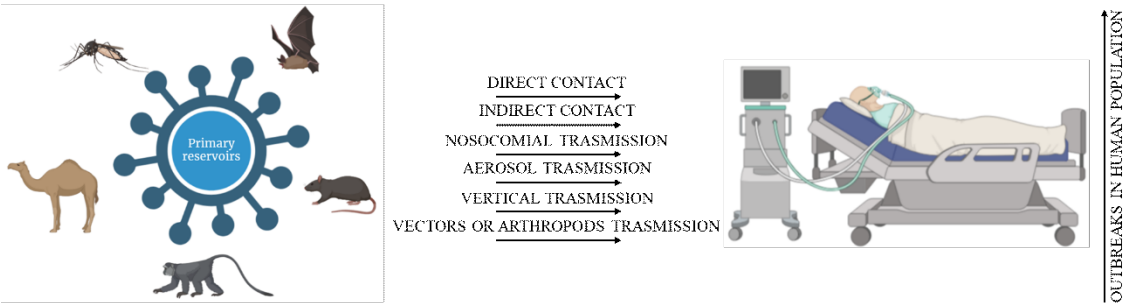

Fig.1 - The transmission of zoonotic viruses

Viral zoonoses occur on every continent, possibly excepting Antarctica, and can spread in a variety of ecological settings or be confined to specific ecological and geographical areas. Although

hundreds of viruses are zoonotic, the significance of many of them has not yet been fully established.[5]

Among the zoonotic viruses most relevant to global public health are those belonging to the flavivirus genus (family Flaviviridae) and the betacoronavirus genus (family Coronaviridae), both of which contribute to the high global burden of vector-borne diseases, which make up over 17% of all infectious diseases and cause more than 700,000 deaths each year.[6,7]

The spread of arthropod vectors and the geographic expansion of flaviviruses into regions with naïve populations can lead to severe outbreaks, such as the Zika virus outbreak in Brazil between 2014 and 2016, during which an estimated 440,000 to 1,300,000 cases occurred in 2015 alone. [8]

Similarly, zoonotic coronaviruses can emerge and spread, as has happened three times in the 21st century, causing the SARS-CoV-1 outbreak in 2003, the MERS-CoV outbreak in 2012, and the SARS-CoV-2 pandemic that began in 2019, which resulted in millions of infections and deaths.[9] Given the potential of flaviviruses and coronaviruses to cause epidemics and pandemics, developing antiviral options to reduce the current and future impact of these pathogens is urgent. Broad-spectrum antivirals would be particularly valuable in countries with multiple circulating flaviviruses and to contain transmission in the early stages of future outbreaks caused by newly emerging coronaviruses.

THE CORONAVIRIDAE FAMILY

The Coronaviridae family includes a range of RNA viruses within the Nidovirales order, known for causing respiratory (Coronavirinae subfamily) and gastrointestinal (Torovirinae subfamily) illnesses in various vertebrates, including mammals and birds.[10] This viral family has attracted significant global attention, especially after notable pandemic events like the severe acute respiratory syndrome (SARS) outbreak in 2002-2003, the Middle East respiratory syndrome (MERS) outbreak in 2012, and most recently, the COVID-19 pandemic in 2019, triggered by SARS-CoV-2.[11] These incidents have underscored the potential of Coronaviridae to cause severe disease, thereby driving scientific research into the pathogenesis, transmission, prevention, and treatment of infections caused by these viruses.

Coronaviruses exhibit significant genetic diversity and are divided into four main genera: Alphacoronavirus and Betacoronavirus, which primarily infect mammals, including humans, and Gammacoronavirus and Deltacoronavirus, which infect mostly birds and some mammals.[12] Among these, Betacoronaviruses include highly pathogenic viruses such as SARS-CoV, MERS-CoV, and SARS-CoV-2, which have led to human epidemics and pandemics. Coronaviridae cause a range of illnesses, from mild respiratory infections similar to the common cold to severe respiratory, hepatic, and neurological diseases.[13]

Coronaviridae's evolutionary origins date back millions of years, suggesting a long-standing co-evolution with their animal hosts. These viruses are known to have an extensive natural reservoir in wild animals, particularly bats and other small mammals, as depicted in Figure 2.

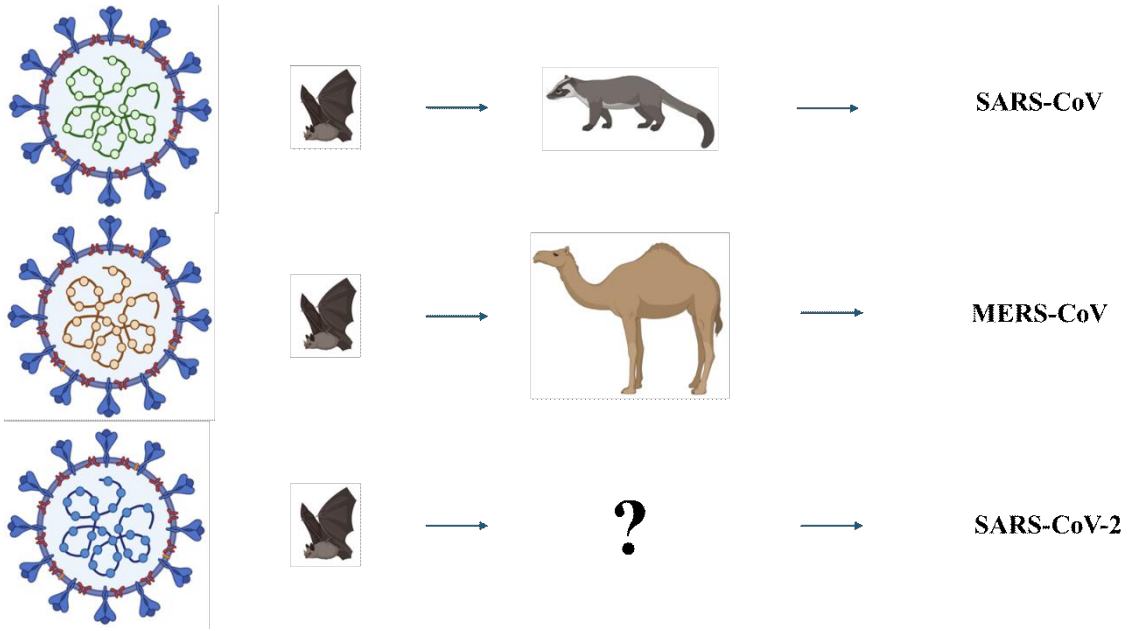

Fig. 2 - Animal origins of human coronaviruses

Bats, in particular, are considered natural reservoirs for several Betacoronaviruses and Alphacoronaviruses, owing to their unique immune and biological features that allow them to coexist with diverse pathogens. Transmission of these viruses from bats to humans or other animals is facilitated by a phenomenon known as spillover, which occurs when a virus crosses species barriers.[14] In some cases, this transition occurs through an intermediate host, as hypothesized for SARS (with the palm civet as an intermediary) and MERS (through camels). SARS-CoV-2, responsible for the COVID-19 pandemic, is presumed to have originated from a bat coronavirus, although the exact pathway to humans is still under study.[15]

Coronaviridae are of particular public health importance due to their capacity to quickly adapt to new hosts and environments. This adaptability stems from the coronaviruses' tendency to genetically recombine and accumulate mutations, which can impact their infectivity, pathogenicity, and immune evasion.[16] Due to these properties, coronaviruses pose a continuous risk of emerging and re-emerging variants capable of causing outbreaks. In the past, human coronavirus infections were relatively benign, causing primarily mild respiratory symptoms, similar to those caused by HCoV-229E and HCoV-OC43, discovered in the 1960s.[17] However, the 2002 SARS outbreak

marked a turning point, demonstrating that coronaviruses have the potential to cause severe infections with high mortality rates. SARS, for example, recorded a mortality rate close to 10%, while MERS in 2012 showed an even higher mortality rate of around 35%.[18] COVID-19 has further highlighted the ability of a coronavirus to cause a pandemic on a global scale, with significant health, economic, and social consequences.

Structure and genome organization

Structurally, viruses in the Coronaviridae family have a complex architecture that is critical for their function and pathogenicity. The structure includes an RNA genome, several structural proteins, and a lipid envelope. The genome of Coronaviridae is composed of positive-sense single-stranded RNA, which can range up to 30,000 nucleotides in length, making it one of the largest known RNA viral genomes. This extensive RNA genome contains multiple open reading frames (ORFs) that encode both structural and non-structural proteins essential for viral replication and assembly. Specifically, the first two-thirds of the genome encodes non-structural proteins that are vital for the replication process, while the remaining segment codes for the four main structural proteins, as shown in Figure 3: the spike protein (S), the membrane protein (M), the envelope protein (E), and the nucleoprotein (N).[19–21]

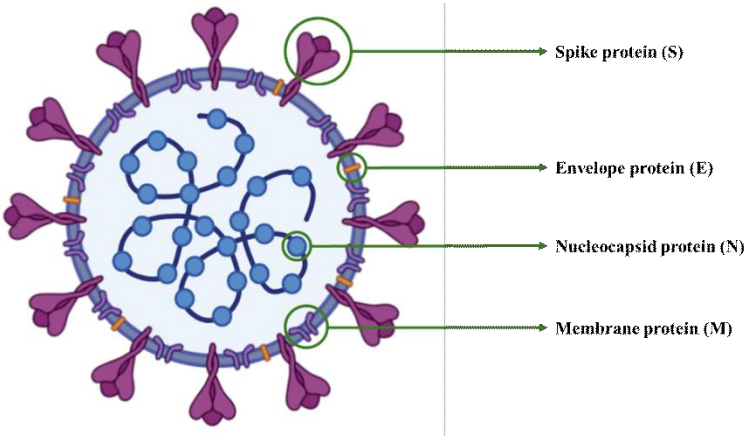

Fig. 3 - Four structural proteins of SARS-CoV-2

The spike protein (S) is a critical component of the coronavirus structure, playing a pivotal role in the virus's ability to enter host cells. It is responsible for binding to specific receptors on the surface of host cells, such as the ACE2 receptor utilized by both SARS-CoV and SARS-CoV-2, and the DPP4 receptor used by MERS-CoV. The binding of the spike protein to these receptors triggers conformational changes that facilitate the fusion of the viral envelope with the host cell membrane, allowing the viral genome to enter the host cell. The membrane protein (M) is the most abundant protein in the virion and is crucial for maintaining the shape and integrity of the virus. The envelope protein (E), although smaller, is essential for the assembly and release of new virions, and it has been shown to play a role in pathogenesis by modulating the host's immune response. Finally, the nucleoprotein (N) binds to the viral RNA, forming a ribonucleoprotein complex that protects the viral genome and is involved in regulating RNA synthesis during replication.[22–24]

Coronaviruses have a characteristic spherical or slightly ovoid shape, typically measuring between 80 and 120 nanometers in diameter.[25,26] This shape is maintained by the nucleocapsid and lipid envelope, which is derived from the host cell during the budding process. The presence of spike proteins on the virion's surface gives it a distinctive crown-like appearance when viewed under an electron microscope, which is where the name "coronavirus" originates.[27,28] The lipid envelope makes coronaviruses sensitive to lipid solvents, which can disrupt the envelope and inactivate the virus, highlighting the importance of proper sanitation practices in controlling viral transmission.

Life cycle

The life cycle of Coronaviridae involves several well-defined stages: attachment, fusion, transcription and translation, assembly, and release.[20] The process begins when the virus attaches to the host cell via the interaction between the spike protein and specific cell surface receptors. Once bound, the spike protein undergoes a conformational change that enables fusion of the viral envelope with the host cell membrane. This spike protein, which is 1273 amino acids long, consists

of two subunits: S1 (residues 14–685), which houses the N-terminal domain (NTD, residues 14–305) and receptor-binding domain (RBD, 319–541) essential for receptor recognition, and S2 (residues 686–1273), responsible for membrane fusion. S2 contains the fusion peptide (FP, residues 788–806), heptad repeat sequences HR1 (912–984) and HR2 (1163–1213), and the transmembrane (TM) domain (1213–1237).[20,29,30] This trimeric protein forms a crown-like structure around the viral particle, giving the virus its characteristic appearance, and allows the viral RNA to enter the host cell's cytoplasm. Inside the host cell, the positive-sense RNA genome can act directly as messenger RNA (mRNA), which is translated by the host's ribosomes to produce viral proteins. This initial translation produces a large polyprotein that is cleaved by viral proteases into smaller functional proteins, including the essential RNA-dependent RNA polymerase (RdRp). The RdRp is crucial for the replication of the viral RNA, allowing for the synthesis of new viral genomes and subgenomic RNAs, which encode the structural proteins needed for the formation of new virions.[31,32] As viral proteins are synthesized, they begin to accumulate in the cytoplasm, where the nucleoprotein (N) binds to the newly replicated RNA genomes, forming ribonucleoprotein complexes. Simultaneously, the structural proteins (S, M, E) are transported to the endoplasmic reticulum and the Golgi apparatus, where they are processed and assembled into new viral particles. The assembly process is highly coordinated, as the nucleocapsids formed by the nucleoprotein and RNA genome interact with the membrane proteins to create new virions.[31–33] Finally, the newly assembled virions are transported in vesicles to the host cell's surface, where they are released into the extracellular environment by exocytosis. This release process can lead to the lysis of the host cell, contributing to tissue damage and the clinical symptoms associated with coronavirus infections. [31–33]

Associated Symptoms and Diseases

The Coronaviridae family primarily spreads through respiratory routes, although transmission can also occur via direct contact with contaminated surfaces.[34] Airborne transmission happens mainly through respiratory droplets produced when an infected individual speaks, coughs, or sneezes; these droplets can be inhaled by nearby individuals, facilitating the spread of the virus.[35] Additionally, coronaviruses can persist on inanimate surfaces for varying durations depending on environmental conditions, which enables potential indirect transmission. Research indicates that SARS-CoV-2, the virus responsible for COVID-19, can remain infectious on surfaces such as plastic and stainless steel for several hours to even days.[36,37] Another mode of transmission includes direct contact with infected animals or consumption of contaminated wild animal meat, as seen in the SARS outbreak, where civets are believed to have been a significant source of infection.[38] In the case of MERS, transmission primarily occurred through contact with dromedary camels, emphasizing the need for monitoring zoonotic spillover events that pose a risk to human health.[39] The interaction of humans with wildlife, practices related to intensive farming, and the exotic animal trade all contribute to creating favourable conditions for such transmissions to occur.

The clinical manifestations of viruses in the Coronaviridae family vary significantly based on the specific type of coronavirus involved and the host's response to the infection. The most common symptoms associated with these viruses include fever, cough, respiratory difficulty, and fatigue. Generally, most coronavirus infections result in mild illnesses that resemble the common cold, but in certain cases, they can lead to severe clinical manifestations such as pneumonia, severe acute respiratory syndrome (SARS), and respiratory failure.[40] In the case of SARS, initial symptoms can include high fever, general malaise, and respiratory symptoms that can progress to interstitial pneumonia, potentially leading to respiratory failure and death. Conversely, MERS is associated with a higher mortality rate, and while it can present with similar symptoms to SARS, it is

frequently accompanied by more severe respiratory illnesses and renal complications, with mortality rates exceeding 30%.[41–44]

COVID-19, caused by SARS-CoV-2, has exhibited a wide range of symptoms, from asymptomatic cases to severe manifestations that can include pneumonia, thromboembolism, and acute respiratory distress syndrome (ARDS). Patients may also experience additional symptoms, such as loss of taste and smell, muscle pain, diarrhea, and nasal congestion. The variability in symptoms makes the diagnosis and management of coronavirus infections a complex challenge for healthcare professionals.[40,45]

Currently Available Therapies

The treatment of infections caused by viruses from the Coronaviridae family, which includes SARS-CoV, MERS-CoV, and SARS-CoV-2, necessitates a multifaceted approach that incorporates various pharmacological therapies and clinical protocols to manage symptoms and improve patient outcomes. Following the emergence of the COVID-19 pandemic, scientific research has accelerated the development of new treatments and antiviral therapies, which have proven crucial in combating the virus.[46] Initially, remdesivir emerged as one of the most promising drugs for treating COVID-19. This antiviral, initially designed to combat Ebola, has demonstrated efficacy in inhibiting viral replication by targeting the RNA polymerase enzyme, thus reducing the duration of the illness and the hospitalization rate among patients with moderate to severe COVID-19. Clinical studies have highlighted that, when administered early, remdesivir can significantly enhance clinical outcomes and decrease recovery time. However, the results have not been uniform, leading to debates regarding its effectiveness, particularly in the advanced stages of the disease.[47,48]

In addition to remdesivir, several other antiviral drugs have been approved or are currently undergoing testing. For instance, protease inhibitors, such as nirmatrelvir, have been developed for

COVID-19 treatment and are used in combination with ritonavir to enhance therapeutic efficacy. These drugs aim to inhibit the virus's ability to replicate within human cells, thereby reducing viral load and, consequently, the severity of the disease. The combination of antiviral agents may represent a promising strategy to address the health emergency, as it can help lower the likelihood of viral resistance.[49,50]

Monoclonal antibody therapies have also gained significant importance in the treatment of COVID-19, especially for patients at high risk of developing severe complications. Monoclonal antibodies are designed to recognize and bind to specific viral proteins, neutralizing the virus and preventing it from attaching to human cells.[51,52] Drugs such as casirivimab and imdevimab, developed by Regeneron, have shown to reduce the risk of hospitalization and death among patients receiving early COVID-19 diagnoses. Similarly, Eli Lilly's monoclonal antibody (bebtelovimab) treatment has demonstrated comparable efficacy.[53,54] However, the effectiveness of these therapies can vary depending on emerging viral variants, prompting researchers to develop new antibodies capable of addressing viral mutations. The use of monoclonal antibodies has represented a rapid and flexible therapeutic response, demonstrating the possibility of utilizing targeted approaches to combat viral infection, particularly in the early stages of the disease.

Regarding infections caused by MERS-CoV and SARS-CoV, the therapeutic landscape is more complex, as there are currently no approved specific antivirals for these viruses.[55] Treatment options are primarily supportive, focusing on assisting patients with respiratory failure and managing complications. Mechanical ventilation and oxygen therapy are often required for patients with severe respiratory distress, while monitoring for secondary infections is essential, as these patients may be more susceptible to bacterial infections. Research remains active in this field, with clinical studies evaluating existing antiviral drugs and new immunological therapies aimed at identifying effective treatments for MERS and SARS.

An important aspect of combating coronavirus infections is the exploration of combination therapies that integrate antivirals and monoclonal antibodies to maximize therapeutic effectiveness. Drug combinations can help rapidly reduce viral load and prevent the emergence of resistant variants. Additionally, the potential for developing oral treatments that can be administered to outpatient populations represents a significant area of interest, as it would facilitate quicker and easier access to therapies, ultimately improving overall patient outcomes.[56,57]

While preventive measures are not the primary focus of this section, it is important to note that the success of treatments is amplified by effective prevention strategies. Vaccination remains essential for reducing virus transmission and disease severity. Vaccines, such as mRNA vaccines (Pfizer-BioNTech and Moderna) and vector-based vaccines (AstraZeneca and Johnson & Johnson), have been critical in controlling the pandemic, demonstrating high efficacy in reducing the risk of infection and severe consequences.[58,59]

THE FLAVIVIRIDAE FAMILY

Flaviviruses represent a highly significant group of viruses due to their medical and veterinary relevance, as they are responsible for numerous infectious diseases that affect both humans and various other animals.[60]

Flaviviruses encompass a variety of viruses primarily transmitted by arthropods, particularly mosquitoes and ticks, which act as biological vectors.[61] This mode of transmission highlights the complex interactions between the viruses, their hosts, and the environments in which they circulate. Among the most relevant flaviviruses for human health are [62,63]:

- Dengue Virus (DENV), which is responsible for widespread epidemics in tropical and subtropical regions and can lead to forms of disease ranging from mild dengue fever to severe dengue hemorrhagic fever;
- Zika Virus (ZIKV), which gained global attention due to its rapid spread during the 2015-2016 outbreak and its association with severe congenital malformations, including microcephaly;
- West Nile Virus (WNV), predominantly found in Africa, the Middle East, and Asia, and more recently in North America and Europe, which can cause severe neurological disease such as encephalitis in immunocompromised individuals and the elderly;
- Japanese Encephalitis Virus (JEV), endemic in East and Southeast Asia and the leading cause of viral encephalitis in many countries in this region;
- Yellow Fever Virus (YFV), responsible for a severe hemorrhagic disease, for which there is an effective and widely used vaccine that has significantly reduced incidence rates in endemic areas.

In addition to these flaviviruses affecting humans, there are several that impact animals, which can have direct implications for veterinary health and agriculture. For example, the Kyasanur Forest disease virus is found in southern India and primarily affects livestock, leading to significant economic losses in the agricultural sector. Wesselsbron virus, on the other hand, mainly infects livestock in Africa, emphasizing the veterinary significance of the Flaviviridae family. These viruses not only threaten animal health but also have the potential to spill over into human populations, creating additional public health challenges.[63]

Flaviviruses are among the leading causes of emerging and re-emerging infectious diseases, with major impacts on global public health, as their spread is heavily influenced by vectors and environmental factors. Tropical and subtropical areas are particularly vulnerable to mosquito-borne flaviviruses such as dengue and Zika, which propagate rapidly due to factors like urbanization, population density, globalization, and climate change. The expansion of urban areas provides ideal breeding grounds for mosquitoes, while global travel and trade facilitate the movement of both vectors and viruses, increasing the risk of outbreaks in new regions. Recently, even regions like Europe and North America, which were previously considered low-risk for these viruses, have reported outbreaks, illustrating the changing epidemiology of flavivirus infections.[64,65]

The history of flavivirus discovery is long and complex, beginning with the identification of yellow fever virus in the late 19th century, which was the first virus ever described to infect humans.[66] Other family members were identified in the 20th century, including Japanese encephalitis virus and West Nile virus, during periods of significant public health interest. Advances in molecular biology technologies, such as polymerase chain reaction (PCR) and next-generation sequencing, along with global surveillance systems, have facilitated the identification of new flaviviruses and improved our understanding of their transmission methods and pathogenic mechanisms.[67–69]

Structure and genome organization

Flaviviruses are RNA viruses distinguished by their unique morphology, which is critical to their ability to infect host cells.[70–72] The viral particle, or virion, typically has a spherical shape and measures about 40-60 nm in diameter.[73] The flavivirus genome's structure and organization play a crucial role in their biology and ability to cause disease. Measuring between 10 and 11 kb in length, the genome is organized as a polyprotein, which is initially translated into a single polypeptide chain. This chain is then cleaved into multiple structural proteins, such as the capsid (C), premembrane (prM), and envelope (E) proteins (Figure 4), as well as non-structural proteins, including NS1, NS2A, NS2B, NS3, NS4A, NS4B, and NS5.[74,75]

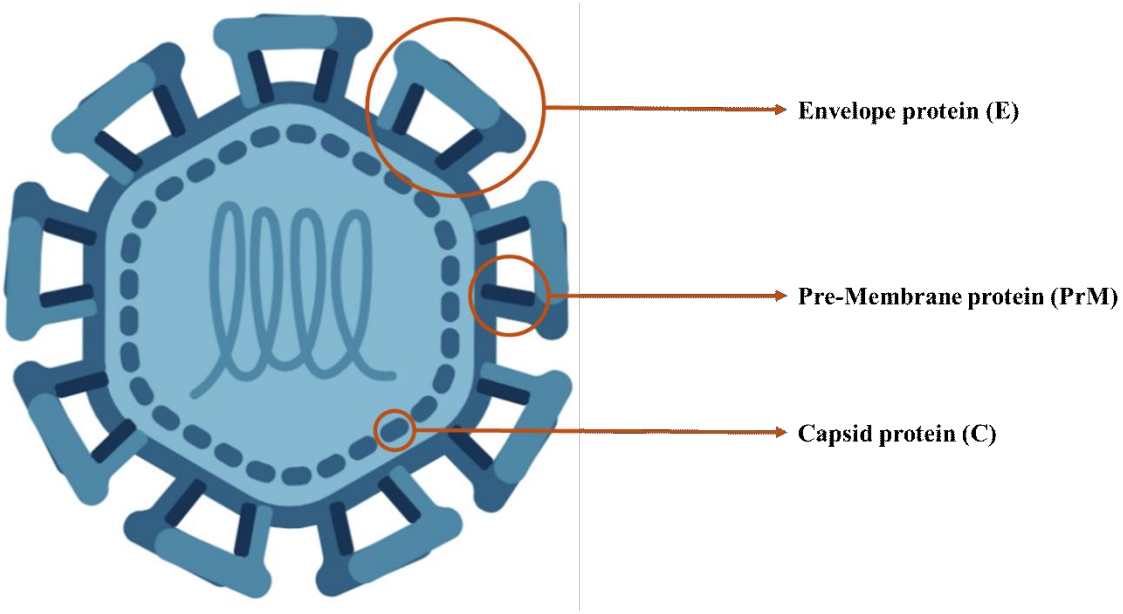

Fig. 4 - Structural proteins of Flavivruses

The viral capsid, primarily composed of the C and prM proteins, is responsible for encapsulating and protecting the viral genome. The C protein is essential for the stability of the capsid, as it associates with the viral RNA to form the nucleocapsid, a structure crucial for the stability and integrity of the virus. Additionally, the C protein is localized not only in viral replication organelles but also in the nucleolus and lipid bodies, suggesting a role in multiple cellular functions, including the modulation of viral replication.[76–78] The prM protein, on the other hand, plays a crucial role

in the assembly and maturation of the virus, associating with the E protein to form a complex that is essential for proper virion formation. During the maturation process, prM is cleaved by the viral protease, adopting a form that allows the virus to exit the host cell.[79] Furthermore, prM interacts with various cellular factors, suggesting its involvement in modulating the host's immune responses.[80]

The envelope protein (E) of flaviviruses plays a vital role in the virus's infection and pathogenicity. This protein is the main component of the virion surface and is crucial for host recognition, receptor binding, and cellular entry.[81,82] The E protein is found as a dimer on the virion surface, and its structure is highly conserved across different members of the Flaviviridae family, indicating its evolutionary significance. The E protein's three-dimensional structure features a "herringbone" pattern, which helps stabilize the virion and facilitates interactions with cellular receptors.[83] A notable characteristic of the E protein is its ability to undergo conformational changes in response to pH shifts, a crucial step in membrane fusion during viral entry into the host cell. These changes are driven by histidine residues that act as pH sensors, allowing the E protein to adapt to the changing environment during the viral lifecycle.[84] Another key step in virion maturation is the cleavage of the premembrane protein (prM) by furin, which impacts the functionality of the E protein and the virus's ability to infect cells. Inefficient cleavage of prM can lead to the formation of structurally diverse virions, which possess unique antigenic and functional properties.[85] Moreover, the E protein is involved not only in viral entry but also in modulating the host immune response. Its interactions with neutralizing antibodies are an area of active study, as understanding these interactions could aid in developing vaccines and antiviral treatments.[82] The E protein is also a target for the innate immune response, and its ability to evade this response is crucial for the virus's survival within the host.[86,87] Recent research has shown that the E protein interacts with other viral proteins and cellular factors, suggesting that its function goes beyond facilitating viral entry. For instance, the E protein interacts with the NS2A protein, which is involved in virion assembly,

emphasizing the importance of protein-protein interactions for the production of infectious viral particles.[88] These interactions may affect the stability of the virion and its ability to infect host cells, making the E protein a central player in flavivirus biology.

The non-structural proteins—such as NS1, NS2A, NS2B, NS3, NS4A, NS4B, and NS5—play important roles in RNA replication and in evading the host's immune defenses. Specifically, the NS5 protein is the most conserved among flaviviruses and is integral to genome replication, while the NS1 protein is key in modulating the immune response and contributing to pathogenesis.[89,90]

The 5' and 3' ends of the genome exhibit distinctive features. The 5' end contains a cap that aids in translation and protects the genome from degradation, while the 3' end has a polyadenylated tail that enhances RNA stability and translation. These regulatory sequences are crucial for the replication and translation of the viral genetic material, facilitating efficient protein synthesis within the host. Moreover, the presence of replication sequences and other regulatory elements within the genome allows the virus to optimize its life cycle and respond quickly to environmental changes and immune pressures.[91–93]

Life cycle

The replication cycle of flaviviruses consists of a series of intricate and well-coordinated steps: attachment, penetration, replication, and release of viral particles. Understanding these steps is crucial to grasp how these viruses successfully infect host cells and evade the immune responses of the body.

The first step in the replication cycle is attachment. During this stage, flaviviruses bind to specific receptors located on the surface of host cells. This interaction is primarily facilitated by the viral E protein, which is essential for binding to cellular receptors. Flaviviruses recognize and attach to receptors such as the platelet-derived growth factor receptor (PDGFR) and the DC-SIGN (dendritic

cell-specific intercellular adhesion molecule-3-grabbing non-integrin) receptor.[94,95] These receptors play a vital role not only in the initial attachment but also in the subsequent internalization of the virion into the host cell, primarily mediated by endocytosis, a mechanism that enables the cell to engulf extracellular materials into vesicles.[96]

Once the virus has attached to the receptor, the next phase is penetration. In this process, the virion is taken up by the host cell through endocytosis. During this stage, the cell membrane wraps around the virion, creating an endocytic vesicle that transports the virion into the cell. Inside the vesicle, changes in pH trigger a conformational alteration in the E protein, enabling the viral envelope to merge with the vesicle membrane.[97] This fusion is critical for the release of the viral genome and proteins into the cytoplasm of the host cell.[98]

Once released into the cytoplasm, the single-stranded viral RNA genome initiates the replication phase, serving both as mRNA for protein synthesis and as a template for its own replication.[99] Translation of the genome produces a long polypeptide, which is cleaved by viral proteases into structural and non-structural proteins. RNA replication occurs within replication complexes located on the membranes of the endoplasmic reticulum, where the viral genome is duplicated. During this stage, viral non-structural proteins (NS), such as NS2A and NS5, play essential roles as enzymes in genome replication and contribute to the assembly of viral particles.[100,101] Specifically, NS5 is crucial for RNA replication and modulating the host immune response, making it a promising target for antiviral therapy development.[102] This highly efficient process enables the virus to produce numerous copies of its genome and to assemble viral particles within a short timeframe.

The assembly of viral particles occurs in the lumen of the endoplasmic reticulum (ER), where structural proteins like prM and E encapsulate the nucleocapsid.[103] This process is tightly regulated and relies on interactions with cellular components, including factors from the secretory pathway. Immature particles then undergo maturation in the Golgi, where the furin enzyme cleaves the prM protein, a critical step for producing infectious virions, as the maturation of the E protein is

necessary for viral infectivity.[104] The mature virions are subsequently transported through the Golgi and released via exocytosis into the extracellular environment. Proteins such as ESCRT (Endosomal Sorting Complex Required for Transport) may facilitate membrane scission during this release. This stage is closely linked to the morphology of the ER and its interaction with the Golgi, highlighting the manipulation of cellular trafficking pathways as a key aspect of flavivirus pathogenesis.[105] During the release phase, the structural proteins and viral genome assemble to form virions, which acquire a lipid envelope through budding as they exit the host cell, enabling the infection of new cells and the continuation of the viral replication cycle.[97,106]

Associated Symptoms and Diseases

Flaviviruses are responsible for a variety of infectious diseases that differ significantly in severity and clinical manifestations. Among the most well-known flaviviruses are dengue virus (DENV), Zika virus (ZIKV), Japanese encephalitis virus (JEV), West Nile virus (WNV), and yellow fever virus (YFV). These viruses are primarily transmitted by arthropods, such as mosquitoes and ticks, and their infections can present with a range of symptoms, from asymptomatic cases to severe and potentially fatal illnesses.[107–109]

Dengue virus, for instance, is responsible for dengue, a disease that can present in various forms. The most common form is dengue fever (DF), characterized by high fever, muscle and joint pain, rash, and, in some cases, bleeding. However, in certain patients, the disease can progress to severe forms like dengue hemorrhagic fever (DHF) or dengue shock syndrome (DSS), both of which can lead to circulatory shock and death.[110–112] The severity of the disease is influenced by several factors, including the virus serotype and the host's immune response. Reinfection with a different serotype can increase the risk of developing severe disease due to a phenomenon known as antibody-dependent enhancement.[113,114]

Initially considered relatively mild, Zika virus gained global attention due to its association with serious neurological complications, such as Guillain-Barré syndrome and congenital malformations like microcephaly in babies born to mothers infected during pregnancy.[115,116] ZIKV infection symptoms can include fever, rash, conjunctivitis, and joint pain, though many cases are asymptomatic, making epidemiological surveillance challenging.[117,118]

Japanese encephalitis virus is another clinically significant flavivirus, responsible for severe encephalitis in certain parts of Asia. The disease can present with severe neurological symptoms, including high fever, neck stiffness, confusion, and coma. The mortality rate associated with Japanese encephalitis is high, and survivors may experience permanent neurological disabilities.[119,120]

West Nile virus, endemic in many parts of the world, can cause a flu-like illness, but in some cases, it can progress to severe forms like encephalitis and meningitis. Symptoms can include fever, headache, muscle pain, and, in more severe cases, neurological signs such as confusion and paralysis.[121,122]

Finally, yellow fever virus, transmitted by infected mosquitoes, can cause an acute illness with fever, chills, headache, and muscle aches. In some cases, the disease can progress to a severe hemorrhagic form with a high mortality rate.[123,124]

Currently Available Therapies

The treatment of infections caused by flaviviruses poses significant challenges, primarily due to their viral nature, which limits available therapeutic options. Currently, most treatments are symptomatic, aimed at alleviating symptoms and improving patient comfort rather than eradicating the infection itself. For instance, in cases of dengue fever, treatment focuses on managing fever and pain through the use of analgesics and antipyretics, while it is crucial to avoid medications like

aspirin and non-steroidal anti-inflammatory drugs (NSAIDs), which can increase the risk of bleeding.[125] For other infections, such as Zika virus, no specific antiviral treatments exist, and care is limited to supportive measures to address symptoms like fever and rashes.[126] Moreover, the emergence of Zika virus as a public health concern has underscored the importance of understanding the disease's implications, particularly in pregnant women, where infection can lead to severe congenital abnormalities such as microcephaly.[127] This has led to increased scrutiny of Zika virus infections and the necessity for effective public health responses, including education on symptom management and the avoidance of mosquito bites. [128]

In recent years, there has been a growing interest in researching specific antivirals for flaviviruses. Studies have been conducted on various compounds showing antiviral activity against dengue, Zika virus, and other flaviviruses. These investigations aim to identify drugs that can interfere with the viral replication cycle or modulate the host's immune response.[129–131] However, the path to approval of new antivirals is complex and requires extensive clinical studies to evaluate the effectiveness and safety of these drugs.[132]

Preventing flavivirus-related diseases is a public health priority and primarily relies on vaccination and vector control measures. Currently, effective vaccines are available against certain flaviviruses, such as the yellow fever vaccine, which is highly effective and recommended for individuals traveling to endemic areas. The yellow fever vaccine is a live attenuated vaccine that provides long-lasting protection after a single dose, helping to control the disease's spread in many tropical regions.[133,134]

Regarding dengue fever, vaccines have been developed that have shown promising results in clinical trials. The Dengvaxia vaccine, for example, has been approved in some countries for use in individuals who have already had a dengue infection, as its use in naive individuals could pose risks of severe complications in the event of subsequent infections.[135,136] The challenge in developing vaccines against other flaviviruses, such as Zika virus and Japanese encephalitis virus, lies in the

need for a durable immune response and the prevention of adverse reactions.[137,138] Furthermore, the genetic heterogeneity among various viral strains complicates the creation of a universal vaccine.

MOLECULAR RECOGNITION

Molecular recognition is the process by which two or more molecules specifically bind to one another.[139] This phenomenon is crucial in biological systems as it governs essential interactions between proteins, nucleic acids, and sugars that participate in vital biological reactions. The ability of molecules to recognize each other was initially described by the "lock-and-key" model proposed by Emil Fischer in 1894, which suggested that only geometrically complementary shapes could perfectly fit together.[140] Later, in 1958, Daniel Koshland developed the induced fit model, emphasizing that enzymes have flexibility, allowing the active site to reshape during interactions with substrates.[140]

Over time, this concept was used to explain molecular self-assembly, laying the foundation for supramolecular chemistry, a branch of chemistry that studies the formation of unique structural complexes through non-covalent and reversible interactions, such as the host-guest (HG) interaction. In this type of chemistry, host and guest molecules bind through interactions like π-π stacking, electrostatic interactions, and hydrogen bonds.[141] The effectiveness of these interactions depends on the complementarity between binding sites, the pre-organization of the host's conformation, and the cooperativity of binding units. HG chemistry has been widely used to develop synthetic receptors capable of recognizing specific guest molecules.[142,143]

Since the late 1960s, supramolecular chemistry has given rise to compounds such as crown ethers, cryptands, and cyclodextrins, primarily used for binding metal cations. Crown ethers, discovered by Charles Pederson in 1967, are cyclic compounds consisting of ethylene bridges separated by oxygen atoms, while cryptands, introduced by Jean-Marie Lehn in 1969, represent a three-dimensional

version of these rings. Another important example is cyclodextrins, cyclic oligosaccharides that form hydrophobic cavities capable of hosting molecules.[144,145]

The development of this discipline has led to fundamental discoveries, recognized with the Nobel Prize in Chemistry in 1987, awarded to Cram, Lehn, and Pederson for the development of molecules with highly selective interactions. In recent decades, supramolecular chemistry has contributed to various fields such as sensors, nanotechnology, medicine, and molecular machines, with recent research recognized in 2016 with another Nobel Prize awarded to Sauvage, Stoddart, and Feringa for their work on molecular machines.[146,147]

Molecularly Imprinted Polymers

Molecular recognition is fundamental in many biological processes, enabling organisms to interact with their environment through specialized receptors. Natural receptors, such as antibodies, are capable of recognizing and binding to a diverse range of both endogenous and foreign molecules, facilitating various biological functions from immune response to cellular signaling.[148] However, while these biological entities exhibit high specificity and sensitivity, they often come with significant limitations, including varying stability under different environmental conditions and complex production processes.[149–152] To address these challenges, the field of synthetic chemistry has evolved to develop molecularly imprinted polymers (MIPs), which offer a promising alternative for creating robust materials capable of selective molecular recognition.[153–155]

The concept of molecular imprinting can be traced back to the early 20th century, with foundational contributions from researchers who laid the groundwork for understanding how specific interactions can be mimicked in synthetic systems. The pioneering work of Polyakov in 1931 marked a significant milestone in this field. He investigated the polymerization of silica and observed that the incorporation of various solvents during this process affected the adsorption properties of the

resulting silica gel. This early observation highlighted the potential of using template molecules to influence the structure and properties of synthetic materials. Polyakov's findings suggested that the presence of a template molecule could create specific binding sites within a polymer matrix, leading to selective recognition capabilities.[156]

Building upon this foundation, Dickey advanced the concept of molecular imprinting in 1949 by developing silica-based adsorbents with specific affinities for organic dyes. His work involved synthesizing silica in the presence of template dye molecules, which would later be removed to leave behind recognition sites shaped like the original dyes. Dickey’s experiments demonstrated that these imprinted silica materials exhibited a pronounced selectivity towards the corresponding dye molecules, akin to the selective binding observed in natural antibody-antigen interactions. This seminal study illustrated the viability of synthetic methods for creating materials with tailored recognition properties.[157]

The historical progression of molecular imprinting continued with further explorations into the mechanisms of recognition. In the 1940s, Linus Pauling proposed theories of antibody diversity, emphasizing the role of specific three-dimensional configurations of antibodies in their interactions with antigens. Pauling's insights provided a theoretical framework for understanding how synthetic polymers could mimic these complex biological processes. The idea of utilizing template molecules to construct binding sites that closely resemble the original target became a focal point for researchers in the subsequent decades.[158]

In the 1970s, the field of molecular imprinting saw significant advancements with the introduction of covalent and non-covalent approaches. Wulff and Sarhan were among the first to demonstrate the potential of covalent imprinting, where functional monomers formed covalent bonds with the template. This method aimed to create a more homogeneous population of binding sites within the polymer matrix, thereby enhancing affinity and binding capacity. However, despite its advantages,

the covalent approach was limited by the restricted range of functional groups that could participate in reversible covalent bonding.[159]

Conversely, the introduction of non-covalent imprinting by Mosbach in the 1980s broadened the scope of molecular imprinting techniques. This approach allowed for the formation of pre-polymerization complexes between the template and functional monomers through non-covalent interactions, such as hydrogen bonds and electrostatic forces. The flexibility inherent in non-covalent methods opened new avenues for utilizing a wider variety of functional groups and templates, including larger biomolecules like proteins and even whole cells. This expanded the potential applications of MIPs significantly, leading to their adoption in various fields such as diagnostics, drug delivery, and environmental sensing.[160–162]

Despite the promising advancements, the field of molecular imprinting faced challenges related to the stability and reproducibility of silica-based imprints. Researchers recognized that silica particles could lose their "memory" of the template over time, leading to decreased selectivity and binding efficiency.[163] This limitation sparked interest in developing more stable and reproducible materials using organic polymers. The quest for improved stability led to innovations in the synthesis of MIPs, ultimately culminating in the development of more reliable synthetic methods.

Recent advancements in molecular imprinting technologies have continued to refine the process of creating MIPs. Controlled free radical polymerization techniques, such as atom-transfer radical polymerization (ATRP) and reversible addition-fragmentation chain transfer (RAFT), have been employed to enhance the precision and control over the synthesis of MIPs. These techniques facilitate the production of well-defined polymer networks with specific binding sites that can exhibit high selectivity and affinity for target molecules.[164,165]

Synthesis

The synthesis of molecularly imprinted polymers (MIPs) represents a highly developed technique for creating materials with recognition sites specific to a particular target molecule, called the "template".[166] The MIPs (Molecularly Imprinted Polymers) synthesis process can be divided into three main phases, as shown in Figure 5. The first phase is the pre-polymerization, in which the template molecule interacts with the functional monomers, forming a complex. During this phase, the monomers selectively bind to the template's structure, setting up the ideal conditions for the formation of the final polymer. The second phase is polymerization, where the monomers polymerize in the presence of the template and a cross-linking agent. This process results in the formation of a three-dimensional polymer network that retains the template's structural memory. Finally, in the third phase, the template is removed. This step is crucial as it allows for the creation of a polymer with specific cavities capable of selectively recognizing and binding the template or similar molecules.

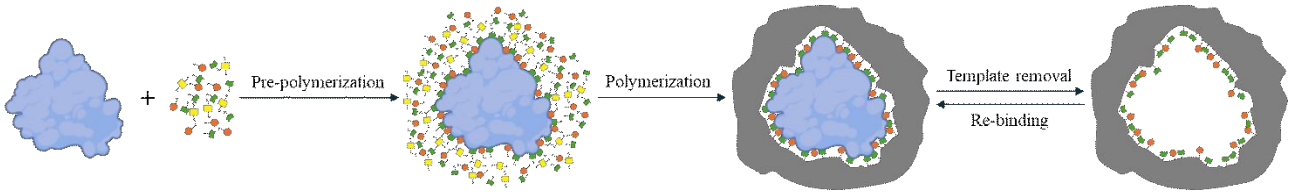

Fig. 5 - Molecular imprinting mechanism

The main methods for synthesizing MIPs can be divided into two approaches: covalent and non-covalent, each with distinct advantages and disadvantages in terms of interactions between the functional monomer and the template.

Covalent Approach

The covalent approach was developed in the early 1970s by Wulff and Klotz and is based on the formation of reversible covalent bonds between the template and the polymer's functional

monomers.[159] This strategy involves the formation of strong and stable complexes involving the template and the surrounding polymer through covalent bonds, such as carboxylic or boronic acid esters, boronate esters, ketals, and Schiff bases (imines). After polymerization, these covalent bonds must be cleaved through acid hydrolysis to remove the template and free the recognition sites within the polymer. Subsequently, the polymer can be regenerated through the reformation of these covalent bonds during the rebinding phase.[167] A variation of this method involves metal complexation, where the template and matrix form a metal complex, similar to immobilized metal affinity chromatography (IMAC) techniques, which are particularly useful for adsorbing proteins containing histidines located on their surface.[168]

One of the main advantages of the covalent approach lies in the robustness of covalent bonds, ensuring a uniform distribution of recognition sites in the polymer and reducing non-specific interactions. However, this approach has some limitations, such as the difficulty in achieving proper thermodynamic equilibrium and the consequently limited ability to recognize only a few types of target molecules, such as alcohols, aldehydes, ketones, amines, and carboxylic acids.[153,169]

Non-covalent Approach

The non-covalent approach is based on weak interactions between the template and the functional monomers, such as hydrogen bonds, ionic interactions, Van der Waals forces, and dipole-dipole interactions.[170] This strategy, primarily developed in the 1990s, allows for a wide range of potential interactions and considerable versatility in the use of functional monomers. In this case, interactions between the template and the monomer spontaneously form before polymerization and are sterically fixed within the polymer during the cross-linking process. After the template is removed by washing, the polymer presents a macroporous matrix with specific recognition sites that can rebind the template or similar molecules.[171,172]

The non-covalent approach is widely used for its simplicity and its ability to create polymers capable of recognizing a broad range of target molecules. However, the weakness of non-covalent interactions requires the use of an excess of functional monomers to promote the formation of the pre-polymerization complex, which can lead to the creation of non-selective binding sites.[153]

An evolution of these techniques is the semi-covalent approach, introduced by Whitcombe, where the pre-polymerization phase involves covalent bonds, but recognition occurs through non-covalent interactions. This method allows combining the high affinity of covalent pre-polymerization with the binding speed typical of non-covalent interactions.[173]

Polymerization Techniques

Various polymerization methods have been employed for the synthesis of Molecularly Imprinted Polymers (MIPs) (Table 1). The most traditional technique is free radical polymerization, which requires heat or light to initiate the process.[174] Several monomers are suitable for this method; however, it often results in the formation of highly branched, atactic MIPs with low binding specificity and selectivity.[175] This is due to the inability to control the propagation and termination phases, leading to a high polydispersity index.[174] For this reason, controlled radical polymerization has become favored over free radical polymerization[176], as it is a more versatile set of reversible deactivation radical polymerization techniques (such as atom transfer radical polymerization[177], reversible addition-fragmentation chain transfer[178], nitroxide-mediated polymerization[179], and iniferter-mediated polymerization[180]) that allow for better control over molecular weight distribution and stereochemistry, though they do not control the size of the synthesized nanoparticles. Today, the most commonly used techniques for nanogel synthesis include precipitation polymerization, emulsion polymerization, and core-shell polymerization followed by grafting.[181–184]

Technique	Mechanism	Advantages	Disadvantages
Free radical polymerization[174]	Free radical polymerization triggered by heat or light	Ease; wide choice of monomers	Low binding specificity and selectivity
Controlled radical polymerization[176–179]	Deactivation radical polymerization	Control of molecular weight distribution and stereochemistry	Lack of control of the nanoparticles size; high vulnerability to impurities and moisture; limited range of suitable monomers
Precipitation polymerization[185]	The formation of polymer chains from monomers and oligomers continues until their size makes them precipitate	Uniform nanoparticles in a single-step reaction; need of a low amount of reagents required	Long time required; need of a high amount of template and solvent
Emulsion polymerization [186]	Polymerization in emulsions in the presence of a surfactant	High yield; suitability to protein imprinting	Required purification; use of a stabilizer
Core-shell grafting + polymerization[187–194]	Polymerization occurs around preformed nanoparticles	Control on MIPs size	Not effective for bulky templates
Solid-phase synthesis[195,196]	Polymerization follows the immobilization of the template molecule on glass beads	Very high affinity; homogeneous distribution of the recognition sites; recycle of the template	Low yield; not effective for thermosensitive and bulky templates
High dilution polymerization[197,198]	The monomer is dissolved in a high amount of solvent to avoid precipitation during the process	MIPs size is equal to a few nm	High amount of solvent

Table 1. Techniques for the synthesis of MIPs.

Precipitation Polymerization

Precipitation polymerization was first reported by Ye et al. in 1999.[185] This simple method allows for the synthesis of uniform and spherical MIP nanoparticles in a one-step reaction. The process involves an excess of solvent in which the monomers, initiator, and template are soluble, while the polymer that forms is not. Polymer chains continue to form from the monomers and oligomers until their size causes them to precipitate.[181,199] The obtained MIPs are then collected through washing and centrifugation.[200] Key parameters to adjust include solvent polarity, temperature, and stirring speed. The advantages of this technique include the absence of stabilizer molecules, while the disadvantages include the need for a large amount of template and relatively long reaction times.[181,201]

Emulsion Polymerization

Another important method for producing nanogels is emulsion polymerization (Figure 6), which enables the synthesis of monodisperse MIP nanoparticles[186] with surface-exposed binding sites.[202] The polymerization process usually takes place in oil-in-water emulsions (less frequently in water-in-oil emulsions) in the presence of a surfactant.[203] This technique can be performed in mini- and micro-emulsion forms, yielding nanoparticles with diameters ranging from 30–500 nm for mini-emulsions to 5–50 nm for micro-emulsions.[154] A co-surfactant stabilizes the monomers, followed by homogenization through sonication or stirring.[204] The difference between mini- and micro-emulsion polymerization is that the latter requires a higher surfactant concentration to obtain smaller particles. An advantage of emulsion polymerization is its high yield and suitability for protein imprinting [186]; however, the polymers often require purification, especially to remove the surfactant, which can be time-consuming.[154]

Core-Shell Grafting Polymerization

Moreover, another technique for producing core-shell MIP nanoparticles is core-shell grafting followed by polymerization.[154] Preformed particles, such as organic polymers, silica, superparamagnetic iron oxides, quantum dots, upconversion nanophosphors, carbon dots, and gold/silver particles, are used as the core, while MIPs form the shell of the nanoparticles.[187–193] This technique allows for precise control over the MIP size.[194]

Solid-Phase Synthesis

A more recent approach in nanogel synthesis is solid-phase synthesis (Figure 7), which involves polymerization after immobilizing the template molecule on glass beads activated with NaOH to expose -OH groups for silanization.[195] Afterward, the nanogels must be purified. Solid-phase synthesis allows for the creation of MIPs with high affinity and a homogeneous distribution of recognition sites, as well as the recycling of the template and eliminating the need for a washing phase to remove the template from the polymer[154,202]. However, the drawbacks include low yield and limited effectiveness for templates with large structures.[202] Additionally, the detachment of MIPs is done by applying heat, which makes it impossible to increase reaction yield by performing multiple syntheses on the same solid phase using thermosensitive templates like proteins.[196]

Other Polymerization Techniques

High dilution polymerization is a method where the monomer is dissolved in a large amount of solvent to avoid precipitation during the process.[197] This technique allows for the synthesis of MIPs with very small sizes, similar to natural antibodies.[198] Surface-imprinted materials have recognition sites located on the polymer surface and show enhanced selectivity and sensitivity,

improving recognition effectiveness.[169,205] They are produced by localizing the template on the polymer surface, and the most commonly used techniques are solid-phase synthesis and emulsion polymerization.[206–208] A specific strategy employed when the template is a difficult-to-obtain or large molecule is fragment imprinting, also known as segment imprinting, which uses a portion of the target molecule as a pseudo-template to create MIPs.[209]

Applications of MIPs as Antibodies

Initially, molecularly imprinted polymers (MIPs) were primarily focused on separation tasks rather than recognition due to the inherent interactions between the templates and the polymer or functional monomers. However, advancements in imprinting techniques have expanded the applications of MIPs to various fields, including sensing, bioimaging, and drug delivery. For instance, Shinde et al. successfully synthesized core-shell SA-MIPs that can recognize glycan motifs on cancer cells, utilizing the fluorescent reporter nitrobenzoxadiazole (NBD) within the polymer shell for effective imaging of SA on tumor cells.[187] Similarly, Canfarotta et al. developed a MIP capable of selectively delivering the cytotoxic drug doxorubicin to tumor cells that overexpress the epidermal growth factor receptor.[210]

The first therapeutic MIP was created in 2010, designed to bind and neutralize the bee venom toxin melittin in mouse blood, significantly reducing mortality rates.[211] The primary focus of MIPs has been in cancer pharmacology, where a critical requirement is the extended retention time of drugs within tumor tissues.[212] One strategy to achieve this involves targeting cadherins, proteins that facilitate cell–cell adhesion, as their uncontrolled expression can promote cancer proliferation.[202,213] In this context, researchers utilized an oligopeptide fragment of cadherin as a template. Thermo-responsive MIPs were synthesized through solid-phase polymerization of various acrylamides in the presence of a crosslinking agent and an immobilized oligopeptide. The

results demonstrated that these MIPs effectively reduced tumor cell proliferation more than traditional monoclonal antibodies.[214]

Another cancer therapy approach involves inhibiting the HER2 pathway, which is overexpressed in breast cancer and interacts with proteins like HER3 to promote tumor growth.[215] While this interaction has been previously targeted with monoclonal antibodies, MIPs created using boronate affinity-oriented surface imprinting polymerization and conjugated with silica nanoparticles containing fluorescein isothiocyanate have shown greater effectiveness in reducing cancer tissue in female mice.[216]

Moreover, MIPs hold promise for treating infectious diseases by recognizing and blocking components of pathogens such as bacteria, viruses, fungi, and protists involved in infection processes. For example, Parisi et al. employed non-covalent imprinting to develop a MIP that could recognize and bind to the receptor-binding domain of the spike protein of SARS-CoV-2, which is crucial for the virus's attachment to host cells. The resulting imprinted nanoparticles significantly inhibited virus replication in Vero cell cultures.[217,218]

SUMMARY OF THE PAPERS

The aim of this thesis is to explore the development of synthetic receptors using Molecular Imprinting Technology, with a particular focus on Molecularly Imprinted Polymers (MIPs) as robust alternatives to traditional antibody-based systems. The research spans three papers, each contributing to a deeper understanding of MIP technology and its potential applications in diagnostics and therapeutics.

Paper I, currently under review in a peer-reviewed journal, serves as a foundational study for understanding MIPs. It focuses on the use of nanogels to enhance molecular recognition properties and functionality. This study also includes significant advancements in the production and characterization of nanogels, offering crucial insights that inform the methodologies and approaches used in subsequent research.

Paper II, published in a peer-reviewed journal, showcases the successful application of MIPs for targeting the receptor-binding domain (RBD) of the SARS-CoV-2 spike protein. The study achieves promising results in inhibiting viral entry, demonstrating the potential of MIPs as a therapeutic tool against the Omicron variant of SARS-CoV-2.

Building on the advancements in viral inhibition seen in Paper II, **Paper III**, currently in manuscript form, extends the application of MIPs to the Zika virus. It explores the use of polysaccharide-based MIP nanoparticles for the selective recognition of the Zika virus envelope protein (ZIKV-E). This study represents a novel approach to combating mosquito-borne pathogens, with significant implications for public health.

Paper I

Development and Benchmarking of Molecularly Imprinted Polymers for Human Chorionic Gonadotropin (hCG) Detection

The first study focuses on the development of MIP nanogels for the detection of human Chorionic Gonadotropin (hCG), a hormone that is the primary biomarker for pregnancy. Traditional pregnancy tests rely on lateral flow assays (LFAs), which use antibodies to bind to hCG and produce a colour change. However, LFAs suffer from several limitations, including the need for antibody production, poor stability, sensitivity issues under adverse storage conditions, and the fact that they are typically designed for single use. To address these drawbacks, this research investigates the use of MIPs as synthetic receptors for hCG, providing an alternative that is both reusable and more cost-effective.

MIP nanogels were designed to target two specific epitopes of hCG, namely the SV and PQ epitopes, using a novel approach of magnetic template-assisted imprinting. This technique allows for high-yielding, dispersed-phase imprinting, which ensures a uniform and reproducible distribution of imprinted sites within the nanogel matrix. Molecular dynamics simulations were employed to study the conformational overlap between the templates and the native hCG protein, supporting the suitability of the chosen epitopes for generating recognition sites.

The resulting MIP nanogels demonstrated exceptional binding affinity for hCG, with nanomolar dissociation constants revealed through Quartz Crystal Microbalance (QCM)-based binding tests and kinetic interaction analysis using Surface Plasmon Resonance (SPR). These nanogels exhibited a sensitive response to hCG concentrations within the physiologically relevant range of 6.30 to 200 mIU/mL, which is typical for home-based pregnancy testing. Importantly, the MIPs showed minimal interference from luteinizing hormone (LH), which can cause false positives in traditional tests. When benchmarked against commercial hCG enzyme-linked immunosorbent assays (ELISA),

the MIP-based assays demonstrated comparable or even superior performance in terms of sensitivity and specificity.

Paper II

Molecularly imprinted polymers (MIPs) for SARS-CoV-2 omicron variant inhibition: An alternative approach to address the challenge of emerging zoonoses

The second study builds upon the concept of MIPs by exploring their application in the context of the COVID-19 pandemic. The SARS-CoV-2 virus, which causes COVID-19, uses its spike protein's receptor-binding domain (RBD) to bind to the human ACE2 receptor, facilitating viral entry into host cells. This interaction is a critical target for therapeutic interventions, and the development of MIPs that can block this binding offers an exciting alternative to traditional antibody-based treatments.

The study focuses on the Omicron variant of SARS-CoV-2, which has become the dominant strain due to its increased transmissibility and ability to evade immunity. MIPs were synthesized to target the RBD of the Omicron spike protein using inverse microemulsion polymerization. This approach allowed for precise control over the size, morphology, and surface charge of the MIPs, addressing the issues of stability and dispersion that were present in earlier research.

After synthesis, the MIPs were thoroughly characterized to assess their recognition properties and ability to inhibit the interaction between the SARS-CoV-2 RBD and the ACE2 receptor. The study used QCM-D for rebinding studies, which demonstrated that the MIPs exhibited strong binding affinity for the RBD, with a concentration-dependent reduction in the RBD's ability to bind ACE2. Notably, the MIPs did not exhibit any cytotoxic effects in vitro, suggesting that they are safe for use in therapeutic applications.

Paper III

Biopolymeric Nanoparticles as MIPs for Zika Virus Recognition

The third study expands the application of MIPs to the detection of the Zika virus, a mosquito-borne pathogen that poses significant risks to public health, particularly in pregnant women, as it can lead to severe birth defects. The study introduces a novel approach by developing MIP nanoparticles based on polysaccharides, specifically sodium alginate and chitosan, which are biocompatible and biodegradable materials. These nanoparticles were designed to target the Zika virus envelope protein (ZIKV-E), a key antigen involved in viral entry into host cells.

To optimize the MIP synthesis process, controlled depolymerization with hydrogen peroxide was used to adjust the molecular weight of the base materials, enhancing their solubility and stability. This step was crucial in ensuring that the resulting nanoparticles exhibited optimal size, uniform distribution, and reproducibility. The MIPs were then characterized in terms of their physical properties, and QCM-D was used to determine their binding affinity and specificity for ZIKV-E. The MIP nanoparticles demonstrated superior binding capacity compared to non-imprinted polymers (NIPs), highlighting their potential for use in specific and sensitive detection assays.

In vitro evaluations further confirmed the excellent biocompatibility of the MIPs, with no evidence of cytotoxicity or sensitizing effects in cell viability assays and the human Cell Line Activation Test (h-CLAT). This makes them highly suitable for biomedical applications, particularly in therapeutic treatments, where safety and non-toxicity are critical.

REFERENCES

[1] Chomel BB. Zoonoses. Reference Module in Biomedical Sciences. Elsevier; 2014.

[2] Milton AAP, Priya GB, Ghatak S, et al. Viral Zoonoses: Wildlife Perspectives. 2020. p. 339–378.

[3] WANG L-F, CRAMERI G. Emerging zoonotic viral diseases. Revue Scientifique et Technique de l'OIE. 2014;33(2):569–581.

[4] FAILLOUX AB, MOUTAILLER S. Aspects zoonotiques des infections à transmission vectorielle. Revue Scientifique et Technique de l'OIE. 2015;34(1):165–183.

[5] Reed KD. Viral Zoonoses. Reference Module in Biomedical Sciences. Elsevier; 2018.

[6] Shaheen MNF. The concept of one health applied to the problem of zoonotic diseases. Rev Med Virol. 2022;32(4).

[7] World Health Organization (WHO). Vector-borne diseases. https://www.who.int/news-room/fact-sheets/detail/vector-borne-diseases.

[8] Heukelbach J, Alencar CH, Kelvin AA, et al. Zika virus outbreak in Brazil. The Journal of Infection in Developing Countries. 2016;10(02):116–120.

[9] Yang Y, Peng F, Wang R, et al. The deadly coronaviruses: The 2003 SARS pandemic and the 2020 novel coronavirus epidemic in China. J Autoimmun. 2020;109:102434.

[10] Payne S. Family Coronaviridae. Viruses. Elsevier; 2017. p. 149–158.

[11] da Costa VG, Moreli ML, Saivish MV. The emergence of SARS, MERS and novel SARS-2 coronaviruses in the 21st century. Arch Virol. 2020;165(7):1517–1526.

[12] Dhama K, Khan S, Tiwari R, et al. Coronavirus Disease 2019–COVID-19. Clin Microbiol Rev. 2020;33(4).

[13] Cui J, Li F, Shi Z-L. Origin and evolution of pathogenic coronaviruses. Nat Rev Microbiol. 2019;17(3):181–192.

[14] Han H-J, Wen H, Zhou C-M, et al. Bats as reservoirs of severe emerging infectious diseases. Virus Res. 2015;205:1–6.

[15] Yuan S, Jiang S-C, Li Z-L. Analysis of Possible Intermediate Hosts of the New Coronavirus SARS-CoV-2. Front Vet Sci. 2020;7.

[16] Zhan J, Liu QS, Sun Z, et al. Environmental impacts on the transmission and evolution of COVID-19 combing the knowledge of pathogenic respiratory coronaviruses. Environmental Pollution. 2020;267:115621.

[17] Channappanavar R, Perlman S. Age-related susceptibility to coronavirus infections: role of impaired and dysregulated host immunity. Journal of Clinical Investigation. 2020;130(12):6204–6213.

[18] Abdelghany TM, Ganash M, Bakri MM, et al. SARS-CoV-2, the other face to SARS-CoV and MERS-CoV: Future predictions. Biomed J. 2021;44(1):86–93.

[19] Liu DX, Fung TS, Chong KK-L, et al. Accessory proteins of SARS-CoV and other coronaviruses. Antiviral Res. 2014;109:97–109.

[20] Malone B, Urakova N, Snijder EJ, et al. Structures and functions of coronavirus replication–transcription complexes and their relevance for SARS-CoV-2 drug design. Nat Rev Mol Cell Biol. 2022;23(1):21–39.

[21] V'kovski P, Kratzel A, Steiner S, et al. Coronavirus biology and replication: implications for SARS-CoV-2. Nat Rev Microbiol. 2021;19(3):155–170.

[22] Artika IM, Dewantari AK, Wiyatno A. Molecular biology of coronaviruses: current knowledge. Heliyon. 2020;6(8):e04743.

[23] Jha N, Jeyaraman M, Rachamalla M, et al. Current Understanding of Novel Coronavirus: Molecular Pathogenesis, Diagnosis, and Treatment Approaches. Immuno. 2021;1(1):30–66.

[24] Lin P, Wang M, Wei Y, et al. Coronavirus in human diseases: Mechanisms and advances in clinical treatment. MedComm (Beijing). 2020;1(3):270–301.

[25] Masters PS. The Molecular Biology of Coronaviruses. 2006. p. 193–292.

[26] Kaniyala Melanthota S, Banik S, Chakraborty I, et al. Elucidating the microscopic and computational techniques to study the structure and pathology of <scp>SARS-CoVs</scp>. Microsc Res Tech. 2020;83(12):1623–1638.

[27] Nassar A, Ibrahim IM, Amin FG, et al. A Review of Human Coronaviruses' Receptors: The Host-Cell Targets for the Crown Bearing Viruses. Molecules. 2021;26(21):6455.

[28] Seminara G, Carli B, Forni G, et al. Biological fluid dynamics of airborne COVID-19 infection. Rend Lincei Sci Fis Nat. 2020;31(3):505–537.

[29] Yuan H-W, Wen H-L. Research progress on coronavirus S proteins and their receptors. Arch Virol. 2021;166(7):1811–1817.

[30] Huang Y, Yang C, Xu X, et al. Structural and functional properties of SARS-CoV-2 spike protein: potential antivirus drug development for COVID-19. Acta Pharmacol Sin. 2020;41(9):1141–1149.

[31] Nakagawa K, Lokugamage KG, Makino S. Viral and Cellular mRNA Translation in Coronavirus-Infected Cells. 2016. p. 165–192.

[32] Eriani G, Martin F. Viral and cellular translation during SARS-CoV-2 infection. FEBS Open Bio. 2022;12(9):1584–1601.

[33] Wang W, Chen J, Yu X, et al. Signaling mechanisms of SARS-CoV-2 Nucleocapsid protein in viral infection, cell death and inflammation. Int J Biol Sci. 2022;18(12):4704–4713.

[34] World Health Organization (WHO). Modes of transmission of virus causing COVID-19. https://www.who.int/news-room/commentaries/detail/modes-of-transmission-of-virus-causing-covid-19-implications-for-ipc-precaution-recommendations.

[35] Harrison AG, Lin T, Wang P. Mechanisms of SARS-CoV-2 Transmission and Pathogenesis. Trends Immunol. 2020;41(12):1100–1115.

[36] Marquès M, Domingo JL. Contamination of inert surfaces by SARS-CoV-2: Persistence, stability and infectivity. A review. Environ Res. 2021;193:110559.

[37] Ashokkumar S, Kaushik NK, Han I, et al. Persistence of Coronavirus on Surface Materials and Its Control Measures Using Nonthermal Plasma and Other Agents. Int J Mol Sci. 2023;24(18):14106.

[38] Gozalo AS, Clark TS, Kurtz DM. Coronaviruses: Troubling Crown of the Animal Kingdom. Comp Med. 2023;73(1):6–44.

[39] Khalafalla AI. Zoonotic diseases transmitted from the camels. Front Vet Sci. 2023;10.

[40] Baj J, Karakuła-Juchnowicz H, Teresiński G, et al. COVID-19: Specific and Non-Specific Clinical Manifestations and Symptoms: The Current State of Knowledge. J Clin Med. 2020;9(6):1753.

[41] Hui DS. Epidemic and Emerging Coronaviruses (Severe Acute Respiratory Syndrome and Middle East Respiratory Syndrome). Clin Chest Med. 2017;38(1):71–86.

[42] Zhu Z, Lian X, Su X, et al. From SARS and MERS to COVID-19: a brief summary and comparison of severe acute respiratory infections caused by three highly pathogenic human coronaviruses. Respir Res. 2020;21(1):224.

[43] Lombardi AF, Afsahi AM, Gupta A, et al. Severe acute respiratory syndrome (SARS), Middle East respiratory syndrome (MERS), influenza, and COVID-19, beyond the lungs: a review article. Radiol Med. 2021;126(4):561–569.

[44] Wang Z, Deng H, Ou C, et al. Clinical symptoms, comorbidities and complications in severe and non-severe patients with COVID-19. Medicine. 2020;99(48):e23327.

[45] Pfortmueller CA, Spinetti T, Urman RD, et al. COVID-19-associated acute respiratory distress syndrome (CARDS): Current knowledge on pathophysiology and ICU treatment – A narrative review. Best Pract Res Clin Anaesthesiol. 2021;35(3):351–368.

[46] Raghav PK, Mann Z, Ahluwalia SK, et al. Potential treatments of COVID-19: Drug repurposing and therapeutic interventions. J Pharmacol Sci. 2023;152(1):1–21.

[47] Eastman RT, Roth JS, Brimacombe KR, et al. Remdesivir: A Review of Its Discovery and Development Leading to Emergency Use Authorization for Treatment of COVID-19. ACS Cent Sci. 2020;6(5):672–683.

[48] Frediansyah A, Nainu F, Dhama K, et al. Remdesivir and its antiviral activity against COVID-19: A systematic review. Clin Epidemiol Glob Health. 2021;9:123–127.

[49] Haslam A, Prasad V. A Systematic Review of Nirmatrelvir/Ritonavir and Molnupiravir for the Treatment of Coronavirus Disease 2019. Open Forum Infect Dis. 2024;11(9).

[50] Parums D V. Editorial: Current Status of Oral Antiviral Drug Treatments for SARS-CoV-2 Infection in Non-Hospitalized Patients. Medical Science Monitor. 2022;28.

[51] Hwang Y-C, Lu R-M, Su S-C, et al. Monoclonal antibodies for COVID-19 therapy and SARS-CoV-2 detection. J Biomed Sci. 2022;29(1):1.

[52] Miguez-Rey E, Choi D, Kim S, et al. Monoclonal antibody therapies in the management of SARS-CoV-2 infection. Expert Opin Investig Drugs. 2022;31(1):41–58.

[53] Gao M, Ao G, Hao X, et al. Casirivimab-imdevimab treatment is associated with reduced rates of mortality and hospitalization in patients with COVID-19: A systematic review with meta-analysis. Journal of Infection. 2023;87(1):82–84.

[54] Falcone M, Tiseo G, Valoriani B, et al. Efficacy of Bamlanivimab/Etesevimab and Casirivimab/Imdevimab in Preventing Progression to Severe COVID-19 and Role of Variants of Concern. Infect Dis Ther. 2021;10(4):2479–2488.

[55] Dyall J, Gross R, Kindrachuk J, et al. Middle East Respiratory Syndrome and Severe Acute Respiratory Syndrome: Current Therapeutic Options and Potential Targets for Novel Therapies. Drugs. 2017;77(18):1935–1966.

[56] Akinbolade S, Coughlan D, Fairbairn R, et al. Combination therapies for COVID-19: An overview of the clinical trials landscape. Br J Clin Pharmacol. 2022;88(4):1590–1597.

[57] Sasaki M, Sugi T, Iida S, et al. Combination therapy with oral antiviral and anti-inflammatory drugs improves the efficacy of delayed treatment in a COVID-19 hamster model. EBioMedicine. 2024;99:104950.

[58] Patel R, Kaki M, Potluri VS, et al. A comprehensive review of SARS-CoV-2 vaccines: Pfizer, Moderna & Johnson & Johnson. Hum Vaccin Immunother. 2022;18(1).

[59] Tregoning JS, Flight KE, Higham SL, et al. Progress of the COVID-19 vaccine effort: viruses, vaccines and variants versus efficacy, effectiveness and escape. Nat Rev Immunol. 2021;21(10):626–636.

[60] Pastorino B, Nougairède A, Wurtz N, et al. Role of host cell factors in flavivirus infection: Implications for pathogenesis and development of antiviral drugs. Antiviral Res. 2010;87(3):281–294.

[61] Blitvich B, Firth A. A Review of Flaviviruses that Have No Known Arthropod Vector. Viruses. 2017;9(6):154.

[62] Liang Y, Dai X. The global incidence and trends of three common flavivirus infections (Dengue, yellow fever, and Zika) from 2011 to 2021. Front Microbiol. 2024;15.

[63] Flaviviridae. Fenner's Veterinary Virology. Elsevier; 2017. p. 525–545.

[64] Rocklöv J, Dubrow R. Climate change: an enduring challenge for vector-borne disease prevention and control. Nat Immunol. 2020;21(5):479–483.

[65] Messina JP, Brady OJ, Golding N, et al. The current and future global distribution and population at risk of dengue. Nat Microbiol. 2019;4(9):1508–1515.

[66] Mackenzie JS, Gubler DJ, Petersen LR. Emerging flaviviruses: the spread and resurgence of Japanese encephalitis, West Nile and dengue viruses. Nat Med. 2004;10(S12):S98–S109.

[67] Pybus OG, Rambaut A. Evolutionary analysis of the dynamics of viral infectious disease. Nat Rev Genet. 2009;10(8):540–550.

[68] Ciota AT, Kramer LD. Insights into Arbovirus Evolution and Adaptation from Experimental Studies. Viruses. 2010;2(12):2594–2617.

[69] Chen R, Vasilakis N. Dengue — Quo tu et quo vadis? Viruses. 2011;3(9):1562–1608.

[70] Slonchak A, Parry R, Pullinger B, et al. Structural analysis of 3'UTRs in insect flaviviruses reveals novel determinants of sfRNA biogenesis and provides new insights into flavivirus evolution. Nat Commun. 2022;13(1):1279.

[71] Flaviviridae. Virus Taxonomy. Elsevier; 2012. p. 1003–1020.

[72] Miorin L, Maiuri P, Marcello A. Visual detection of Flavivirus RNA in living cells. Methods. 2016;98:82–90.

[73] Staples JE, Monath TP, Gershman MD, et al. Yellow Fever Vaccines. Plotkin's Vaccines. Elsevier; 2018. p. 1181-1265.e20.

[74] Zhao R, Wang M, Cao J, et al. Flavivirus: From Structure to Therapeutics Development. Life. 2021;11(7):615.

[75] Akey DL, Brown WC, Jose J, et al. Structure-guided insights on the role of NS1 in flavivirus infection. BioEssays. 2015;37(5):489–494.

[76] Ishida K, Goto S, Ishimura M, et al. Functional Correlation between Subcellular Localizations of Japanese Encephalitis Virus Capsid Protein and Virus Production. J Virol. 2019;93(19).

[77] Li M, Johnson JR, Truong B, et al. Identification of antiviral roles for the exon–junction complex and nonsense-mediated decay in flaviviral infection. Nat Microbiol. 2019;4(6):985–995.

[78] Liu Z-Y, Li X-F, Jiang T, et al. Novel *cis* -Acting Element within the Capsid-Coding Region Enhances Flavivirus Viral-RNA Replication by Regulating Genome Cyclization. J Virol. 2013;87(12):6804–6818.

[79] Ye J, Chen Z, Zhang B, et al. Heat Shock Protein 70 Is Associated with Replicase Complex of Japanese Encephalitis Virus and Positively Regulates Viral Genome Replication. PLoS One. 2013;8(9):e75188.

[80] Savidis G, McDougall WM, Meraner P, et al. Identification of Zika Virus and Dengue Virus Dependency Factors using Functional Genomics. Cell Rep. 2016;16(1):232–246.

[81] Hasan SS, Sevvana M, Kuhn RJ, et al. Structural biology of Zika virus and other flaviviruses. Nat Struct Mol Biol. 2018;25(1):13–20.

[82] Dowd KA, Pierson TC. The Many Faces of a Dynamic Virion: Implications of Viral Breathing on Flavivirus Biology and Immunogenicity. Annu Rev Virol. 2018;5(1):185–207.

[83] Luca VC, AbiMansour J, Nelson CA, et al. Crystal Structure of the Japanese Encephalitis Virus Envelope Protein. J Virol. 2012;86(4):2337–2346.

[84] Füzik T, Formanová P, Růžek D, et al. Structure of tick-borne encephalitis virus and its neutralization by a monoclonal antibody. Nat Commun. 2018;9(1):436.

[85] Mukherjee S, Sirohi D, Dowd KA, et al. Enhancing dengue virus maturation using a stable furin over-expressing cell line. Virology. 2016;497:33–40.

[86] Morrison J, Aguirre S, Fernandez-Sesma A. Innate Immunity Evasion by Dengue Virus. Viruses. 2012;4(3):397–413.

[87] Shah PS, Link N, Jang GM, et al. Comparative Flavivirus-Host Protein Interaction Mapping Reveals Mechanisms of Dengue and Zika Virus Pathogenesis. Cell. 2018;175(7):1931-1945.e18.

[88] Zhang Z, Rong L, Li Y-P. *Flaviviridae* Viruses and Oxidative Stress: Implications for Viral Pathogenesis. Oxid Med Cell Longev. 2019;2019:1–17.

[89] Zeng Q, Liu J, Hao C, et al. Making sense of flavivirus non-strctural protein 1 in innate immune evasion and inducing tissue-specific damage. Virus Res. 2023;336:199222.

[90] Suthar MS, Aguirre S, Fernandez-Sesma A. Innate Immune Sensing of Flaviviruses. PLoS Pathog. 2013;9(9):e1003541.

[91] Markoff L. 5′- and 3′-noncoding regions in flavivirus RNA. 2003. p. 177–228.

[92] Brinton MA, Basu M. Functions of the 3′ and 5′ genome RNA regions of members of the genus Flavivirus. Virus Res. 2015;206:108–119.

[93] Ng W, Soto-Acosta R, Bradrick S, et al. The 5′ and 3′ Untranslated Regions of the Flaviviral Genome. Viruses. 2017;9(6):137.

[94] Kaufmann B, Rossmann MG. Molecular mechanisms involved in the early steps of flavivirus cell entry. Microbes Infect. 2011;13(1):1–9.

[95] Fernandez-Garcia M-D, Meertens L, Bonazzi M, et al. Appraising the Roles of CBLL1 and the Ubiquitin/Proteasome System for Flavivirus Entry and Replication. J Virol. 2011;85(6):2980–2989.

[96] Mazeaud C, Freppel W, Chatel-Chaix L. The Multiples Fates of the Flavivirus RNA Genome During Pathogenesis. Front Genet. 2018;9.

[97] Verhaegen M, Vermeire K. The endoplasmic reticulum (ER): a crucial cellular hub in flavivirus infection and potential target site for antiviral interventions. npj Viruses. 2024;2(1):24.

[98] Aktepe TE, Mackenzie JM. Shaping the flavivirus replication complex: It is curvaceous! Cell Microbiol. 2018;20(8).

[99] Xie X, Gayen S, Kang C, et al. Membrane Topology and Function of Dengue Virus NS2A Protein. J Virol. 2013;87(8):4609–4622.

[100] Xie X, Zou J, Puttikhunt C, et al. Two Distinct Sets of NS2A Molecules Are Responsible for Dengue Virus RNA Synthesis and Virion Assembly. J Virol. 2015;89(2):1298–1313.

[101] Yoshii K, Igarashi M, Ichii O, et al. A conserved region in the prM protein is a critical determinant in the assembly of flavivirus particles. Journal of General Virology. 2012;93(1):27–38.

[102] Sager G, Gabaglio S, Sztul E, et al. Role of Host Cell Secretory Machinery in Zika Virus Life Cycle. Viruses. 2018;10(10):559.

[103] Therkelsen MD, Klose T, Vago F, et al. Flaviviruses have imperfect icosahedral symmetry. Proceedings of the National Academy of Sciences. 2018;115(45):11608–11612.

[104] Sampath A, Padmanabhan R. Molecular targets for flavivirus drug discovery. Antiviral Res. 2009;81(1):6–15.

[105] Nicholls CMR, Sevvana M, Kuhn RJ. Structure-guided paradigm shifts in flavivirus assembly and maturation mechanisms. 2020. p. 33–83.

[106] van Leur SW, Heunis T, Munnur D, et al. Pathogenesis and virulence of flavivirus infections. Virulence. 2021;12(1):2814–2838.

[107] Li G, Teleki C, Wang T. Memory T Cells in Flavivirus Vaccination. Vaccines (Basel). 2018;6(4):73.

[108] Reteng P, Nguyen Thuy L, Tran Thi Minh T, et al. A targeted approach with nanopore sequencing for the universal detection and identification of flaviviruses. Sci Rep. 2021;11(1):19031.

[109] Chin K-L, Tan K-K, Bakar SA, et al. Resveratrol as an epigenetic therapy for flavivirus infection: A narrative review. Asian Pac J Trop Med. 2023;16(12):546–557.

[110] Sips GJ, Wilschut J, Smit JM. Neuroinvasive flavivirus infections. Rev Med Virol. 2012;22(2):69–87.

[111] Estofolete CF, Milhim BHGA, Zini N, et al. Flavivirus Infection Associated with Cerebrovascular Events. Viruses. 2020;12(6):671.

[112] Mota MT de O, Estofolete CF, Zini N, et al. Transverse Myelitis as an Unusual Complication of Dengue Fever. The American Society of Tropical Medicine and Hygiene. 2017;96(2):380–381.

[113] Nath H, Ghosh A, Basu K, et al. Dengue virus clinical isolates sustain viability of infected hepatic cells by counteracting apoptosis-mediated DNA breakage. 2020.

[114] Patel SS, Winkle P, Faccin A, et al. An open-label, Phase 3 trial of TAK-003, a live attenuated dengue tetravalent vaccine, in healthy US adults: immunogenicity and safety when administered during the second half of a 24-month shelf-life. Hum Vaccin Immunother. 2023;19(2).

[115] González–Barreto W, Rodríguez–Vega GM, De Jesús–Umpierre P, et al. Miller Fisher−Guillain−Barré overlap syndrome during the Zika Virus outbreak. Archive of Clinical Cases. 2017;04(04):199–203.

[116] Li X-F, Li X-D, Deng C-L, et al. Visualization of a neurotropic flavivirus infection in mouse reveals unique viscerotropism controlled by host type I interferon signaling. Theranostics. 2017;7(4):912–925.

[117] Papa MP, Meuren LM, Coelho SVA, et al. Zika Virus Infects, Activates, and Crosses Brain Microvascular Endothelial Cells, without Barrier Disruption. Front Microbiol. 2017;8.

[118] Siahaan AMP, Tandean S, Nainggolan BWM, et al. A Critical Analysis of Intracranial Hemorrhage as a Fatal Complication of Dengue Fever. J Korean Neurosurg Soc. 2023;66(5):494–502.

[119] Jhan M-K, Chen C-L, Shen T-J, et al. Polarization of Type 1 Macrophages Is Associated with the Severity of Viral Encephalitis Caused by Japanese Encephalitis Virus and Dengue Virus. Cells. 2021;10(11):3181.

[120] Dodd KA, Bird BH, Jones MEB, et al. Kyasanur Forest Disease Virus Infection in Mice Is Associated with Higher Morbidity and Mortality than Infection with the Closely Related Alkhurma Hemorrhagic Fever Virus. PLoS One. 2014;9(6):e100301.

[121] Pan Y, Cai W, Cheng A, et al. Flaviviruses: Innate Immunity, Inflammasome Activation, Inflammatory Cell Death, and Cytokines. Front Immunol. 2022;13.

[122] De Ory F, Sánchez-Seco M, Vázquez A, et al. Comparative Evaluation of Indirect Immunofluorescence and NS-1-Based ELISA to Determine Zika Virus-Specific IgM. Viruses. 2018;10(7):379.

[123] Chan KR, Ismail AA, Thergarajan G, et al. Serological cross-reactivity among common flaviviruses. Front Cell Infect Microbiol. 2022;12.

[124] Gandini M, Gras C, Azeredo EL, et al. Dengue Virus Activates Membrane TRAIL Relocalization and IFN-α Production by Human Plasmacytoid Dendritic Cells In Vitro and In Vivo. PLoS Negl Trop Dis. 2013;7(6):e2257.

[125] de Araújo TVB, Rodrigues LC, de Alencar Ximenes RA, et al. Association between Zika virus infection and microcephaly in Brazil, January to May, 2016: preliminary report of a case-control study. Lancet Infect Dis. 2016;16(12):1356–1363.

[126] He A, Brasil P, Siqueira AM, et al. The Emerging Zika Virus Threat: A Guide for Dermatologists. Am J Clin Dermatol. 2017;18(2):231–236.

[127] Honein MA, Dawson AL, Petersen EE, et al. Birth Defects Among Fetuses and Infants of US Women With Evidence of Possible Zika Virus Infection During Pregnancy. JAMA. 2017;317(1):59.

[128] Lim JK, McDermott DH, Lisco A, et al. CCR5 Deficiency Is a Risk Factor for Early Clinical Manifestations of West Nile Virus Infection but not for Viral Transmission. J Infect Dis. 2010;201(2):178–185.

[129] Wang Z, Yan Y, Dai Q, et al. Azelnidipine Exhibits In Vitro and In Vivo Antiviral Effects against Flavivirus Infections by Targeting the Viral RdRp. Viruses. 2022;14(6):1228.

[130] Zhang Z-R, Zhang H-Q, Li X-D, et al. Generation and characterization of Japanese encephalitis virus expressing GFP reporter gene for high throughput drug screening. Antiviral Res. 2020;182:104884.

[131] Pawlak JB, Hsu JC-C, Xia H, et al. CMPK2 restricts Zika virus replication by inhibiting viral translation. PLoS Pathog. 2023;19(4):e1011286.

[132] Komarasamy TV, Adnan NAA, James W, et al. Finding a chink in the armor: Update, limitations, and challenges toward successful antivirals against flaviviruses. PLoS Negl Trop Dis. 2022;16(4):e0010291.

[133] Nomhwange T, Baptiste A, Ezebilo O, et al. The Resurgence of Yellow Fever Outbreaks in Nigeria; A 2-Year Review 2017-2019. 2020.

[134] Wauters R, Hernandez C, Petersen M. An Atypical Local Vesicular Reaction to the Yellow Fever Vaccine. Vaccines (Basel). 2017;5(3):26.

[135] Rougemont B, Simon R, Carrière R, et al. Absolute quantification of dengue virus serotype 4 chimera vaccine candidate in Vero cell culture by targeted mass spectrometry. Proteomics. 2015;15(19):3320–3330.

[136] Hadinegoro SR, Arredondo-García JL, Capeding MR, et al. Efficacy and Long-Term Safety of a Dengue Vaccine in Regions of Endemic Disease. New England Journal of Medicine. 2015;373(13):1195–1206.

[137] Thisyakorn U, Thisyakorn C. Prospects for the Development of a Dengue Vaccine. Journal of Vaccines and Immunology. 2016;2(1):015–018.

[138] Oviya S, Kaviya S, Udhaya S. Dengue fever: Causes, complications, and vaccine strategies – A review. GSC Biological and Pharmaceutical Sciences. 2019;6(3):016–023.

[139] Csermely P, Palotai R, Nussinov R. Induced fit, conformational selection and independent dynamic segments: an extended view of binding events. Trends Biochem Sci. 2010;35(10):539–546.

[140] Fischer E. Einfluss der Configuration auf die Wirkung der Enzyme. Berichte der deutschen chemischen Gesellschaft. 1894;27(3):2985–2993.

[141] Cragg PJ. Supramolecular Chemistry. Dordrecht: Springer Netherlands; 2010.

[142] Lehn J. Perspectives in Supramolecular Chemistry—From Molecular Recognition towards Molecular Information Processing and Self-Organization. Angewandte Chemie International Edition in English. 1990;29(11):1304–1319.

[143] Aida T, Meijer EW, Stupp SI. Functional Supramolecular Polymers [Internet]. Available from: https://www.science.org.

[144] The Chemistry of Molecular Recognition — Host Molecules and Guest Molecules. Supramolecular Chemistry — Fundamentals and Applications. Berlin, Heidelberg: Springer Berlin Heidelberg; 2006. p. 7–44.

[145] Ogoshi T, Yamagishi T. Historical Background of Macrocyclic Compounds. Pillararenes. The Royal Society of Chemistry; 2015. p. 1–22.

[146] Cragg PJ, Vahora R. Crown and Lariat Ethers. Supramol Chem. Wiley; 2012.

[147] Barnes JC, Mirkin CA. Profile of Jean-Pierre Sauvage, Sir J. Fraser Stoddart, and Bernard L. Feringa, 2016 Nobel Laureates in Chemistry. Proceedings of the National Academy of Sciences. 2017;114(4):620–625.

[148] Woof JM, Burton DR. Human antibody–Fc receptor interactions illuminated by crystal structures. Nat Rev Immunol. 2004;4(2):89–99.

[149] Laflamme C, McKeever PM, Kumar R, et al. Implementation of an antibody characterization procedure and application to the major ALS/FTD disease gene C9ORF72. Elife. 2019;8.

[150] Lertjuthaporn S, Cicala C, Van Ryk D, et al. Select gp120 V2 domain specific antibodies derived from HIV and SIV infection and vaccination inhibit gp120 binding to α4β7. PLoS Pathog. 2018;14(8):e1007278.

[151] Rouet R, Henry JY, Johansen MD, et al. Broadly neutralizing SARS-CoV-2 antibodies through epitope-based selection from convalescent patients. Nat Commun. 2023;14(1):687.

[152] Nagano K, Tsutsumi Y. Phage Display Technology as a Powerful Platform for Antibody Drug Discovery. Viruses. 2021;13(2):178.

[153] Parisi OI, Puoci F. Chapter 13. Stimuli-responsive Molecularly Imprinted Polymers. 2015. p. 364–383.

[154] Refaat D, Aggour MG, Farghali AA, et al. Strategies for Molecular Imprinting and the Evolution of MIP Nanoparticles as Plastic Antibodies—Synthesis and Applications. Int J Mol Sci. 2019;20(24):6304.

[155] Poma A, Guerreiro A, Whitcombe MJ, et al. Solid-Phase Synthesis of Molecularly Imprinted Polymer Nanoparticles with a Reusable Template–"Plastic Antibodies." Adv Funct Mater. 2013;23(22):2821–2827.

[156] Polyakov M., Khim Z. Adsorption properties and structure of silica gel. Zh Fiz Khim Ser B . 1931;2:799–805.

[157] Dickey FH. The Preparation of Specific Adsorbents. Proceedings of the National Academy of Sciences. 1949;35(5):227–229.

[158] Pauling L. A Theory of the Formation of Antibodies 2643 [Contribution from the Gates A Theory of the Structure and Process of Formation of Antibodies* [Internet]. 1940. Available from: https://pubs.acs.org/sharingguidelines.

[159] Wulff G. The use of polymers with enzyme-analogous structures for the resolution of racemates. Angrew Chem Internat. 1972;341.

[160] Andersson L, Sellergren B, Mosbach K. Imprinting of amino acid derivatives in macroporous polymers. Tetrahedron Lett. 1984;25(45):5211–5214.

[161] Arshady R, Mosbach K. Synthesis of substrate-selective polymers by host-guest polymerization. Die Makromolekulare Chemie. 1981;182(2):687–692.

[162] Haupt K, Mosbach K. Molecularly Imprinted Polymers and Their Use in Biomimetic Sensors. Chem Rev. 2000;100(7):2495–2504.

[163] Morrison JL, Worsley M, Shaw DR, et al. THE NATURE OF THE SPECIFICITY OF ADSORPTION OF ALKYL ORANGE DYES ON SILICA GEL. Can J Chem. 1959;37(12):1986–1995.

[164] Liu M, Tran TM, Abbas Elhaj AA, et al. Molecularly Imprinted Porous Monolithic Materials from Melamine–Formaldehyde for Selective Trapping of Phosphopeptides. Anal Chem. 2017;89(17):9491–9501.

[165] Fitzmaurice RJ, Kyne GM, Douheret D, et al. Synthetic receptors for carboxylic acids and carboxylates. J Chem Soc Perkin 1. 2002;(7):841–864.

[166] Alexander C, Andersson HS, Andersson LI, et al. Molecular imprinting science and technology: a survey of the literature for the years up to and including 2003. Journal of Molecular Recognition. 2006;19(2):106–180.

[167] Wulff G. Molecular Imprinting in Cross-Linked Materials with the Aid of Molecular Templates— A Way towards Artificial Antibodies. Angewandte Chemie International Edition in English. 1995;34(17):1812–1832.

[168] Dhal PK, Arnold FH. Template-mediated synthesis of metal-complexing polymers for molecular recognition. J Am Chem Soc. 1991;113(19):7417–7418.

[169] Chen L, Xu S, Li J. Recent advances in molecular imprinting technology: current status, challenges and highlighted applications. Chem Soc Rev. 2011;40(5):2922.

[170] Chen L, Xu S, Li J. Recent advances in molecular imprinting technology: current status, challenges and highlighted applications. Chem Soc Rev. 2011;40(5):2922.

[171] Kriz D, Ramström O, Mosbach K. Molecular Imprinting: New Possibilities for Sensor Technology. Anal Chem. 1997;69(11):345A-349A.

[172] Sellergren B. Noncovalent molecular imprinting: antibody-like molecular recognition in polymeric network materials. TrAC Trends in Analytical Chemistry. 1997;16(6):310–320.

[173] Whitcombe MJ, Rodriguez ME, Villar P, et al. A New Method for the Introduction of Recognition Site Functionality into Polymers Prepared by Molecular Imprinting: Synthesis and Characterization of Polymeric Receptors for Cholesterol. J Am Chem Soc. 1995;117(27):7105–7111.

[174] Zahedi P, Ziaee M, Abdouss M, et al. Biomacromolecule template-based molecularly imprinted polymers with an emphasis on their synthesis strategies: a review. Polym Adv Technol. 2016;27(9):1124–1142.

[175] Ding S, Lyu Z, Niu X, et al. Integrating ionic liquids with molecular imprinting technology for biorecognition and biosensing: A review. Biosens Bioelectron. 2020;149:111830.

[176] Beyazit S, Tse Sum Bui B, Haupt K, et al. Molecularly imprinted polymer nanomaterials and nanocomposites by controlled/living radical polymerization. Prog Polym Sci. 2016;62:1–21.

[177] Adali-Kaya Z, Tse Sum Bui B, Falcimaigne-Cordin A, et al. Molecularly Imprinted Polymer Nanomaterials and Nanocomposites: Atom-Transfer Radical Polymerization with Acidic Monomers. Angewandte Chemie. 2015;127(17):5281–5284.

[178] Pan G, Zu B, Guo X, et al. Preparation of molecularly imprinted polymer microspheres via reversible addition–fragmentation chain transfer precipitation polymerization. Polymer (Guildf). 2009;50(13):2819–2825.

[179] Boonpangrak S, Whitcombe MJ, Prachayasittikul V, et al. Preparation of molecularly imprinted polymers using nitroxide-mediated living radical polymerization. Biosens Bioelectron. 2006;22(3):349–354.

[180] Vaughan AD, Sizemore SP, Byrne ME. Enhancing molecularly imprinted polymer binding properties via controlled/living radical polymerization and reaction analysis. Polymer (Guildf). 2007;48(1):74–81.

[181] Refaat D, Aggour MG, Farghali AA, et al. Strategies for Molecular Imprinting and the Evolution of MIP Nanoparticles as Plastic Antibodies—Synthesis and Applications. Int J Mol Sci. 2019;20(24):6304.

[182] Hoshino Y, Shea KJ. The evolution of plastic antibodies. J Mater Chem. 2011;21(11):3517–3521.

[183] Wulff G. Fourty years of molecular imprinting in synthetic polymers: origin, features and perspectives. Microchimica Acta. 2013;180(15–16):1359–1370.

[184] Poma A, Turner APF, Piletsky SA. Advances in the manufacture of MIP nanoparticles. Trends Biotechnol. 2010;28(12):629–637.

[185] Ye L, Cormack PAG, Mosbach K. Molecularly imprinted monodisperse microspheres for competitive radioassay. Analytical Communications. 1999;36(2):35–38.

[186] Haupt K, Medina Rangel PX, Bui BTS. Molecularly Imprinted Polymers: Antibody Mimics for Bioimaging and Therapy. Chem Rev. 2020;120(17):9554–9582.

[187] Shinde S, El-Schich Z, Malakpour-Permlid A, et al. Sialic Acid-Imprinted Fluorescent Core–Shell Particles for Selective Labeling of Cell Surface Glycans. J Am Chem Soc. 2015;137(43):13908–13912.

[188] Gonzato C, Courty M, Pasetto P, et al. Magnetic Molecularly Imprinted Polymer Nanocomposites via Surface-Initiated RAFT Polymerization. Adv Funct Mater. 2011;21(20):3947–3953.

[189] Wan L, Chen Z, Huang C, et al. Core–shell molecularly imprinted particles. TrAC Trends in Analytical Chemistry. 2017;95:110–121.

[190] Markose KK, Anjana R, Jayaraj MK. Upconversion Nanophosphors: An Overview. 2020. p. 47–102.

[191] Zhang Y, Li S, Ma X-T, et al. Carbon dots-embedded epitope imprinted polymer for targeted fluorescence imaging of cervical cancer via recognition of epidermal growth factor receptor. Microchimica Acta. 2020;187(4):228.

[192] Yin D, Li X, Ma Y, et al. Targeted cancer imaging and photothermal therapy via monosaccharide-imprinted gold nanorods. Chemical Communications. 2017;53(50):6716–6719.

[193] Canfarotta F, Cecchini A, Piletsky S. Nano-sized Molecularly Imprinted Polymers as Artificial Antibodies. Molecularly Imprinted Polymers for Analytical Chemistry Applications. The Royal Society of Chemistry; 2018. p. 1–27.

[194] Poma A, Guerreiro A, Whitcombe MJ, et al. Solid-Phase Synthesis of Molecularly Imprinted Polymer Nanoparticles with a Reusable Template–"Plastic Antibodies." Adv Funct Mater. 2013;23(22):2821–2827.

[195] Canfarotta F, Poma A, Guerreiro A, et al. Solid-phase synthesis of molecularly imprinted nanoparticles. Nat Protoc. 2016;11(3):443–455.

[196] Biffis A, Graham NB, Siedlaczek G, et al. The synthesis, characterization and molecular recognition properties of imprinted microgels. Macromol Chem Phys. 2001;202(1):163–171.

[197] Çakir P, Cutivet A, Resmini M, et al. Protein-Size Molecularly Imprinted Polymer Nanogels as Synthetic Antibodies, by Localized Polymerization with Multi-initiators. Advanced Materials. 2013;25(7):1048–1051.

[198] Wang S, Yin D, Wang W, et al. Targeting and Imaging of Cancer Cells via Monosaccharide-Imprinted Fluorescent Nanoparticles. Sci Rep. 2016;6(1):22757.

[199] Jing T, Gao X-D, Wang P, et al. Determination of trace tetracycline antibiotics in foodstuffs by liquid chromatography–tandem mass spectrometry coupled with selective molecular-imprinted solid-phase extraction. Anal Bioanal Chem. 2009;393(8):2009–2018.

[200] Vasapollo G, Sole R Del, Mergola L, et al. Molecularly Imprinted Polymers: Present and Future Prospective. Int J Mol Sci. 2011;12(9):5908–5945.

[201] Chen L, Wang X, Lu W, et al. Molecular imprinting: perspectives and applications. Chem Soc Rev. 2016;45(8):2137–2211.

[202] Vaihinger D, Landfester K, Kräuter I, et al. Molecularly imprinted polymer nanospheres as synthetic affinity receptors obtained by miniemulsion polymerisation. Macromol Chem Phys. 2002;203(13):1965–1973.

[203] Zhao G, Liu J, Liu M, et al. Synthesis of Molecularly Imprinted Polymer via Emulsion Polymerization for Application in Solanesol Separation. Applied Sciences. 2020;10(8):2868.

[204] Marchyk N, Maximilien J, Beyazit S, et al. One-pot synthesis of iniferter-bound polystyrene core nanoparticles for the controlled grafting of multilayer shells. Nanoscale. 2014;6(5):2872.

[205] Tian L, Guo H, Li J, et al. Fabrication of a near-infrared excitation surface molecular imprinting ratiometric fluorescent probe for sensitive and rapid detecting perfluorooctane sulfonate in complex matrix. J Hazard Mater. 2021;413:125353.

[206] Titirici MM, Hall AJ, Sellergren B. Hierarchical Imprinting Using Crude Solid Phase Peptide Synthesis Products as Templates. Chemistry of Materials. 2003;15(4):822–824.

[207] Xu J, Ambrosini S, Tamahkar E, et al. Toward a Universal Method for Preparing Molecularly Imprinted Polymer Nanoparticles with Antibody-like Affinity for Proteins. Biomacromolecules. 2016;17(1):345–353.

[208] Fresco-Cala B, Mizaikoff B. Surrogate Imprinting Strategies: Molecular Imprints via Fragments and Dummies. ACS Appl Polym Mater. American Chemical Society; 2020. p. 3714–3741.

[209] WANG Y, LI J, WANG L, et al. Recent advances in applications of fragment/dummy molecularly imprinted polymers. Chinese Journal of Chromatography. 2021;39(2):134–141.

[210] Canfarotta F, Lezina L, Guerreiro A, et al. Specific Drug Delivery to Cancer Cells with Double-Imprinted Nanoparticles against Epidermal Growth Factor Receptor. Nano Lett. 2018;18(8):4641–4646.

[211] Hoshino Y, Koide H, Urakami T, et al. Recognition, Neutralization, and Clearance of Target Peptides in the Bloodstream of Living Mice by Molecularly Imprinted Polymer Nanoparticles: A Plastic Antibody. J Am Chem Soc. 2010;132(19):6644–6645.

[212] Kiessling F, Mertens ME, Grimm J, et al. Nanoparticles for Imaging: Top or Flop? Radiology. 2014;273(1):10–28.

[213] Jeanes A, Gottardi CJ, Yap AS. Cadherins and cancer: how does cadherin dysfunction promote tumor progression? Oncogene. 2008;27(55):6920–6929.

[214] Medina Rangel PX, Moroni E, Merlier F, et al. Chemical Antibody Mimics Inhibit Cadherin-Mediated Cell–Cell Adhesion: A Promising Strategy for Cancer Therapy. Angewandte Chemie International Edition. 2020;59(7):2816–2822.

[215] Ishikawa T, Ichikawa Y, Shimizu D, et al. The role of HER-2 in Breast Cancer.

[216] Dong Y, Li W, Gu Z, et al. Inhibition of HER2-Positive Breast Cancer Growth by Blocking the HER2 Signaling Pathway with HER2-Glycan-Imprinted Nanoparticles. Angewandte Chemie International Edition. 2019;58(31):10621–10625.

[217] Parisi OI, Dattilo M, Patitucci F, et al. Design and development of plastic antibodies against SARS-CoV-2 RBD based on molecularly imprinted polymers that inhibit in vitro virus infection. Nanoscale. 2021;13(40).

[218] Wu C, Liu Y, Yang Y, et al. Analysis of therapeutic targets for SARS-CoV-2 and discovery of potential drugs by computational methods. Acta Pharm Sin B. 2020;10(5):766–788.

I

Development and Benchmarking of Molecularly Imprinted Polymers for Human Chorionic Gonadotropin (hCG) Detection

Radvilė Zubrytė,[1,2] Liliia Mavliutova,[2] Yadiris García,[3,4] Mark Sullivan,[5] Nicholas W. Turner,[5] Francesco Patitucci,[3,6] Laura C. Polania,[4] Verónica A. Jiménez,[4] Robert Porter,[1] Alice Mattsson,[1] and Börje Sellergren,[2,3*]

[1] Pharmista Technologies AB, Scheelevägen 3, Lund, 223 63, Sweden

[2] Surecapture Technologies AB, Per Albin Hanssons väg 35, Malmö 214 32, Sweden

[3] Biofilms Research Center for Biointerfaces, Malmö University, Per Albin Hanssons väg 35, Malmö 214 32, Sweden

[4] Departamento de Ciencias Químicas, Facultad de Ciencias Exactas, Universidad Andres Bello, Autopista Concepción-Talcahuano 7100, Talcahuano, Chile

[5] University of Sheffield, Dainton Building, Brook Hill, Sheffield S3 7HF, Great Britain

[6] Department of Pharmacy, Health and Nutritional Sciences, University of Calabria, 87036, Arcavacata di Rende (CS) - Italy

ABSTRACT

Diagnostic pregnancy tests are the most widely used immunoassays for home-based use. These tests employ the well-established lateral flow assay (LFA) technique, reminiscent of affinity chromatography relying on the dual action of two orthogonal anti-hCG antibodies. Immunoassays

suffer from several drawbacks, including challenges in antibody manufacturing, suboptimal accuracy and sensitivity to adverse storing conditions. Additionally, LFAs are typically designed for single use, as the LFA technique is nonreusable. An alternative to overcome these drawbacks is to leverage molecularly imprinted polymer (MIP) technology to generate polymer-based hCG-receptors and subsequently nonbioreceptor based tests. Here, we report the development of MIP nanogels for hCG detection, exploiting epitopes and magnetic templates for high-yielding dispersed phase imprinting. The resulting nanogels were designed for orthogonal targeting of two immunogenic epitopes (SV and PQ) and were thoroughly characterized with respect to physical properties, binding affinity, specificity, and sensitivity. Molecular dynamics simulations indicated a pronounced conformational overlap between the templates and the epitopes in the native protein, supporting their suitability for templating cavities for hCG recognition. Quartz crystal microbalance (QCM) -based binding tests and kinetic interaction analysis by via surface plasmon resonance (SPR) revealed nanomolar dissociation constants for the MIP nanogels and their corresponding template peptides. The optimized nanogels were benchmarked against hCG capture antibodies using a commercial hCG ELISA. The assays exhibited a sensitive response to physiologically relevant hCG concentrations between 6.30 and 200·mIU mL^{-1} with minimal interference from constant levels of luteinizing hormone (LH). This offers a new tool for future sustainable home-based and point of care testing using MIP nanogels as synthetic antibodies.

INTRODUCTION

Human chorionic gonadotropin (hCG) is a 36 kDa glycoprotein hormone produced by the placenta during early pregnancy. This protein is composed of an α and β chain forming a heterodimer, with variable glycosylation levels comprising up to ca 30% of its total molecular weight. hCG plays a pivotal role during early pregnancy by promoting the thickening of the uterine lining to support the nourishment of a growing embryo. Consequently, hCG becomes detectable shortly after fertilization.[1,2] Most pregnancy tests available on the market today demonstrate a detection accuracy of 99% when used on the day of a missed period or 14 days post-ovulation correlating with hCG levels of about 50 mIU/mL.[3] However, these levels can vary significantly among individuals. Given the frequency with which women use pregnancy tests throughout their reproductive years, they represent today one of the most commonly utilized immunoassays.[4] In other medical contexts, hCG plays a vital therapeutic role for in vitro fertilization and is a significant tumor marker across various cancers, including testicular, ovarian, and trophoblastic tumors.[5] Quantitative and specific hCG tests are thus indispensable for both pregnancy and disease management purposes. The development of corresponding tests is associated with different requirements in terms of sensitivity ranges and the need for detecting various modified forms of hCG.[6] All hCG tests are antibody-based immunoassays designed to distinguish hCGfrom closely related hormones such as luteinizing hormone (LH), follicle-stimulating hormone (FSH), and thyroid-stimulating hormone (TSH). While these hormones share identical α-chains with hCG, their distinct β-chains confer unique biological activities despite significant sequence homology with hCG (e.g., LH shares ~80% sequence identity). Accurate hCG tests depend on access to specific antibodies displaying no or minimal cross-reactivity with the other hormones.[7] Developing such antibodies, in turn, depends on a comprehensive structural mapping of all isoforms to identify proteotypic and solvent-accessible epitopes. This is further complicated by the wide range of hCG

variants differing in glycosylation state and fragment size.[8] In addition, antibody-based assays suffer from inherent challenges such as complicated manufacturing, suboptimal accuracy, sensitivity to adverse storing conditions, and restriction to single use. This has led to an emerging need for robust and readily available recognition elements as sustainable alternative antibodies.[9-11]

In recent years, molecularly imprinted polymers (MIPs) have emerged as promising robust synthetic antibodies for detecting fluid biomarkers.[12-15] These are prepared in the presence of a template that, post-removal, leaves behind binding sites with template-complementary shapes and functionalities. MIPs are robust and stable, negating the need for costly, temperature-controlled supply chains. Meanwhile, they exhibit molecular recognition properties comparable with antibodies, are inexpensive to produce, and are made using animal-free methods. Moreover, unaffected by harsh cleaning conditions, MIPs are reusable, potentially paving the way for more sustainable diagnostic tools.[16, 17] MIPs adapted for diagnostic applications are preferably nanoparticles or nanogels produced by precipitation, emulsion, or graft polymerization,[13, 14, 18] and thin-film materials[19] that exhibit homogenous binding sites due to the spatial restrictions imposed by the limited film thickness or nanoparticle radius. Following a quasi-generic protocol, polyacrylamide-gel-based nanogels can now be manufactured to target well-established antigens.[20-22] Like antibodies, these binders can bind biological targets ranging from small to large molecules and have been implemented in sensor and assay formats. This notable progress stems from recent advances in polymer, colloid, and host-guest chemistry, particularly through the application of epitope imprinting[22-26] combined with solid-phase[27, 28] or dispersed phase synthesis using magnetic template carriers[29, 30][31]. In the latter methods, the template is strategically immobilized in a site-directed orientation on non-porous glass beads or magnetic nanoparticles, respectively. Subsequently, high dilution polymerization of appropriate water-soluble monomers occurs, resulting in polymers partially adhering to the surface of the template carriers.

The magnetic templating method (Fig. 1) is preferred for high-yielding synthesis of epitope imprinted nanoparticles targeting hCG.

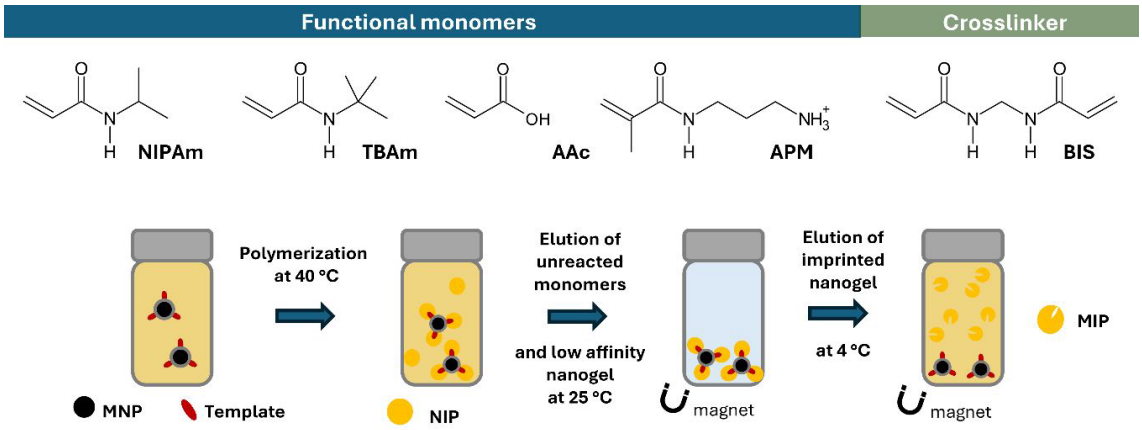

Fig. 1. Monomers used to synthesize nanogels for hCG recognition and principle of hCGepitope imprinting exploiting dispersions of magnetized templates to produce imprinted nanogels.

Similar to antibody-antigen interactions, the epitope refers to a short, solvent-exposed peptide sequence (8-20 amino acids), acting as an antigenic determinant, thus constituting the specific site on the protein surface interacting with the MIP. Preferred epitopes are linear solvent-exposed C- or N-terminal sequences or internal conformationally defined loop structures. Moreover, the epitopes should be free from interfering post-translational modifications and generate adequate affinity and specificity for the target hormone, in this case, allowing detection of hCG levels in the range 10 pM – 1.0 µM and absence of crossreactivity with luteinizing hormone (LH). Most hCG-reactive antibodies bind to assembled discontinuous epitopes and rarely to linear continuous sequences.[8, 32] Two exceptions are the C-terminal peptide (βCTP) of the β-chain, aa 135-145 (PGPSDTPILPQ = PQ), and the β-chain loop structure sequence aa 66-80 (SIRLPGCPRGVNPVV = SV) (Fig. 2A). βCTP is a flexible terminal sequence lacking a defined secondary structure. Hence, its immunogenicity is limited, constraining the production of high-affinity antibodies. Given that βCTP is lacking in LH, monoclonal antibodies against this sequence show high selectivity to hCG versus LH and have found use in various commercial sandwich immunoassays.[33] Interestingly, glycosylation of this sequence at Ser138 did not seem to influence affinity for this epitope. [34] On

the other hand, the β-chain loop structure sequence aa 66-80 is a highly conserved motif present in all hCG variants that has been proposed as an ideal epitope for developing a universal, single epitope hCG assay. Indeed, monoclonal antibodies recognizing this sequence show an exceptionally high target selectivity with only minor cross-reactivity with the homologous LH fragment (aa 86-100) that features an identical sequence except for Asn77, which in LH corresponds to Asp. This reflects the high performance of the corresponding monoclonal antibodies.[35]

In this report, we used these two immunogenic sequences (SV and PQ) as templates for preparing high-affinity polymer-based receptors for hCG. Molecular dynamics simulations confirmed that the templates retain their mimotopic conformations within a prepolymerization mixture environment, thus being suitable for imprinting cavities capable of hCG recognition. The obtained MIPs recognize their templates with high affinities when used as receptors in an SPR-based biosensor or as capture agents in a sandwich assay. Importantly, we demonstrate comparable or improved performance over a commercial ELISA regarding sensitivity, precision, and suppressed LH interference.

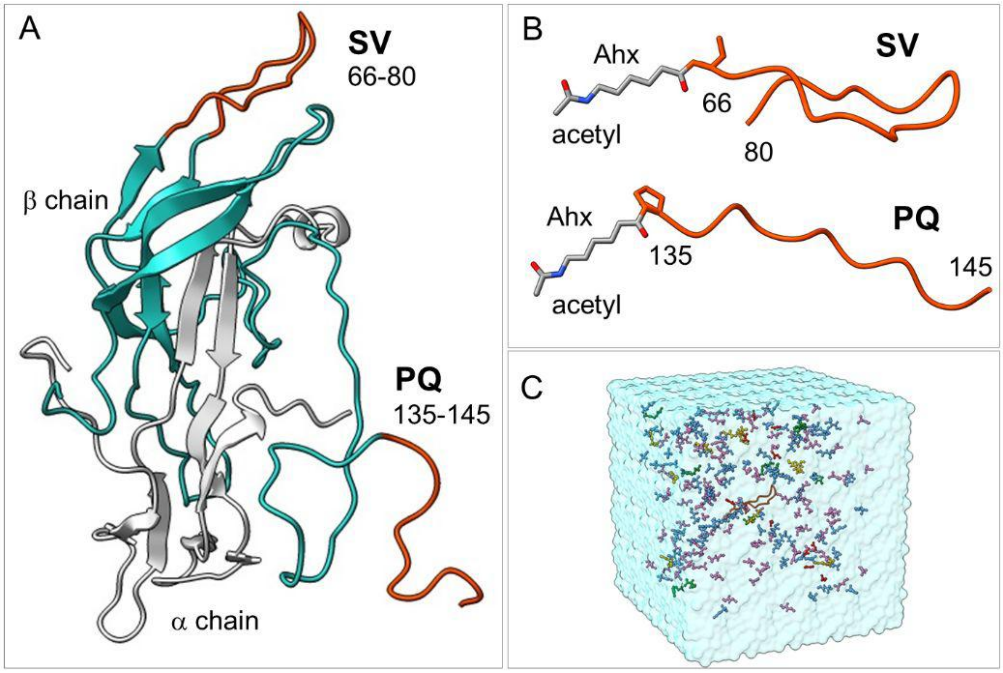

Fig. 2. (A) Structure of the full hCG hormone in which the epitopes SV and PQ are highlighted. SV corresponds to the β-chain loop residues 66-80 (SIRLPGCPRGVNPVV). PQ is the C-terminal peptide of the β-chain, corresponding to residues 135-145 (PGPSDTPILPQ). (B) Structures of the SV and PQ peptides conjugated to the N-acetylated- 6-aminohexanoyl (Ahx) moiety at the N-termini. (C) MD simulation box used to evaluate the conformational properties of the peptide templates (Ahx-SV or Ahx-PQ) within a prepolymerization mixture environment. The simulated systems were built by placing thetemplates Ahx-SV or Ahx-PQ at the center of the box surrounded by 200 monomers in proportions consistent with the experimental setup and explicit solvent molecules.

MATERIALS AND METHODS

Reagents

Ferric chloride hexahydrate ($FeCl_3 \cdot 6H_2O$), sodium acetate, polyethylene glycol 6000 (PEG), sulfuric acid, glycine and sodium dodecyl sulfate (SDS) were obtained from Merck. Ethylene glycol, ammonium hydroxide 25%, triethylamine (TEA), (3-aminopropyl)trimethoxysilane (APTMS), succinic anhydride, 1-ethyl-3-(3-dimethylaminopropyl)-carbodiimide hydrochloride (EDC), N-hydroxysuccinimide (NHS), ammonium persulfate (APS), N,N,N′,N′-tetramethylethylenediamine (TEMED), N-isopropylacrylamide (NIPAm), N-tertbutylacrylamide (TBAm), acrylic acid (AA), tetraethyl orthosilicate (TEOS), phosphatebuffered saline (PBS), ethanolamine hydrochloride, 16-mercaptohexadecanoic acid (MHA), 11-mercapto-1-undecanol (MU), acetic acid, sodium chloride (HCl), triethylamine, 4-(2- hydroxyethyl)piperazine-1-ethane-sulfonic acid (HEPES), 2-[morpholino]ethanesulfonic acid (MES), albumin from Bovine Serum (BSA), human chorionic gonadotropin (hCG) and luteinizing hormone (LH) were obtained from Sigma-Aldrich. N,N-Dimethylformamide (DMF), acetone, hydrochloric acid (HCl) and tetrahydrofuran (THF) were purchased from VWR. N,N′-methylene-bis-acrylamide (MBAm) was obtained from Alfa Aesar, N-(3- aminopropyl)methacrylamide hydrochloride (APM) was obtained from Polysciences Inc. Ethanol was obtained from Solveco. Oligo Binding Buffer (50 mM Na_2PO_4, pH 8.5, 1 mM EDTA), EveryBlot blocking buffer was obtained from Bio-Rad. 6-Aminohexanoyl-$hCG_{\beta 60\text{-}80}$ (Ahx-SIRLPGCPRGVNPVV) and 6-Aminohexanoyl-$hCG_{\beta 135\text{-}145}$ (Ahx-PGPSDTPILPQ) (> 95%) were purchased from Lifetein LLC (New Jersey, US). N-fluoresceinacrylamide was synthesized as reported previously.[36] Alpha hCG mAb antibody, anti-mouse immunoglobulins/HRP solution, 3,3’,5,5’-Tetramethylbenzidine (TMB), tween 20, uncoated human hCG (Chorionic Gonadotropin) ELISA kit and ancillary reagent kit were obtained from Elabscience

(Wuhan, Hubei, China). Fluoresceine was purchased from TCI, and Tween 20 was obtained from AppliChem.

Apparatus

Molecular dynamics simulations. MD-simulations were carried out in a computer cluster equipped with (a) 2 Supermicro Quantum TXR413-1500R servers with 2 Intel Xeon® processors E52620, and 16 NVIDIA GeForce GTX1080 GPUs and (b) 2 TensorEX TS4- 1598415-AMB servers with 2 Intel Xeon Silver® processors and 16 NVIDIA RTC2080 GPUs.

Dynamic light scattering (DLS) and zeta-potential. Effective hydrodynamic diameters (dh) of the particles were determined by dynamic light scattering (DLS) with a Zetasizer Ultra (Malvern Panalytical) equipped with a He-Ne laser (688 nm) and set to backscatter mode, with measurements of samples performed in triplicate at 25 °C. Data was analyzed using the ZS Xplorer software.

Fourier-transform Infrared Spectroscopy (FTIR) spectra were collected using a Nicolet 6400, equipped with a DTGS detector. The smartiTR accessory was used to characterize dried modified magnetic nanoparticles. 500 spectra were collected at resolution 4. Compressed air was continuously run through the instrument during and before the measurements. Baseline correction and data management were performed with the OMNIC 6 software.

Surface plasmon resonance (SPR). The affinity of the imprinted nanoparticles for the epitope target was investigated using a Reichert 2 SPR system (Reichert Technologies, Buffalo, USA) with an attached autosampler and degasser. The specificity of the imprinted nanomaterial was investigated by binding a non-target peptide of similar shape and size.

Quartz crystal microbalance (QCM) measurements. The interaction between the peptide/protein and nanogels was analyzed with Q-Sense QCM-D E4 unit equipped with a standard flow module (Biolin Scientific AB, Sweden). The sensors used for the experiments were the

QCM5140TiAu120QCM5140TiAu120-050-Q (5 MHz) from QuartzQuartz Pro AB (Jarfalla, Sweden). All sensors were cleaned in line with the manufacturer's recommendations.

Experimental

Synthesis of Magnetic Nanoparticles

Magnetic nanoparticles (MNP) were obtained by solvothermal synthesis, as reported by Mahajan et al.[37] Briefly, $FeCl_3 \cdot 6H_2O$ (16.6 mmol), sodium acetate (95.0 mmol), SDS (21.8 mmol) and PEG 6000 (2.7 g) were dissolved in 150 mL of ethylene glycol. The mixture was magnetically stirred at 100 °C for 30 min and then transferred to a 150 mL Teflon-lined stainless-steel autoclave. The autoclave was sealed and heated at 180 °C for 24 h. Then, the container was cooled to room temperature, and the MNPs were separated by a magnet. The solid was then washed five times with deionized water, three times with 100 mL of ethanol, three times with 100 mL of acetone, and then dried in a desiccator under vacuum at 22 °C for 24 h. Subsequently, 1000 mg of MNPs were dispersed in 1 L of 80 % ethanol containing 0.25 mM ammonium hydroxide, and ultrasonicated for 2 min at 50 % intensity using a sonifier (BRANSON). A 0.5 M TEOS solution was then added, and the reaction mixture was shaken in an orbital shaker for 6 h. The obtained nanoparticles were washed with deionized water until neutral pH, followed by three washes with 100 mL of ethanol, and dried in a desiccator over activated silica at 22 °C for 24 h. The produced silica-coated nanoparticles (MNP@Si,1000 mg) were surface-functionalized by sonication in a bath sonicator for 2 h with APTMS (57 mM) in 75% ethanol. The resulting primary amine-modified MNPs ($MNPNH_2$) were washed three times with ethanol and dried in a 37 °C oven overnight. Particles were further functionalized with succinic anhydride (2.1 M) in DMF by sonication in a bath for 3 h. The final product (MNPs-COOH) was washed ten times with deionized water, three times with ethanol, and dried at 37 °C oven.

Template conjugation to magnetic nanoparticles (MNPs)

MNPs-COOH (100 mg) was placed into a 20 mL vial along with 6 mL of deionized water at room temperature, followed by sonication for 30 s twice at 35 % amplitude. The carboxylic groups on the surface of the magnetic nanoparticles were activated by adding 2 mL of freshly prepared EDC solution (100 mg·mL^{-1}) and 2 mL of NHS solution (62.5 mg·mL^{-1}) in deionized water. The mixture was then shaken on an orbital shaker for 1 h at room temperature. Afterward, the activated magnetic nanoparticles were washed twice with 10 mL of deionized water and once with 5 mL of 10 mM PBS (pH 7.4). The immobilization of Ahx- PQ and Ahx-SV was carried out by adding 5 mL of epitope solution (0.50 mg·mL^{-1} in 10 mM PBS, pH 7.4) to the vial, which was then shaken at room temperature overnight. Subsequently, the peptide conjugation was assessed via the fluorescamine test.[38, 39] A portion of the initial supernatant (100 µL) from the reaction was mixed with 25 µL of Fluorescamine solution (0.50 mg·mL^{-1} in acetone). Fluorescence was then measured (λ_{ex} = 400, λ_{em} = 510 nm), and the specific amount of conjugated peptide was calculated from the reduced signal upon solution depletion. To remove any excess epitope, the MNPs were collected using an external magnet, rinsed with PBS and deionized water, then suspended in 5 mL of deionized water and stored at 4°C.

Preparation of molecularly imprinted nanogels using magnetic templates

Monomer feed ratios used to synthesize the epitope-imprinted MIPs are reported in Table S2. Synthesis of MIP-PQ was conducted as follows. A pre-polymerization mixture with a total monomer concentration of 10 mM for MIP-PQ and 20 mM for MIP-SV was prepared by dissolving NIPAm (5.43 mg, 48 µmol), BIS (0.31 mg, 2 µmol), TBAm (5.09 mg, 40 µmol dissolved in 1 mL of ethanol), APMA (1.79 mg, 10 µmol), and 0.4 mg of Nfluoresceinylacrylamide (dissolved in ethanol) in deionized water (9 mL) in a 20 mL vial. The pre-polymerization mixture was homogenized for 30 min, followed by the addition of 1 mL of 25 mg·mL^{-1} MNP-SV or MNP-PQ

dispersion. The mixture was stirred at room temperature under N_2 atmosphere for 15 min. Then, 0.26 mmol of ammonium persulfate (APS) and 0.40 mmol of N,N,N',N'-tetramethylethylenediamine (TEMED) were added and the dispersion was left overnight at 40 °C under constant stirring (480 rpm). Afterward, the particles were collected using an external magnet and washed with deionized water (5 × 10 mL) at 40°C to remove unreacted functional monomers and low-affinity nanoparticles. Finally, the high-affinity imprinted nanogels were obtained by adding 4 mL MQ-water to the magnetic particles and stirring at 4°C for 4 hours. The elution step was performed by collecting the first 4 mL, and this process was repeated once on the magnetic nanoparticles by adding an additional 1 mL of 1 mM PBS and incubating overnight at 4°C. Thus, the elution process resulted in a total volume of 5 mL of imprinted nanogel solution. Concentrations of the nanogel solutions were calculated by taking 400 µL of the solution (in triplicate) and evaporating to dryness. The mass of the dried particles was then measured, and the amount was multiplied by 2.5 to give the concentration in µg mL^{-1}.

DLS measurements

To evaluate the hydrodynamic size of nanogels, a 100 µg mL^{-1} dispersion of the MIP nanogels in water was prepared. The sample was sonicated in a bath sonicator for 30 min and left at 4°C for 2h. To evaluate MNP synthesis and surface modifications, a 50 µg mL^{-1} suspension of the MNPs was prepared in water. Before the measurement samples were sonicated 3 times for 10 s at 50 % amplitude. Size and zeta potential measurements were done in triplicates.

Immobilisation of MIP nanogels onto the SPR Sensor Surface

A carboxymethyl dextran hydrogel-coated Au chip (Reichert, USA) was preconditioned within the SPR using a running buffer consisting of PBS (0.010 M) and 0.010 % Tween 20 at pH 7.4, at a flow

rate of 10 μL min^{-1}. The carboxylic acid groups on the dextran chip were activated with an injection of 1 mL of aqueous solution containing 40 mg EDC and 10 mg NHS passed over the chip (6 min at 10 μL min-[1]). The MIP nanogels (approximately 300 μg), were activated by dissolving in 1 mL of 10 mM sodium acetate in PBST solution. This was injected over the left channel (working channel) of the chip for 1 minute. The amine groups of the MIP nanogels react with the functionalized surface of the chip, leading to the covalent immobilization of the nanoparticles. A quenching solution of ethanolamine (1 M at pH 8.5) was injected over both channels (working and reference) for 8 min, followed by a continuous flow of PBST at 10 μL min^{-1}. All injections were taken from a stable baseline.

Kinetic interaction analysis

The kinetic analysis for the affinity of the target peptide to the MIP nanogels was performed in a set pattern of a 2 min association (PBST with the analyte in a concentration range of 4- 64 nM), 5-min dissociation (PBST only) and a regeneration cycle (regeneration buffer 10 mM Glycine-HCl, pH 2 for 1 min) followed by a final stabilization cycle (PBST for 1 min). An initial injection of blank PBST was used as the first run, with increasing analyte concentration for subsequent runs. After the analyses were completed, signals from the reference channel were subtracted from signals from the working channel. Selectivity of the MIP nanogels was investigated by repeating the kinetic analysis, but with a non-target analyte with the same concentration range (4-64 nM). All experiments were performed in triplicate (n=3). The SPR responses were fitted to a 1:1 Langmuir fit bio-interaction (BI) model using the Reichert TraceDrawer software. The association rate constants (ka), dissociation rate constants (kd), and maximum binding (Bmax) were fitted globally, whereas the BI signal was fitted locally. Equilibrium dissociation constants (KD) were calculated by k_d/k_a. For each MIP nanogel/analyte epitope combination, a calibration curve was generated across the

concentration range 4-64 nM, using the SPR fitted curve maxima. From this information, a theoretical limit of detection (LOD) was calculated.

QCM experiments

Sensor chip modification. After washing with piranha solution (H_2SO_4:H_2O_2, 4:1), a gold-coated QCM sensor chip was dried with N_2. The chip, cleaned via plasma cleaner for 5 min, was then placed in a petri dish and immersed in 4 mL of a thiol solution composed of 1 mM 16-Mercaptohexadecanoic acid (MHA) and 1 mM 11-Mercapto-1-undecanol (MU) in absolute ethanol:acetic acid (ratio 9:1) for 18 h at room temperature in the dark. Afterward, the chip was washed three times with absolute ethanol and 10 mM MES buffer (pH 6) and dried with N_2. To activate the carboxylic group of MHA, 100 µL of a sulfo-NHS:EDC mixture (1:1, 100 mg·mL^{-1} in MES buffer) was introduced for 30 min, followed by washing with 10 mM PBS and drying with N_2. The immobilization of the epitope was conducted using a standard solution of Ahx-PQ or Ahx-SV prepared at a concentration of 1 mg·mL^{-1} in 10 mM PBS (pH 7,4). Immobilization of hCG was carried out using a protein solution at 10 µg·mL^{-1} in PBS. The protein was injected into a QCM-D instrument to verify the bound amount. Additionally, to confirm the specificity of imprinted nanogels, the same procedure was conducted for LH. QCM measurements. The experiments aimed at examining the binding of imprinted nanogels with PQ, SV and hCG were carried out utilizing various concentrations of MIP-PQ or MIP-SV (12.5, 25, 50, 100 µg·mL^{-1}) prepared through the same procedure employed for DLS measurements. The fundamental frequency was approximately 5 MHz and the baseline frequency signal was calibrated by injecting a running buffer solution composed of 1 mM PBS and Tween 20 (0.005%, v/v) for 1 hour at a flow rate of 10 µL·min^{-1} until the frequency signal response stabilized within ± 0.2 Hz/5 min. Using the same flow rate, the samples were introduced in QCM-D instrument for 23 min for each concentration. The frequency variations attributed to binding with analytes were recorded in accordance with the frequency signal response. To evaluate the specificity of MIP-PQ and MIP-SV in detecting hCG and LH, the

nanogels were immobilized on QCM sensor chips, and the coupling was analyzed using the same dilutions as before. The apparent molarities of nanogels were determined using Equation 1.

Equation 1 $$[M(app)] = \frac{6}{\pi N_A d^3 \rho} X$$

where, d is the hydrodynamic diameter of particles, N_A is Avogadro's constant ($6.023 \cdot 10^{23}$ mol^{-1}), X is the nanogel concentration in $g \cdot mL^{-1}$ ($1 \cdot 10^{-4}$ $g \cdot mL^{-1}$) and ρ is the polymer density.

Microplate assays for hCG detection

ELISA kit protocol for hCG quantification. A commercial ELISA kit was used for comparative purposes to detect and quantify hCG. The experimental protocol provided by the supplier was followed for hCG determination. Briefly, 100 µL of capture antibody (1:750) was immobilized overnight at 2 – 8 °C on a clean polystyrene microplate. The supernatant was discarded, and the plates were treated with 200 µL of ELISA plate-blocking buffer for 60 min at 37 °C. After discarding the blocking buffer, 100 µL of hCG standard solutions (6.3 - 200 $mIU \cdot mL^{-1}$), containing a constant concentration of LH (100 $mIU \cdot mL^{-1}$), were added in duplicates. The plate was incubated for 90 min at 37 °C. Subsequently, 100 µL of Biotinylated Detection Antibody (1:750) was added to each well and incubated for 60 min at 37 °C. The wells were then washed three times with the wash buffer provided by the supplier. Next, the wells were treated with 100 µL of HRP conjugate solution (1:750) and incubated for 30 min at 37 °C, followed by five washes with 350 µL of the wash buffer. Finally, 90 µL of 3.3'.5.5'-Tetramethylbenzidine (TMB) was added to each well and incubated for 20 min at 37 °C. The enzymatic reaction was terminated by adding 50 µL of stop solution (sulfuric acid 5 %) to each well. Absorbance was read at 450 nm using a microplate reader (Tecan, Safire).

MIP-based ELISA sandwich test for hCG quantification. The immobilization of nanoMIP dispersion was carried out by drying 40 µL the dispersion (0.06 $mg \cdot mL^{-1}$ in HEPES 10 mM, NaCl 150 mM and 0.005% Tween 20) overnight at 37 °C on a clean polystyrene microplate. The plate was washed twice with 250 µL of PBS (pH 7.4), then each well was incubated with a blocking solution (1 % BSA, 1 % Tween 20 in PBS pH 7.4) for 120 min at room temperature and washed three times with PBS (pH 7.4). After discarding the buffer, 100 µL of hCG standard solutions (6.3 - 200 $mIU \cdot mL^{-1}$) containing a constant concentration of LH (100 $mIU \cdot mL^{-1}$) were added in duplicates and incubated for 90 min at 37 °C. Following this, 100 µL of Biotinylated Detection Antibody (1:750) was added to each well and incubated for 60 min at 37 °C. The plates were washed three times with the wash buffer provided by the supplier, treated with 100 µL of HRP conjugate solution (1:750), and incubated for 30 min at 37 °C, followed by five washes with 350 µL of the wash buffer. Each well was treated with 90 µL of TMB and incubated for 20 min at 37 °C. The enzymatic reaction was terminated by adding 50 µL of stop solution (sulfuric acid 5%) to each well, and absorbance was read at 450 nm using a microplate reader.

Molecular dynamics simulations

The coordinates of the full hCG protein were retrieved from the Protein Data Bank server (PDB code 1HRP).[40] The missing protein segments were built using the Chimera X interface to Modeller tools. The coordinates of the epitopes SV and PQ were obtained from residues 60-80 and 135-145 of the β-chain, respectively. Both epitopes were modified at the N-terminal end by attaching an N-acetylated-6-aminohexanoyl (Ahx) moiety. The modified epitopes were placed at the center of a cubic box of 80 Å side and surrounded by 200 randomly located monomers in proportions consistent with the formulations reported in this work using the PACKMOL software.[41] The simulated mixtures were neutralized with Na^+ or Cl^- ions and solvated in a cubic box of explicit OPC waters considering an outer layer of 5 Å measured from the outermost atoms.

The ff19SB force field was used to model the peptidic segments, whereas the Ahx moieties were modeled using parameters consistent with the gaff2 force field with AM1-BCC charges. MD simulations were carried out using the following protocol: (a) 1500 steepest descent minimization steps followed by 3500 conjugate gradient minimization steps for water molecules relaxation, (b) 1500 steepest descent minimization steps followed by 6500 conjugate gradient minimization steps for the entire system, (c) 500 ps of progressive NVT heating from 0 to 300 K, (d) 10 ns of NPT equilibrium at 300 K to ensure density equilibration, (e) 20 ns of NPT equilibrium at 300 K, and finally (f) 150 ns of NPT production dynamics at 300 K and 1 bar from which production data were collected. During MD simulations the cutoff for non-bonded terms was 10 Å, long-range electrostatics were treated using the Particle-Mesh Ewald approach, and the SHAKE algorithm was employed to constrain all bonds involving hydrogen. Positional restraints were applied to the terminal acetyl group of the Ahx moiety throughout the simulation protocol to mimic the immobilization of the epitopes to the solid support through Ahx. All Calculations were carried out using the pmemd.CUDA software implemented in AMBER20. Trajectory analysis was carried out with the CPPTRAJ[42] and VMD[43] software.

RESULTS AND DISCUSSION

This study reports the development of molecularly imprinted polymer nanogels (MIPs) exploiting an epitope-based approach for hCG detection. To this aim, we focused on the 15aa sequence corresponding to the β3-loop of the β -subunit from residues 60 to 80 (SIRLPGCPRGVNPVV = SV) and the C-terminal undecapeptide of the β -chain from residues 135 to 145 (PGPSDTPILPQ = PQ) as templates. To confirm that these sequences properly mimic the three-dimensional conformation of the corresponding protein epitopes, we performed molecular dynamics (MD) simulations.

Molecular Dynamics Simulations

MD simulations were used to investigate the conformational properties of the SV and PQ segments in the full hCG protein and in the context of pre-polymerization formulations. This is relevant to confirm whether the selected templates preserve the structural features required for imprinting molecular cavities capable of efficiently recognizing the full protein. To that end, we conducted MD simulations on the structures of the SV and PQ peptides conjugated with the Ahx moiety (Ahx-SV and Ahx-PQ, respectively) (Fig. 2B) and surrounded by a mixture of functional monomers and explicit solvent molecules in proportions consistent with the experimental setting reported in this work (Fig. 2C). Parallel simulations were carried out on the structure of the full hCG protein in water to evaluate the intrinsic dynamic properties of the SV and PQ epitopes.

The global conformational properties of the template peptides Ahx-SV and Ahx-PQ and the corresponding epitopes in the hCG protein were evaluated from root-mean-square deviation (RMSD) calculations on the peptide backbone atoms throughout each simulation run, using the epitope coordinates in the 1HRP crystallographic model as the reference structure (Fig. 3A). RMSD

data indicate that the template peptides Ahx-SV and Ahx-PQ have similar mobilities as the corresponding epitopes in the full protein, with PQ being more flexible than SV. The size and compactness of each peptide were evaluated from radius of gyration (Rg) calculations along each MD trajectory (Fig. 3B). SV has very similar Rg distributions in the Ahx-SV template and in the full hCG protein, whereas PQ has slightly larger Rg values in the Ahx-PQ system, suggesting more extended conformations than in the hCG epitope. The structural consistency between the SV peptide in Ahx-SV and the full protein was confirmed by the visual inspection of the conformations achieved by the sequence in their MD trajectories (Fig. 3B,C). SV retained the loop structure required to imprint cavities suitable for hCG recognition, which is a relevant outcome to support the choice of this segment as a template for the synthesis of molecularly imprinted nanogels. In the case of PQ, the peptide adopts more extended conformations in the Ahx-PQ than in the hCG protein, as inferred from R_g data. Regarding the intrinsic arrangement of the peptide sequences, DSSP secondary structure analysis confirmed that SV and PQ are highly disordered peptides that exist mostly in turn and bend states both in the Ahx-conjugated templates and the full hCG protein (Fig. 3D). This conformational plasticity is relevant for the epitopes to adapt to imprinted cavities of variable size and shape, which supports the choice of SV and PQ as template peptides in our experimental design.

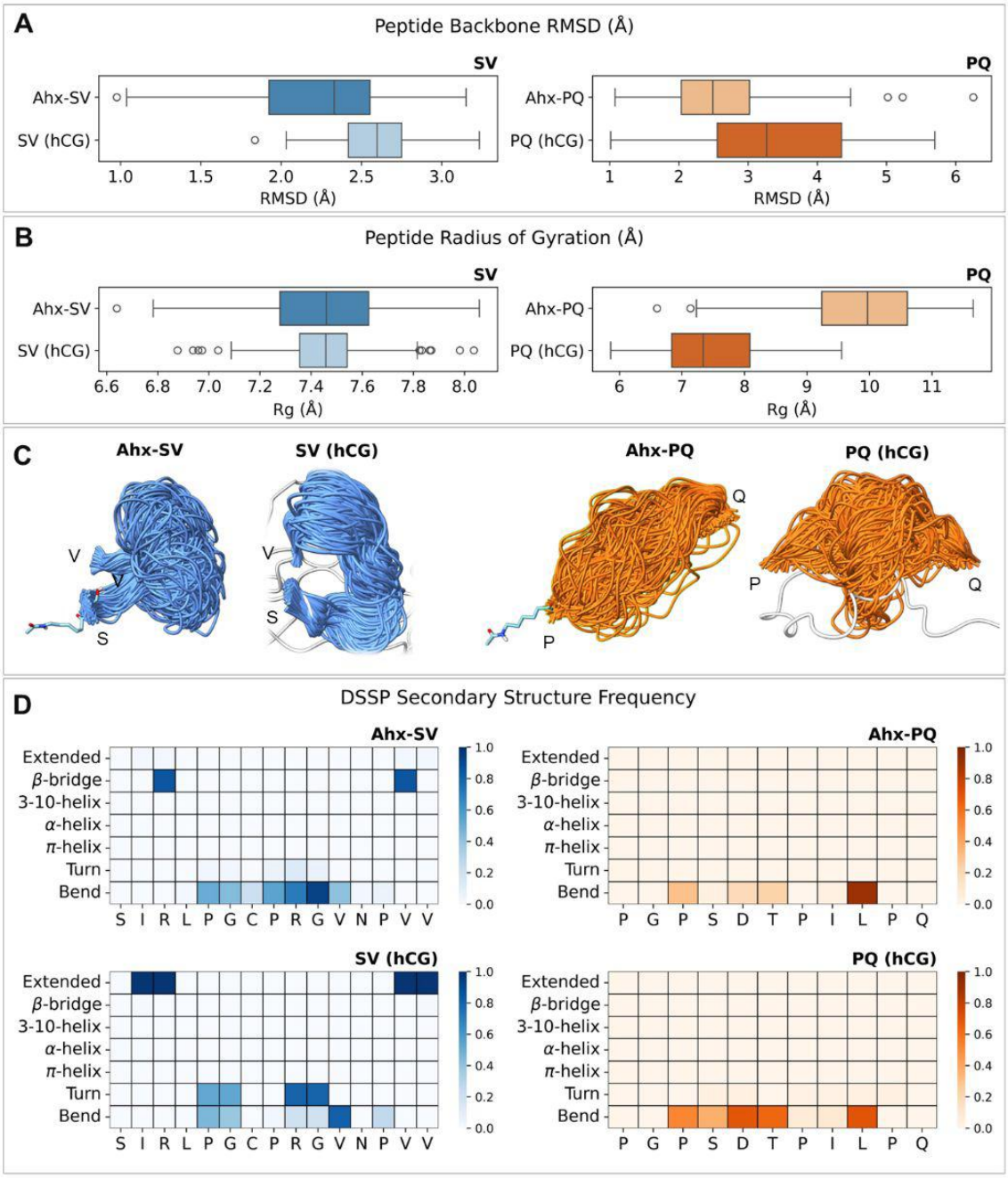

Fig. 3. (A) Root-mean-square deviation RMSD (Å) distributions calculated for the peptide backbone in Ahx-SV and Ahx-PQ and the corresponding epitopes in the hCG protein. Data was collected from the analysis of 150 ns MD simulations in pre-polymerization mixtures (Ahx-SV and Ahx-PQ) or water (full hCG), using the coordinates of the SV and PQ epitopes in the 1HRP crystallographic structure as reference models. (B) Peptide radius of gyration R_g (Å) for the SV and PQ sequences in Ahx-SV, Ahx-PQ, and the full hCG protein calculated from 150 ns MD trajectories. (C) Structural representations of the backbone conformations achieved by the SV and PQ sequences in Ahx-SV, Ahx-PQ, and the full hCG protein throughout 150 MD trajectories. Structures are displayed from MD trajectories aligned to the first and last amino acids of each sequence. (D) Heatmaps for the frequency of secondary structure assignations according to DSSP analysis on SV and PQ sequences in Ahx-SV, Ahx-PQ, and the full hCG protein throughout 150 MD trajectories.

Besides conformational features, we used MD simulations to estimate the strength of peptidemonomer interactions within the pre-polymerization mixtures under a LIE approach. This method decomposes the total interaction energy between a molecule and its surrounding environment (E_{total}) as the sum of electrostatic (E_{lec}) and van der Waals (E_{vdW}) energy terms. Energy components were calculated between all atoms in the peptides with all atoms in the surrounding monomer mixtures with a distance cutoff of 12 Å along the entire MD trajectories (Fig. 4A). For Ahx-SV, the interaction with the monomer mixture is almost equally driven by the contributions from E_{lec} and E_{vdW} terms. On the other hand, the interaction of the monomer mixture with Ahx-PQ shows a stronger E_{lec} component over E_{vdW}. A possible explanation for this effect arises from the presence of the highly polar SDT triad in PQ, which can engage in strong electrostatic or hydrogen bonding interactions with opposite-charged moieties of the surrounding monomers. Added to the energetics of peptidemonomer interactions, we examined the organization of the pre-polymerization mixtures by counting the number of monomers interacting with the peptides at distances ≤ 5 Å throughout the MD trajectories (Fig. 4B). Distribution data reveals that the monomer organization mostly relies on TBAm and NIPAm, which are the monomers with higher proportions in both monomer mixtures.

Template magnetization

Magnetic nanoparticles were synthesized via solvothermal method and subsequently surface-functionalized to yield carboxyl-terminated magnetic nanoparticles (MNP-COOH). The MNP-COOH particles were conjugated with the peptides SV and PQ via their Ahx linkers, resulting in the template-conjugated magnetic nanoparticles referred to as MNPs-SV and MNPs-PQ. The surface coverages of the peptides were estimated to be 8.3 and 11.7 $\mu mol \cdot g^{-1}$ for Ahx-SV and Ahx-PQ, respectively, which are comparable to coverages reported elsewhere.[22, 30, 31] DLS measurements (Table 1) confirmed that the template-conjugated MNPs maintained nanoscale

hydrodynamic radii (ca 280 nm) and exhibited Zeta potential changes agreeing with the net charges of the epitopes (Table S1).

System	Average size (d.nm)	Polydispersisty index	Z-potential (mV)
MNP	189 ± 1.0	0.080 ± 0.01	17.7 ± 0.9
MNP@Si	284 ± 8.0	0.17 ± 0.02	-27.7 ± 0.1
MNP-NH_2	274 ± 1.0	0.16 ±0.02	25.9 ± 0.6
MNP-COOH	259 ± 4.0	0.090 ± 0.04	-33.1 ± 1.2
MNP-PQ	432 ± 8.0	0.22 ± 0.02	-40.6 ± 0.4
MNP-SV	670 ± 23	0.22 ± 0.02	-25.7 ± 0.2
MIP-SV	41.0 ± 14	0.22 ± 0.02	-22.0 ± 1.1
MIP-PQ	100 ± 2.0	0.16±0.03	15.0 ± 0.4

Table 1. Hydrodynamic radii (nm), PI, and Z-potential (mV) of the MNPs and MIPs reported in this work.

MIP synthesis

MIPs were synthesized by free radical polymerization of acrylamide monomers in the presence of the template-conjugated MNPs. The monomers were rationally selected based on previous designs, to enable diverse intermolecular interactions with the immobilized peptides. The template peptides SV (SIRLPGCPRGVNPVV) and PQ (PGPSDTPILPQ) comprise 15 and 11 amino acids, respectively. SV contains two positively charged and eight hydrophobic amino acids reflected in both a high pI and Gravy index (10.9 and 0.30). On the other hand, PQ features one negatively charged and seven hydrophobic residues resulting in a low pI and Gravy index (3.1 and -0.64) (Table S1). Building upon previously reported examples, poly-NIPAm-based nanogels were synthesized using a template matching ratio of the charged monomers N-(3-aminopropyl)methacrylamide hydrochloride (APM) and acrylic acid (AA) in addition to the hydrophobic functional monomer N-tert-butylacrylamide (TBAm) (Table S2). Additionally, N,N'-methylenebisacrylamide (BIS) (2 %) was used as a cross-linker, and the fluorescent functional monomer N-fluoresceinylacrylamide (FITCAAm) was doped to allow fluorescent tracking of the

nanogels.[30, 44] The polymeric nanogels were purified by magnetic decantation with pure water, resulting in a mass yields of 633 mg SV-MIP and 153 mg PQ-MIP per gram of MNP carrier. This confirms that mass yields can be dramatically enhanced (>> 100x) using high surface area MNPs as template carriers.[30, 31] The average size, polydispersity index, and Z-potential of the MIP nanogels assessed through DLS (Fig. S1, Table 1) confirmed the nanoscale dimensions, homogeneity, and low aggregation propensity of the prepared materials. Moreover, the MIPs were characterized by FTIR spectroscopy as shown in Fig. S2. FTIR analysis revealed the characteristic amidine group for both MIP-SV and MIP-PQ at 1640 cm^{-1} (amidine 1), 1536 cm^{-1} (amidine 2), and 1223 cm^{-1} (amidine 3). Additionally, symmetric and asymmetric bands for -CH2- are present at 2933 cm^{-1} and 2875 cm^{-1}, respectively. Notably, the band for the carboxyl group, typically observed at 1700 cm^{-1}, is absent. This absence may be attributed to the low concentration, deprotonation of the carboxylic group, or hydrogen bonding. Deprotonation leads to the formation of carboxylate anion that exhibits absorption bands around 1550-1610 cm^{-1} and 1300-1420 cm^{-1}. Hydrogen bonding, on the other hand, can broaden or shift the existing C=O band. In this study, strong bands for amidine 1 and 2 are superimposed and may have merged with the C=O stretching band and potential bands of carboxylate anions.

Kinetic interaction analysis by surface plasmon resonance (SPR)

For a preliminary assessment of the MIP recognition properties, we performed a kinetic interaction analysis using surface plasmon resonance (SPR). Deposition of the nanogels onto the surface of the SPR chip was achieved through amide coupling on pre-functionalized gold surfaces with a carboxymethyl dextran layer.[17, 31] The carboxyl groups on the chip surface were activated by EDC/NHS and conjugated with excess nanogels through the amine functionalities provided by the side chains of the APM moieties. Ethanolamine was then used to deactivate any unreacted carboxyl groups left on the SPR chip surface after nanogel immobilization while washing away the fraction

of unbound nanogel. This deposition method is expected to leave a single nanogel layer on the chip surface with maximum coverage of available binding sites. The nanogel-modified SPR chips were then tested for their binding interactions with solutions of increasing concentrations of the target peptides SV and PQ. The SPR sensograms showing the RU changes occurring upon injections of five different concentrations of the target peptides are displayed in Fig. S3. The overall equilibrium dissociation constant (KD) values for the target interacting with their nanogels were calculated from the curves using a 1:1 kinetic model, leading to 85 nM and 92 nM for PQ and SV, respectively (Table 2). These results are consistent with previously published values for nanogels imprinted for peptides and demonstrate the capacity of MIP-SV and MIPPQ to rebind their template epitopes with high affinity.[31] Cross-reactivity SPR experiments with swapped templates (SV for MIP-PQ-conjugated sensors and PQ for MIP-SV-conjugated sensors) resulted in nearly 4-fold increases in KD values, which support the selectivity of the nanogels for their corresponding target peptides. Nevertheless, both SV and PQ exhibit nonspecific nanomolar dissociation constants to the conjugated sensors, which might arise from intermolecular interactions involving the nanogel surface or the highly polar groups available from the ethanolamine or uncovered carboxymethyl dextran layers on the SPR chip.

MIP	**K_D (nM)**	
	PQ	SV
MIP-PQ	85.0 (± 1.0)	465 (± 25)
MIP-SV	346 (± 42)	92.0 (± 2.0)

Table 2. Calculated equilibrium dissociation constant (KD) of the nanogels from data presented in Fig. S5. All experiments were performed under ambient conditions and with three replicates.

Nanogels binding affinity towards target peptides and proteins assessed by quartz crystal microbalance (QCM)

QCM was used for quantifying the interaction between the nanogels and their epitope templates, the full hCG protein, and the decoy protein LH.[20, 21, 45] For the measurements, we adopted the most

commonly reported technique based on template-modified sensor chips and the MIP injected in the running buffer. First, the sensor surface was modified with a mixed Self-Assembled Monolayer (SAM) of mercaptohexadecanoic acid (MHA) and mercaptoundecanol (MU), the latter serving as a filler for improved ligand accessibility (Fig. S4). Subsequently, the ligands (SV, PQ, hCG or LH) were immobilized through their amine functionalities via EDC/NHS catalyzed coupling. The progression of this step was monitored through changes in resonant frequency, with estimated surface coverages of $4.9 \cdot 10^{-11}$ mol·cm^{-2} and $4.1 \cdot 10^{-11}$ mol·cm^{-2} for PQ and SV, respectively. For hCG and LH, the estimated immobilization ratios were $1.2 \cdot 10^{-12}$ mol·cm^{-2} and $1.3 \cdot 10^{-12}$ mol·cm^{-2}, respectively (Fig. S5).

The epitope-functionalized QCM chips were first used to assess the binding of MIP-PQ and MIP-SV to their corresponding templates (Fig. 5A,B). Increasing concentrations of colloidal MIP solutions were introduced at predetermined time intervals, and the frequency change (□F), which is proportional to mass uptake on the sensor surface, was monitored in real time. Introducing the MIPs elicited pronounced frequency decreases relative to the injection of dispersions of non-imprinted nanoparticles (NIP) of identical chemical composition. This highlights the relevance of the SV- and PQ-imprinted cavities to trigger the template recognition over non-specific intermolecular interactions on the nanogel surface. Parallel experiments with swapped nanogels-chips pairs (MIP-SV against PQ-functionalized chips and MIP-PQ against SV-functionalized chips) also resulted in significant frequency changes compared to NIPs, which suggests the presence of non-specific binding cavities capable of hosting flexible peptide moieties. Apparent dissociation constants (K_D) were estimated for each system by fitting non-equilibrium frequency changes against injection concentration to a Langmuir adsorption isotherm model (Fig. 6A). This analysis yielded a K_D of ca 8.9 and 30 nM for MIP-PQ and MIP-SV for their corresponding peptide templates (Table 3). These values are in the same order of magnitude as those determined by SPR, with expected variations arising from the QCM-associated errors due to a lack of equilibrium during data acquisition. To

demonstrate the binding specificity, we performed a competitive inhibition test by pre-incubating the nanogels with soluble PQ or SV peptides (Fig. 5A,B, labels MIPPQ+ PQ and MIP-SV+SV). Pre-incubation significantly reduced the subsequent binding of MIP-SV and MIP-PQ to the template-functionalized sensors, implying that epitope occupancy of imprinted sites inhibits further nanogel interactions. These results provide compelling evidence that the MIPs achieve the design goal of selective, epitope-specific binding to the templates.

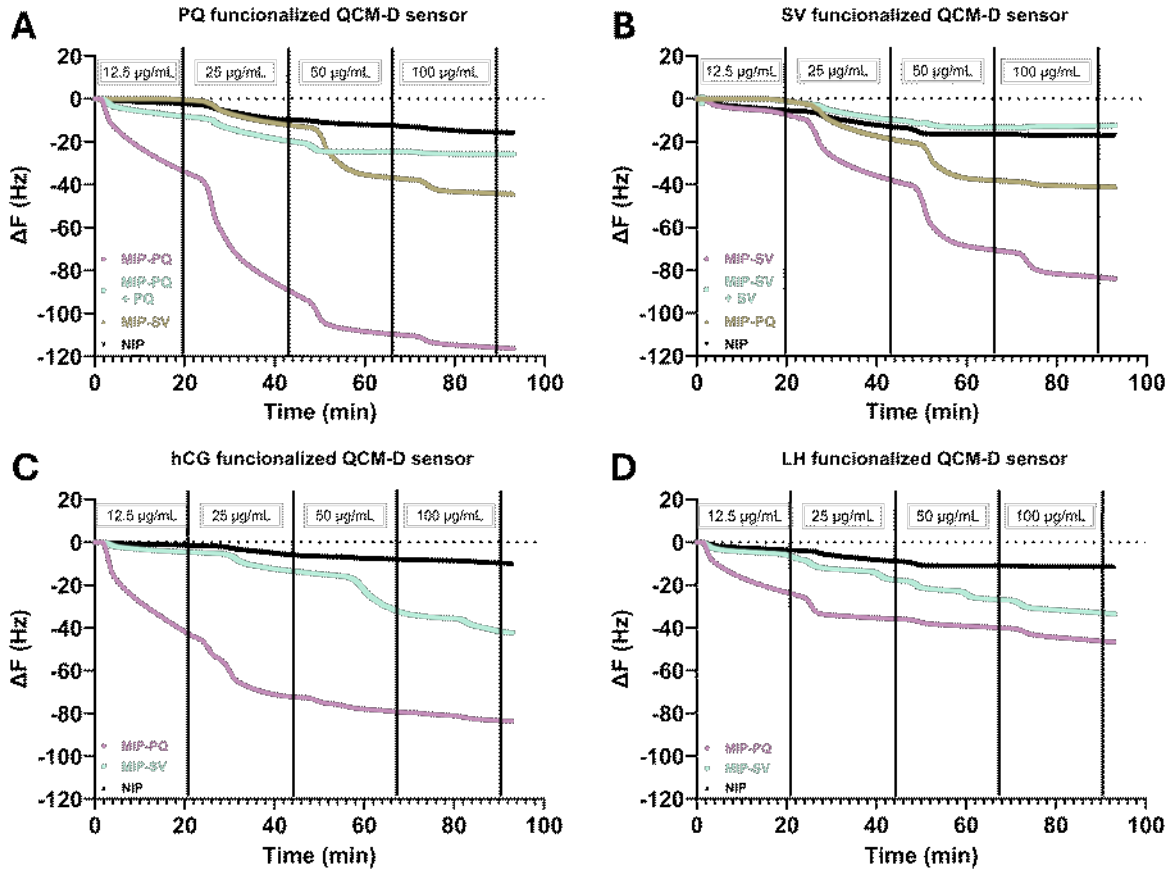

Fig. 5. Real-time resonant frequency changes ΔF (Hz) after repeated injections of MIP-PQ, MIP-SV, and NIP dispersions of increasing concentration on functionalized QCM-D sensor chips with (A) PQ, (B) SV, (C) hCG, and (D) LH. Figures (A) and (B) also show the frequency changes upon injecting nanogels dispersions pre-incubated with 0.1 mg·mL^{-1} peptide solutions (MIP-PQ+PQ and MIP-SV+SV, respectively)

Additional QCM experiments were conducted to assess the nanogel affinity for hCG and LH proteins. To that aim, the two proteins were immobilized on the sensor chips. Following concentration-dependent exposures of MIP-SV and MIP-PQ, the hCG-functionalized sensor led to

pronounced frequency drops, significantly exceeding those of NIPs (Fig. 5C). Apparent KD values to hCG were estimated in 4.4 nM for MIP-PQ and 49 nM for MIP-SV (Table 3) (Fig. 6A). Parallel experiments using the LH-modified sensor chip produced significantly lower resonance frequency drops (Fig. 5D, 6B), highlighting the selectivity of the MIPs towards the target protein hCG. Nevertheless, both MIP-PQ and MIP-SV induce larger frequency changes than NIP, which indicates the presence of surface-binding cavities capable of non-specific interactions. The combined outcomes of QCM experiments with hCG- and LH-modified sensors suggest a higher protein discrimination capacity for MIP-PQ, which can possibly be attributed to either an unfavorable protein immobilization masking the SV epitope or an intrinsically lower affinity of MIP-SV for the epitope.

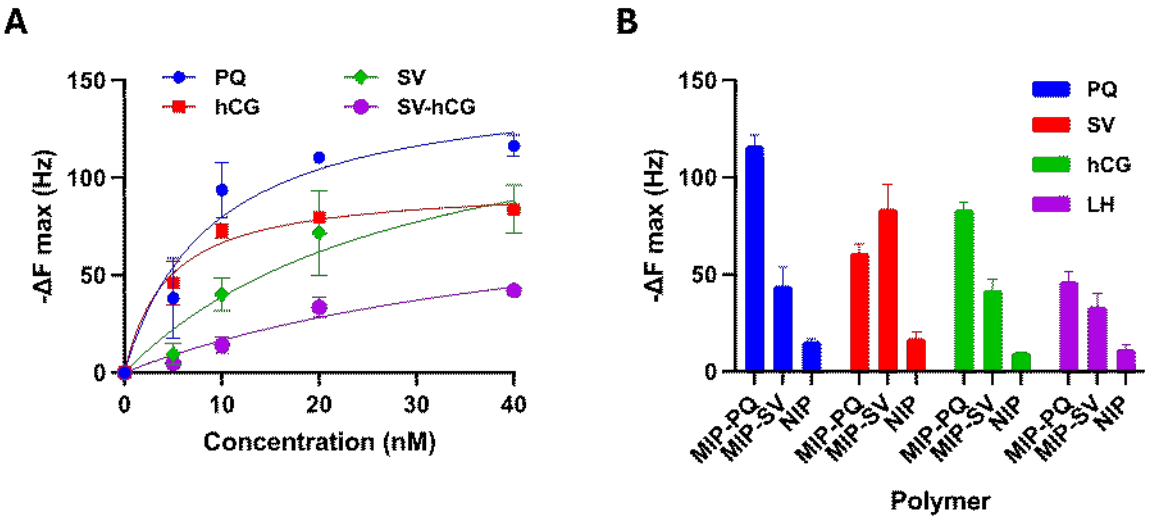

Fig. 6. (A) Apparent non-equilibrium binding isotherms of MIP-PQ on a PQ (blue curve) and hCG (red curve) functionalized sensor chip and MIP-SV on a SV (green curve) and hCG (purple curve) functionalized sensor chip. The data were fitted to a 1:1 Langmuir adsorption model to determine the apparent dissociation constants given in Table 3. (B) Maximum frequency changes registered for the different sensor chips at a nanogel concentration of 40 nM.

The potential binding of MIPs to other proteins through non-specific surface sites was further addressed by complementary experiments in which we evaluated the binding response of nanogel dispersions of increasing concentration (0.02-0.1 $mg \cdot mL^{-1}$) to three immobilized proteins on the surface of microplate wells (hCG, 36 kDa; fetuin, 48.4 kDa; and BSA. 66.5 kDa) (Supporting

Information). The immobilized proteins were incubated with nanogel dispersions of increasing concentration, and the amount of bound MIP was quantified from fluorescence intensity measurements after washing out the unbound fraction. Selective but not specific responses were attained at all concentrations, with higher fluorescence intensities measured in the hCG-containing wells over fetuin and BSA (Fig. S6). These findings highlight the need for further improvements to reduce the heterogeneity of the imprinted cavities on the nanogel surface to maximize the selectivity toward the desired protein template.

MIP	Epitope			hCG		
	K_D (nM)	ΔFmax	R^2	K_D (nM)	ΔFmax	R^2
MIP-PQ	8.9±4.3	151±25	0.95	4.4±1.2	96±6.0	0.99
MIP-SV	30±19	154±53	0.95	49±35	98±45	0.96

Table 3. Calculated equilibrium dissociation constant (KD) of the nanogels from data presented in Fig. 6A. All experiments were performed under ambient conditions and with three replicates.

MIP-based microplate assays for hCG detection

The capacity of the imprinted nanogels to serve as synthetic antibodies for hCG recognition was evaluated from MIP-based ELISA sandwich assays. [46] To this aim, we used the experimental setting of a commercial ELISA kit for hCG detection replacing the natural antibody with MIPs-SV and MIPs-PQ as primary protein receptors. The nanogels were immobilized on the surface of polystyrene microplate wells by physical adsorption followed by treatment with blocking solution, optimized according to Table S3 and Fig. S7, followed by incubation with solutions of increasing hCG concentration (0-200 $mIU \cdot mL^{-1}$). Each sample was supplemented with a fixed concentration of the LH protein (100 $mIU \cdot mL^{-1}$) as an analogous analyte that can compete with hCG for the MIPs' binding sites. Parallel experiments were conducted in microplates containing the natural capture antibody provided by the commercial supplier under identical incubation conditions (Fig. 7). MIP-based assays resulted in non-linear concentration-dependent absorbance responses, with an apparent saturation of binding sites at hCG concentrations higher than 100 $mIU \cdot mL^{-1}$. The analytical signals

showed large variability between replicate experiments, which suggests issues with MIPs immobilization or the non-specific binding of the detection antibodies throughout the experimental procedure. The antibody-based experiments also lead to large variabilities, indicating similar limitations to MIP-based assays under identical conditions. These findings highlight the need for optimizing nanomaterial and antibody immobilization on microplates to enhance analytical performance and reduce inter-replicate variability. Despite these opportunities for improvement, MIP-based assays exhibit analytical responses dependent on the concentration of hCG in the presence of a highly structurally similar interferant, demonstrating the selectivity of the nanomaterials for the analyte for which they were synthesized, with similar outcomes to natural antibodies. Our findings also support the feasibility of replacing natural antibodies with synthetic antigen-imprinted nanogels, offering equivalent analytical performance, with significantly lower production costs and higher stability for laboratory handling and storage.

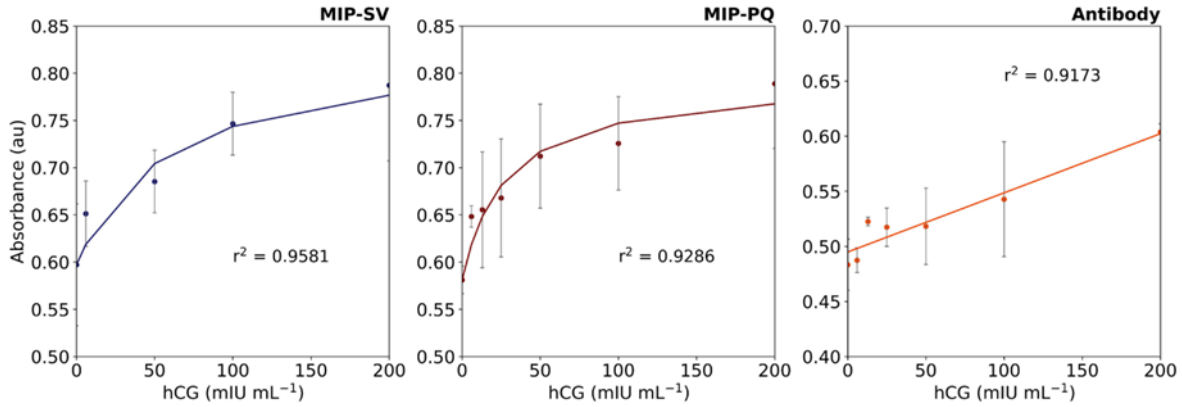

Fig. 7. Microplate assays for hCG detection using MIP-SV, MIP-PQ or a commercial antibody as primary protein receptor. Experiments were conducted with hCG solutions of increasing concentration (0-200 mIU·mL-1) in the presence of a constant concentration of the luteinizing hormone LH (100 mIU·mL-1) as an analogous analyte that can compete with hCG for recognition sites.

CONCLUSIONS

A solid-phase epitope-based synthetic approach was applied to obtain water-soluble molecularly imprinted nanoparticles for hCG detection. MD simulations were used to investigate the structure of the immobilized peptide templates within the context of prepolymerization mixtures. Our findings confirmed that the chosen peptides have conformational properties that mimic the dynamic behavior of the epitopes in the full protein, thereby supporting their potential to imprint molecular cavities suitable for hCG recognition. Template-monomer interactions were found to be driven by TBAm and NIPAm, with a minor contribution of BIS and negligible interactions with AA and APM monomers. These findings offer an opportunity for optimizing the pre-polymerization mixture by varying the monomer types or proportions to maximize the interactions with the template.

The synthesized MIPs have homogeneous size distributions and exhibit high binding affinity and specificity toward the SV and PQ epitopes and hCG as shown through SPR and QCM analysis. The selectivity towards hCG over other proteins and potential intererants including LH was confirmed. A MIP-based ELISA was implemented by replacing the natural capture antibody of a commercial kit with the synthesized nanogels MIP-SV and MIP-PQ. MIPbased assays showed a linear analytical response to increasing hCG levels, with similar outomes to the commercial kit. The nanogels preserved their response to hCG in the presence of the interferent protein LH, which supports the specificity of the developed materials toward the target protein. All in all, the study suggests the feasibility of using imprinted nanogels as a class of cost-effective, stable alternatives to natural antibodies for hCG detection. We foresee applications of these binders with respect to reusable pregnancy tests and other hCG-related disease diagnostics.

Acknowledgment

We acknowledge financial support from EU through the WomenTechEU program (Pharmista) and stipends from the Sten K. Johnsson Foundation (Surecapture Technologies, Pharmista).

Yadiris García thanks to Postdoctoral Project ANID/FONDECYT 3200508 for the financial support. Verónica Jiménez thanks Agencia Nacional de Investigación y Desarrollo through Grant EXPLORACION 13220020 for finantial support.

Francesco Patitucci was funded by PON “Ricerca e Innovazione” 2014–2020, Asse IV “Istruzione e ricerca per il recupero”, Azione IV.4—“Dottorati e contratti di ricerca su tematiche dell’innovazione”.

REFERENCES

[1] L.A. Cole, New discoveries on the biology and detection of human chorionic gonadotropin, Reproductive Biology and Endocrinology : RB&E 7 (2009) 8-8.

[2] L.A. Cole, Biological functions of hCG and hCG-related molecules, Reproductive Biology and Endocrinology 2010 8:1 8(1) (2010) 1-14.

[3] C. Gnoth, S. Johnson, Strips of hope: Accuracy of home pregnancy tests and new developments, Geburtshilfe und Frauenheilkunde 74(7) (2014) 661-669.

[4] C.E. Kennedy, P.T. Yeh, K. Gholbzouri, M. Narasimhan, Self-testing for pregnancy: a systematic review and meta-analysis, BMJ Open 12(2) (2022) e054120-e054120.

[5] U.-H. Stenman, H. Alfthan, K. Hotakainen, Human chorionic gonadotropin in cancer, Clinical biochemistry 37(7) (2004) 549-561.

[6] L. Sisinni, M. Landriscina, The Role of Human Chorionic Gonadotropin as Tumor Marker: Biochemical and Clinical Aspects, Adv Exp Med Biol2015, pp. 159-176.

[7] U.H. Stenman, A. Tiitinen, H. Alfthan, L. Valmu, The classification, functions and clinical use of different isoforms of HCG, Human Reproduction Update, 2006, pp. 769- 784.

[8] P. Berger, E. Paus, P.M. Hemken, C. Sturgeon, W.W. Stewart, J.P. Skinner, L.C. Harwick, S.C. Saldana, C.S. Ramsay, K.R. Rupprecht, K.H. Olsen, J.M. Bidart, U.H. Stenman, Candidate epitopes for measurement of hCG and related molecules: The second ISOBM TD-7 workshop, Tumor Biology 34(6) (2013) 4033-4057.

[9] H.R. Boehringer, B.J. O'Farrell, Lateral Flow Assays in Infectious Disease Diagnosis, Clinical Chemistry 68(1) (2021) 52-58.

[10] G.E. Fridley, H.Q. Le, E. Fu, P. Yager, Controlled release of dry reagents in porous media for tunable temporal and spatial distribution upon rehydration, Lab on a chip 12(21) (2012) 4321-4321.

[11] M.A. Dineva, D. Candotti, F. Fletcher-Brown, J.P. Allain, H. Lee, Simultaneous visual detection of multiple viral amplicons by dipstick assay, Journal of Clinical Microbiology 43(8) (2005) 4015-4021.

[12] Y. Hoshino, H. Koide, T. Urakami, H. Kanazawa, T. Kodama, N. Oku, K.J. Shea, Recognition, Neutralization, and Clearance of Target Peptides in the Bloodstream of Living Mice by Molecularly Imprinted Polymer Nanoparticles: A Plastic Antibody, Journal of the American Chemical Society 132(19) (2010) 6644-6645.

[13] S. Shinde, Z. El-Schich, A. Malakpour, W. Wan, N. Dizeyi, R. Mohammadi, K. Rurack, A. Gjorloff Wingren, B. Sellergren, Sialic Acid-Imprinted Fluorescent Core-Shell Particles for Selective Labeling of Cell Surface Glycans, J Am Chem Soc 137(43) (2015) 13908-12.

[14] B. Tse Sum Bui, A. Mier, K. Haupt, Molecularly Imprinted Polymers as Synthetic Antibodies for Protein Recognition: The Next Generation, Small, John Wiley and Sons Inc, 2023.

[15] H. Zhang, Molecularly Imprinted Nanoparticles for Biomedical Applications, Advanced Materials 32(3) (2020) 1806328.

[16] R. Koeber, C. Fleischer, F. Lanza, K.S. Boos, B. Sellergren, D. Barcelo, Evaluation of a multidimensional solid-phase extraction platform for highly selective on-line cleanup and high-throughput LC-MS analysis of triazines in river water samples using molecularly imprinted polymers, Anal Chem 73(11) (2001) 2437-44.

[17] C. Blackburn, M.V. Sullivan, M.I. Wild, A.J. O' Connor, N.W. Turner, Utilisation of molecularly imprinting technology for the detection of glucocorticoids for a point of care surface plasmon resonance (SPR) device, Analytica Chimica Acta 1285 (2024) 342004.

[18] Q. Li, S. Shinde, G. Grasso, A. Caroli, R. Abouhany, M. Lanzillotta, G. Pan, W. Wan, K. Rurack, B. Sellergren, Selective detection of phospholipids using molecularly imprinted fluorescent sensory core-shell particles, Sci Rep 10(1) (2020) 9924.

[19] M.R. Halhalli, E. Schillinger, C.S.A. Aureliano, B. Sellergren, Thin Walled Imprinted Polymer Beads Featuring Both Uniform and Accessible Binding Sites, Chemistry of Materials 24(15) (2012) 2909-2919.

[20] Y. Hoshino, T. Kodama, Y. Okahata, K.J. Shea, Peptide Imprinted Polymer Nanoparticles: A Plastic Antibody, J. Am. Chem. Soc. FIELD Full Journal Title:Journal of the American Chemical Society 130(46) (2008) 15242-15243.

[21] Z. Zeng, Y. Hoshino, A. Rodriguez, H. Yoo, K.J. Shea, Synthetic Polymer Nanoparticles with Antibody-like Affinity for a Hydrophilic Peptide, ACS Nano 4(1) (2010) 199-204.

[22] Mier, I. Maffucci, F. Merlier, E. Prost, V. Montagna, G.U. Ruiz-Esparza, J.V. Bonventre, P.K. Dhal, B. Tse Sum Bui, P. Sakhaii, K. Haupt, Molecularly Imprinted Polymer Nanogels for Protein Recognition: Direct Proof of Specific Binding Sites by Solution STD and WaterLOGSY NMR Spectroscopies, Angewandte Chemie International Edition 60(38) (2021) 20849-20857.

[23] Rachkov, N. Minoura, Recognition of oxytocin and oxytocin-related peptides in aqueous using a molecularly imprinted polymer the epitope approach, J. Chromatogr., A 889(1+2) (2000) 111-118.

[24] M.M. Titirici, A.J. Hall, B. Sellergren, Hierarchical Imprinting Using Crude Solid Phase Peptide Synthesis Products as Templates, Chemistry of Materials 15(4) (2003) 822- 824.

[25] H. Nishino, C.-S. Huang, K.J. Shea, Selective protein capture by epitope imprinting, Angewandte Chemie, International Edition 45(15) (2006) 2392-2396.

[26] L. Pasquardini, A.M. Bossi, Molecularly imprinted polymers by epitope imprinting: a journey from molecular interactions to the available bioinformatics resources to scout for epitope templates, Analytical and Bioanalytical Chemistry 413(24) (2021) 6101-6115.

[27] Poma, A. Guerreiro, M.J. Whitcombe, E.V. Piletska, A.P.F. Turner, S.A. Piletsky, Solid-Phase Synthesis of Molecularly Imprinted Polymer Nanoparticles with a Reusable Template–"Plastic Antibodies", Advanced Functional Materials 23(22) (2013) 2821-2827.

[28] S. Ambrosini, S. Beyazit, K. Haupt, B. Tse Sum Bui, Solid-phase synthesis of molecularly imprinted nanoparticles for protein recognition, Chemical Communications 49(60) (2013) 6746-6748.

[29] M. Berghaus, R. Mohammadi, B. Sellergren, Productive encounter: molecularly imprinted nanoparticles prepared using magnetic templates, Chemical Communications 50(64) (2014) 8993-8996.

[30] R. Mahajan, M. Rouhi, S. Shinde, T. Bedwell, A. Incel, L. Mavliutova, S. Piletsky, I.A. Nicholls, B. Sellergren, Highly Efficient Synthesis and Assay of Protein-Imprinted Nanogels by Using Magnetic Templates, Angew Chem Int Ed Engl 58(3) (2019) 727-730.

[31] T. Hix-Janssens, J.R. Davies, N.W. Turner, B. Sellergren, M.V. Sullivan, Molecularly imprinted nanogels as synthetic recognition materials for the ultrasensitive detection of periodontal disease biomarkers, Analytical and Bioanalytical Chemistry (2024).

[32] S. Dirnhofer, S. Madersbacher, J.M. Bidart, P.B.W. Ten Kortenaar, G. Spottl, K. Mann, G. Wick, P. Berger, The molecular basis for epitopes on the free β-subunit of human chorionic gonadotrophin (hCG), its carboxyl-terminal peptide and the hCGβ-core fragment, Journal of Endocrinology 141(1) (1994) 153-162.

[33] T. Klonisch, P.J. Delves, P. Berger, G. Panayotou, A.J. Lapthorn, N.W. Isaacs, G. Wick, T. Lund, I.M. Roitt, Relative location of epitopes involved in synergistic antibody binding using human chorionic gonadotropin as a model, European Journal of Immunology 26(8) (1996) 1897-1905.

[34] L. Valmu, H. Alfthan, K. Hotakainen, S. Birken, U.H. Stenman, Site-specific glycan analysis of human chorionic gonadotropin β-subunit from malignancies and pregnancy by liquid chromatography - Electrospray mass spectrometry, Glycobiology 16(12) (2006) 1207-1218.

[35] H. Lund, E. Paus, P. Berger, U.H. Stenman, T. Torcellini, T.G. Halvorsen, L. Reubsaet, Epitope analysis and detection of human chorionic gonadotropin (hCG) variants by monoclonal antibodies and mass spectrometry, Tumor Biology 35(2) (2014) 1013-1022.

[36] F. Canfarotta, A. Poma, A. Guerreiro, S. Piletsky, Solid-phase synthesis of molecularly imprinted nanoparticles, Nature Protocols 11 (2016) 443.

[37] [R. Mahajan, S. Suriyanarayanan, I.A. Nicholls, Improved Solvothermal Synthesis of γ- Fe_2O_3 Magnetic Nanoparticles for SiO_2 Coating, Nanomaterials (Basel, Switzerland) 11(8) (2021) 1889.

[38] S. Udenfriend, S. Stein, P. Boehlen, W. Dairman, W. Leimgruber, M. Weigele, Fluorescamine: a reagent for assay of amino acids, peptides, proteins, and primary amines in the picomole range, Science 178(4063) (1972) 871-872.

[39] J.V. Castell, M. Cervera, R. Marco, A convenient micromethod for the assay of primary amines and proteins with fluorescamine. A reexamination of the conditions of reaction, Analytical biochemistry 99(2) (1979) 379-391.

[40] A.J. Lapthorn, D.C. Harris, A. Littlejohn, J.W. Lustbader, R.E. Canfield, K.J. Machin, F.J. Morgan, N.W. Isaacs, Crystal structure of human chorionic gonadotropin, Nature 369(6480) (1994) 455-461.

[41] L. Martínez, R. Andrade, E.G. Birgin, J.M. Martínez, PACKMOL: A package for building initial configurations for molecular dynamics simulations, J. Comput. Chem. 30 (2009) 2157-2164.

[42] D.R. Roe, T.E. Cheatham Iii, PTRAJ and CPPTRAJ: Software for Processing and Analysis of Molecular Dynamics Trajectory Data, Journal of Chemical Theory and Computation 9(7) (2013) 3084-3095.

[43] W. Humphrey, A. Dalke, K. Schulten, VMD: visual molecular dynamics, J Mol Graph 14(1) (1996) 27-38.

[44] T.S. Bedwell, N. Anjum, Y. Ma, J. Czulak, A. Poma, E. Piletska, M.J. Whitcombe, S.A. Piletsky, New protocol for optimisation of polymer composition for imprinting of peptides and proteins, RSC Advances 9(48) (2019) 27849-27855.

[45] H. Koide, K. Yoshimatsu, Y. Hoshino, S.H. Lee, A. Okajima, S. Ariizumi, Y. Narita, Y. Yonamine, A.C. Weisman, Y. Nishimura, N. Oku, Y. Miura, K.J. Shea, A polymer nanoparticle with engineered affinity for a vascular endothelial growth factor (VEGF(165)), Nat Chem 9(7) (2017) 715-722.

[46] I. Chianella, A. Guerreiro, E. Moczko, J.S. Caygill, E.V. Piletska, I.M.P. De Vargas Sansalvador, M.J. Whitcombe, S.A. Piletsky, Direct Replacement of Antibodies with Molecularly Imprinted Polymer Nanoparticles in ELISA—Development of a Novel Assay for Vancomycin, Analytical Chemistry 85(17) (2013) 8462-8468.

Supporting Information

Development and Benchmarking of Molecularly Imprinted Polymer for Human Chorionic Gonadotropin (hCG) Detection

Radvile Zubryté, Liliia Mavliutova, Yadiris García, Mark V. Sullivan, Nicholas W. Turner, Francesco Patitucci, Laura C. Polania, Verónica A. Jiménez, Robert Porter, Alice Mattsson* and Börje Sellergren*

Supporting Tables

Sequence	Sequence length	Hydrophobicity	GRAVY	Mw average (g/mol)	Theoretical pI
SIRLPGCPRGVNPVV	15	28	0.30	1564	10.9
PGPSDTPILPQ	11	23	-0.64	1121	3.1

Table S1. Epitope properties

Entry	NIPAm	BIS	TBAm	APM	AAc	FITC-AAm
MIP-SV	45	5	40	5	5	0.8 mg
MIP-PQ	48	2	40	10	0	0.4 mg

Table S2. Functional monomer feed ratio (mole %) used for MIP synthesis.

Blocking solution	Composition
BS-1	Ethanolamine 10 %, MilliQ H_2O
BS-2	Ethanolamine 5 %, MilliQ H_2O
BS-3	0.3 % BSA, 1.0 % Tween 20, PBS pH 7.2
BS-4	0.5 % BSA, 1.0 % Tween 20, PBS pH 7.2
BS-5	0.7 % BSA, 1.0 % Tween 20, PBS pH 7.2
BS-6	1.0 % BSA, 1.0 % Tween 20, PBS pH 7.2
BS-7	EveryBlot blocking buffer (BIO-RAD)

Table S3. List of blocking solutions tested to minimize the non-specific analytical response in a microplate antibody-based assay for hCG detection.

Supporting Figures

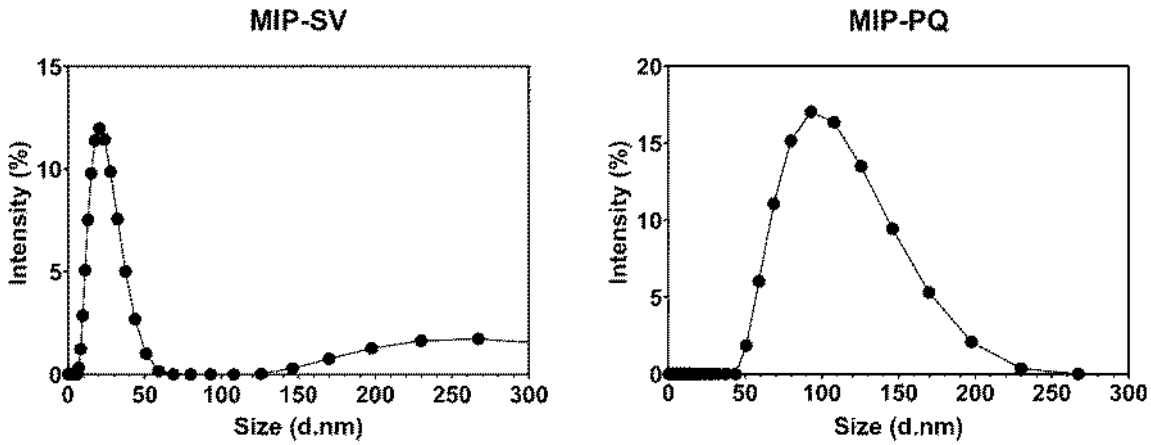

Fig. S1 – DLS size distribution of MIP-SV and MIP-PQ

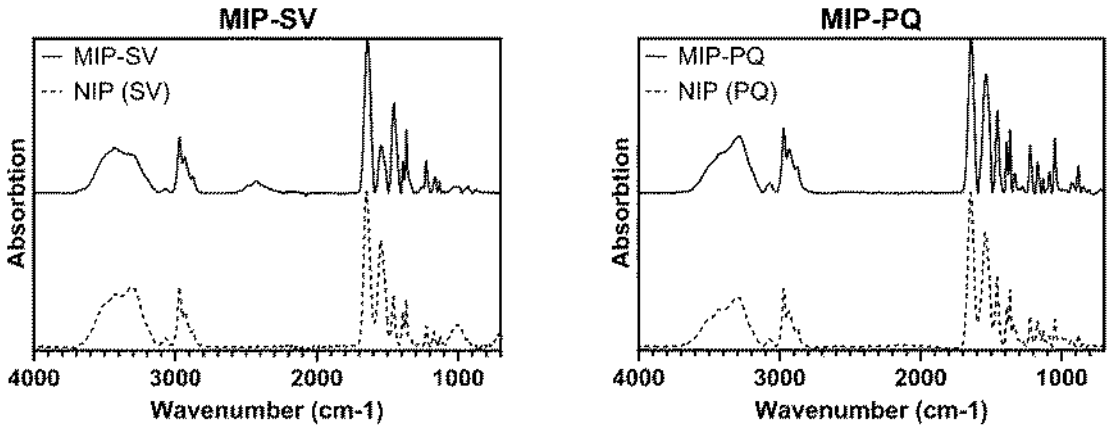

Fig. S2. Fourier transform infrared (FTIR) spectroscopy of MIP-SV and MIP-PQ and corresponding NIPs.

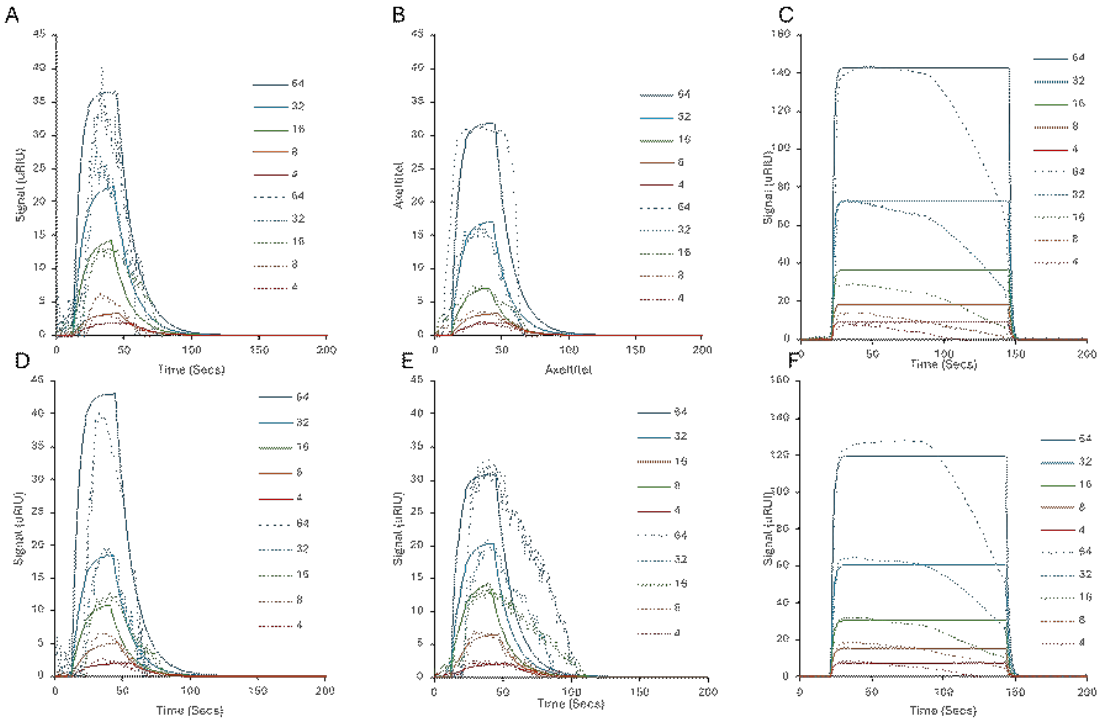

Fig. S3. Representative fitted SPR curves showing the rebinding of the target and non-target peptides to the immobilized nanogel with five concentrations of the analyte in PBST. (A-C) SV, PQ and hCG binding to MIP-SV; (D-F) PQ, SV and hCG binding to MIP-PQ.

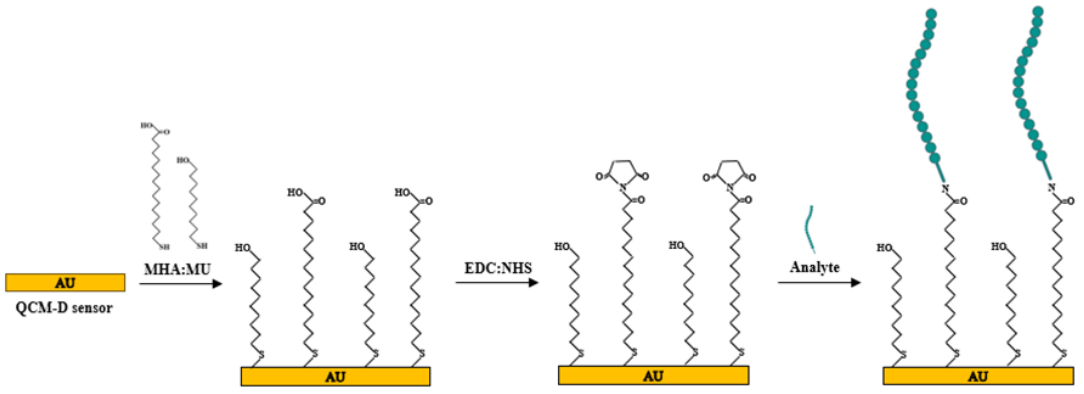

Fig. S4. The process of QCM sensor chip modification with the target peptide.

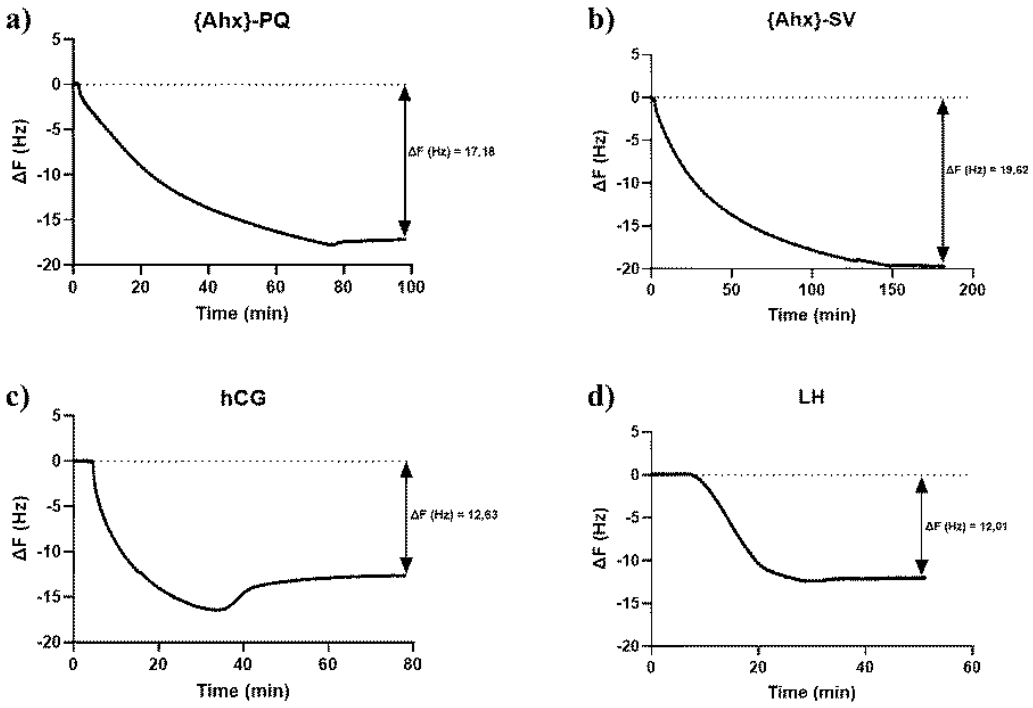

Fig. S5. Analyses of QCM-D sensor modification with a) Ahx-PQ, b) Ahx-SV, c) hCG and d) LH.

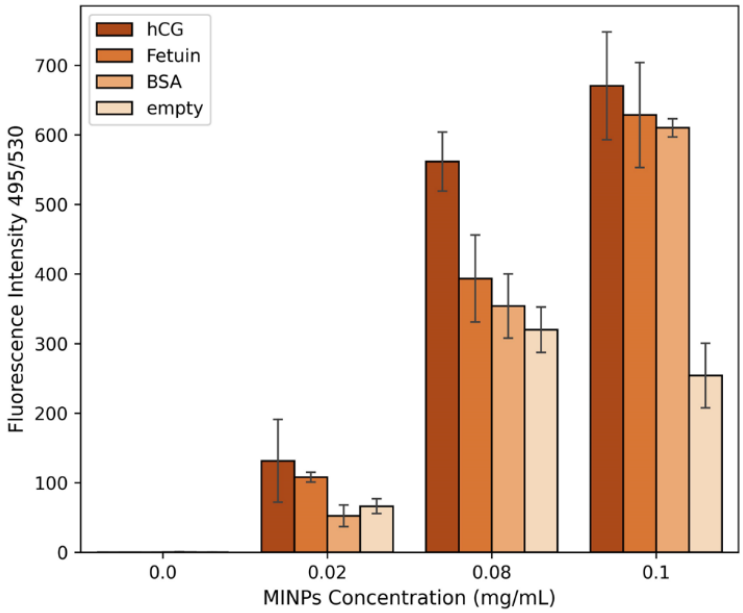

Fig. S6. Microplate-based test of protein discrimination showing the preferential association of MIP-SV dispersions (0-0.1 mg/mL) to immobilized hCG over fetuin and BSA. Empty wells were used as controls at each concentration to account for the extent of nanogel binding on the microplate surface. Fluorescence intensity was measured at 495 nm (excitation) and 530 nm (emission). Experiments were conducted in duplicate.

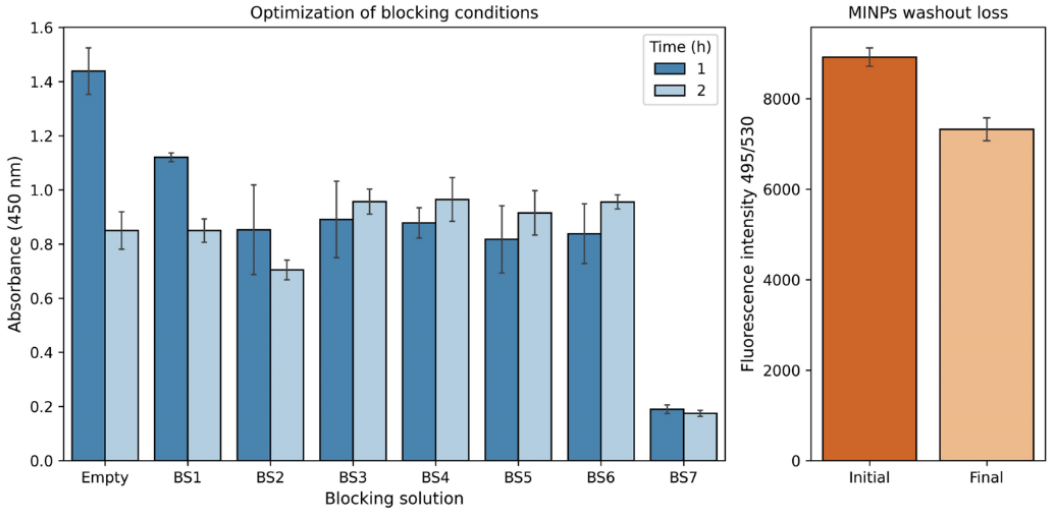

Fig. S7. (left) Analytical response of empty microplate wells treated with seven blocking solutions (Table S3) to the non-specific bindings of the Alpha hCG and the anti-mouse immunoglobulins/HRP antibodies used for hCG detection. Absorbance was measured at 450 nm after the HPR-driven chromogenic reaction. (right) Fluorescence intensity at 495 nm (excitation) and 530 nm (emission) was measured in MIPs-treated microplate wells at the beginning of the experimental procedure (Initial) and after the series of washing steps considered in the protocol for hCG detection. A total nanogel loss close to 20% was estimated from fluorescence intensity measurements.

II

Molecularly Imprinted Polymers (MIPs) for SARS-CoV-2 Omicron variant inhibition: an alternative approach to address the challenge of emerging zoonoses

Marco Dattilo [a, ‡], Francesco Patitucci [a, ‡], Marisa Francesca Motta [a], Sabrina Prete [a], Roberta Galeazzi [b], Silvia Franzè [c], Ida Perrotta [d], Mariangela Caravelli [e], Ortensia Ilaria Parisi [a,f,*], Francesco Puoci [a,f]

[a] Department of Pharmacy, Health and Nutritional Sciences, University of Calabria, 87036 Rende (CS), Italy

[b] Department of Life and Environmental Sciences, Marche Polytechnic University, 60131 Ancona, Italy

[c] Department of Pharmaceutical Sciences, University of Milan, 20133 Milan, Italy

[d] Department of Biology, Ecology and Earth Sciences, University of Calabria, 87036 Rende, CS, Italy

[e] Université Paris-Saclay, Inserm, CEA, Center for Immunology of Viral, Auto-immune, Hematological and Bacterial diseases (IMVA-HB/IDMIT), Fontenay-aux-Roses & Le Kremlin-Bicêtre, France

[f] Macrofarm s.r.l., c/o Department of Pharmacy, Health and Nutritional Sciences, University of Calabria, 87036 Rende (CS), Italy

‡ *These authors contributed equally.*

ABSTRACT

Emerging zoonoses pose significant public health risks and necessitate rapid and effective treatment responses. This study enhances the technology for preparing Molecularly Imprinted Polymers (MIPs), which function as synthetic antibodies targeting SARS-CoV-2 receptor-binding domain

(RBD), specifically the Omicron variant, thereby inhibiting its function. This study builds on previous findings by introducing precise adjustments in the formulation and process conditions to enhance particle stability and ensure better control over size and distribution, thereby overcoming the issues identified in earlier research. Following docking studies, imprinted nanoparticles were synthesized via inverse microemulsion polymerization and characterized in terms of size, morphology and surface charge. The selective recognition properties and ability of MIPs to obstruct the interaction between ACE2 and the RBD of SARS-CoV-2 were assessed in vitro, using Non-Imprinted Polymers (NIPs) as controls, and rebinding studies were conducted utilizing a Quartz Crystal Microbalance with Dissipation monitoring (QCM-D). The synthesized nanoparticles exhibited uniform dispersion and had a consistent diameter within the nanoscale range. MIPs demonstrated significant recognition properties and exhibited a concentration-dependent ability to reduce RBD binding to ACE2 without cytotoxic or sensitizing effects. MIPs-based antibodies offer a promising alternative to natural antibodies for treating SARS-CoV-2 infections, therefore representing a versatile platform for managing emerging zoonoses.

INTRODUCTION

The COVID-19 pandemic, caused by the Severe Acute Respiratory Syndrome Coronavirus 2 (SARS-CoV-2), has posed an unprecedented challenge to global public health systems. Emerging in late 2019, the virus rapidly spread worldwide, leading to widespread morbidity and mortality. As of recent records, millions of confirmed cases and deaths have been reported globally, reflecting the virus's severe impact [30]. This worldwide outbreak demonstrated how swiftly emerging infectious diseases can severely impact human health and national economies and underscored the critical need for effective therapeutics, vaccines, and diagnostic tools to combat its transmission and mitigate its impact on public health [18].

A critical component in developing effective targeted interventions is comprehending the structural composition of SARS-CoV-2. The virus's structure comprises several key proteins, including the spike (S) protein, which plays a pivotal role in the virus's ability to infect host cells. The S protein facilitates the virus's entry into host cells by binding to the angiotensin-converting enzyme 2 (ACE2) receptor, a process primarily mediated by the receptor-binding domain (RBD) of the S protein [11]. This interaction is a critical step in the viral infection cycle, making the RBD a prime target for therapeutic interventions.

Vaccines have been instrumental in reducing the severity and spread of the disease, with various types developed, including mRNA, viral vector, and protein subunit vaccines [25]. Monoclonal antibodies have been used as both therapeutic and preventive measures, providing passive immunity by targeting specific viral epitopes [14]. However, the emergence of new variants of concern (VOCs), such as the Delta and Omicron variants, has complicated these efforts due to mutations in the S protein that can alter antibody binding and reduce vaccine efficacy [28].

In particular, during the peak of the pandemic, global concerns surged as the Omicron variant emerged as the most genetically diverse form of SARS-CoV-2 yet known. The B.1.1.529 variant, first detected in Botswana and South Africa, was named as the Omicron variant on November 26, 2021 [29]. Its remarkable ability to spread rapidly and evade immune defenses heightened anxieties worldwide, underscoring the urgent need for a multifaceted approach to interventions, including the development of novel therapeutics [13].

In this context, Molecularly Imprinted Technology (MIT) represents an innovative method that has garnered attention for its role in developing synthetic receptors. Molecularly Imprinted Polymers (MIPs) are synthetic polymers that can be engineered to have specific binding sites, tailored to the shape and chemical properties of target molecules, akin to the binding sites of natural antibodies. This technology offers several advantages, including high stability, ease of production, and the potential for cost-effective mass production. MIPs can mimic natural antibodies' high specificity and affinity, making them promising candidates for various applications, including diagnostics, therapeutic delivery, and environmental monitoring [7,22]. In diagnostics, MIPs can be employed to detect a wide range of analytes, including pathogens, toxins, and biomarkers, with high sensitivity and specificity. This capability is particularly valuable in the context of infectious diseases, where rapid and accurate detection can significantly impact patient outcomes and public health responses [2]. For therapeutic applications, MIPs can be utilized in targeted drug delivery systems, where they can selectively bind to specific sites in the body, releasing therapeutic agents in a controlled manner. This targeted approach can enhance the efficacy of treatments and minimize side effects, offering a significant advantage over conventional therapies [4]. Moreover, MIPs hold potential for the development of next-generation pharmacological agents capable of disrupting protein-protein interactions. In a recent study, Herrera Le´on et al. investigated the application of MIPs as synthetic peptide antibodies targeting Tumor Necrosis Factor-alpha (TNF-α), a cytokine implicated in autoimmune and inflammatory disorders. The proposed inhibition mechanism relies on a highly

specific binding process that neutralizes TNF-α's inflammatory effects by blocking its interaction with its cell surface receptors, TNFR1 and TNFR2 [10]. Zhou et al., on the other hand, introduced a potential new application for MIPs in antiviral therapy by using them to inhibit viral infections [31]. Specifically, glycan-imprinted nanoparticles were designed to target the HIV-1 envelope protein. By binding specifically to the glycans on the viral envelope, MIPs were able to prevent HIV-1 from infecting target CD4+cells. The nanoparticles showed strong binding affinity and high specificity, with broad inhibitory activity against multiple HIV-1 strains. The versatility and adaptability of MIT allow MIPs to be tailored for a broad range of applications, making them a valuable tool in both medical and environmental fields.

Building on this premises, we aimed to apply MIT as a strategy for inhibiting SARS-CoV-2 infection. Several studies have already explored the applicability of MIT for the detection of SARS-CoV-2. For instance, Bajaj et al. investigated the potential of MIPs for detecting the entire SARS-CoV-2 virus using a label-free, miniaturized Surface Plasmon Resonance (SPR) sensor. Their study demonstrated the successful stepwise fabrication of the sensor, indicating its potential role in monitoring and managing viral contamination and infection risks [1]. Raziq et al. focused their attention on the SARS-CoV-2 Nucleocapsid Protein (ncovNP), a key antigen for COVID-19 diagnostics. They developed a portable electrochemical sensor incorporating a poly-m-phenylenediamine-based MIP as a selective recognition element. Validation with clinical nasopharyngeal swab samples demonstrated the sensor's ability to accurately detect ncovNP in complex biological media, showing promising potential for diagnostic applications [24]. Our group recently reported on the development of MIPs capable of selectively recognizing and binding the S protein RBD of SARS-CoV-2, effectively blocking its function and potentially inhibiting viral infection [21]. The MIPs were synthesized via inverse microemulsion polymerization using a non-covalent imprinting approach with acrylamide and methacrylic acid as monomers. In vitro studies confirmed the antiviral activity and specificity of the MIPs. However, challenges such as particle

aggregation at high concentrations, reduced stability, and difficulties in controlling particle size and achieving monodispersity were encountered.

Here, we developed a refined synthesis protocol by introducing precise adjustments in the formulation and process conditions, enhancing particle stability, and enabling better control over size and distribution. Additionally, to demonstrate the versatility of the technique, we decided to use the Omicron variant of SARS-CoV-2 as template molecule to reflect ongoing efforts to adapt interventions to emerging viral strains. Various experimental methods, including Dynamic Light Scattering (DLS) for measuring size [12]and gravitational sedimentation with the Turbiscan optical analyzer [16], have been employed to study nanoparticle dispersions. The results showed that MIPs had significantly higher binding efficacy to the RBD compared to non-imprinted polymers (NIPs), due to their specific imprinted cavities. Neutralizing anti-SARS-CoV-2 antibody assay and QCM-D analysis confirmed the superior specificity and binding capability of MIPs, highlighting their potential for precise molecular recognition, outperforming both NIPs and non-target proteins such as Human Serum Albumin (HSA). This technique offers a versatile and effective approach to addressing the evolving challenges posed by SARS-CoV-2 and its variants. By refining synthesis techniques and targeting specific viral components like the RBD, it’s possible to enhance the specificity and efficacy of these synthetic particles, potentially leading to new prophylactic and therapeutic options for COVID-19 and other infectious diseases.

EXPERIMENTAL SECTION

Reagents

The receptor-binding domain of the SARS-CoV-2 B.1.1.529 sublineage BA.2 (Omicron) spike protein (RBD, His Tag) was purchased from Sino Biological Inc. (Beijing, China). Acrylamide (AAm), Acrylic acid (AAc), N,N′-methylenebisacrylamide, N-Isopropylacrylamide (NIPAM), n-Propyl Methacrylate (nPMA), N-tert-Butylacrylamide (TBAm), tween-80, span-80, dioctyl sulfosuccinate sodium salt (AOT), ammonium persulfate (APS), N,N,N,N-tetramethylethylenediamine (TEMED), disodium hydrogen phosphate, sodium dihydrogen phosphate, human serum albumin (HSA), 3-sulfo-N-Hydroxysuccinimide (Sulfo-NHS), 1-ethyl-3-(3-dimethylaminopropyl)carbodiimide (EDC), 16-Mercaptohexadecanoic acid (MHA), 11-Mercapto-1-undecanol (MU), Dulbecco's Modified Eagle Medium (DMEM, Product No. D0822), Penicillin/Streptomycin (Product No. P0781), β-Mercapto- ethanol (Product No. M3148), Fetal Bovine Serum (FBS, Product No. F4135), Bovine Calf Serum (BCS, Product No. 12133 C), 3-(4,5-dimethylthiazol-2-yl)-2,5-diphenyltetrazolium (MTT, Product No. 475989), nickel sulfate (Product No. 1.06726), propidium iodide (Product No. 537059), FACS buffer (PBS, 0.5–1 % BSA or 5–10 % FBS, 0.1 % sodium azide), sodium azide (Product No. 71289), Bovine Serum Albumin (BSA, Product No. A4503), and γ-globulin (Product No. G5009) were purchased from Sigma-Aldrich s.r.l. (Milan, Italy). RPMI 1640 medium was obtained from ATCC (Manassas, VA, USA). The Anti-SARS-CoV-2 (BA.2) Neutralizing Antibody Titer Serologic Assay Kit (Catalog number RAS-N087) was obtained from Acro Biosystems (Newark, DE, USA). All solvents were of reagent or HPLC grade and obtained from VWR (Milan, Italy). 5 MHz Au-coated QCM sensors were obtained from Novaetech S.r. l. (Italy).

Cell cultures

BALB/3T3 cells were purchased from the American Type Culture Collection (ATCC, Manassas, VA, USA) and maintained in DMEM medium (containing 2 mM L-glutamine, 1 % penicillin-streptomycin, and 1 % sodium pyruvate 1 mM) supplemented with 10 % bovine calf serum (BCS) at 37◦C in a humidified atmosphere consisting of 5 % CO2 in air. THP-1 cells were purchased from the American Type Culture Collection (ATCC, Manassas, VA, USA) and cultured in RPMI 1640 medium supplemented with 10 % FBS, 1 % Penicillin/Streptomycin, and 0.05 mM β-Mercapto-ethanol at 37◦C in a humidified atmosphere consisting of 5 % CO2 in air.

Instrumentation

Transmission electron micrographs were captured with a Jeol Transmission Electron Microscope, model JEM-1409Plus, operating at 80 kV. The particle size distribution was determined through dynamic light scattering (DLS) utilizing a Zetasizer (Nano-ZS, Malvern Instrument, UK) and Nanoparticle Trafficking Analysis employing a Nanosight NS 300 (Malvern Instrument, UK). For DLS, samples diluted (1:10) in ultrapure water were measured in a disposable cuvette at a detection angle of 173◦. ζ-Potential was evaluated on samples placed in a capillary cell. Three measurements were conducted for each sample, and the outcomes are presented as mean and standard deviation. For NTA analysis, samples were diluted in ultrapure water to reach a proper particles/frame value and underwent 5 sequential measurements at 25 ◦C using a Blue488 laser. The stability studies were carried out using a Turbiscan® DNS™ (Formulaction, Toulouse, France). QCM-D measurements were performed using an openQCM NEXT instrument (Novaetech S.r.l., Italy). Dialysis membranes of 6–27/32” Medicell International LTD (MWCO: 12–14,000 Da) were provided by Spectrum Laboratories Inc., Dalton, U.S.A.

Computational methods and analysis

SARS-CoV2-RBD Omicron structure was retrieved from Brookhaven Protein Data Bank (uniprot P0DTC2, pdb code 7yow) (http://www. wwpdb.org), was processed within the CHIMERA software [23]and minimized using AMBERff14 force field within AMBER 2020 suite [27].] performing progressive minimizations until the average root mean square deviation of the non–hydrogen atoms reached 0.3 Å. and used in molecular docking calculations. AAm structure was built in and minimized using Gaussian 09 at DFT/6–311 G* level of theory (PubChem CID: 6579) [ref]; the same protocol has been applied to AAc and its conjugate anion acrylate (PubChem CID: 4093), NIPAM (CID: 16637), nPMA (CID: 16638) and TBAm (PubChem CID:7877).

Autodock 4.2/MGLTools 1.5.7 was used to perform the molecular docking calculations [19]using the previously calculated charges at QM/DFT level for the ligands. Particularly we tested the cluster distribution considering different charge types (i.e. Mulliken, NBO), obtaining in the two cases a high correspondence of the clusters' distribution. Initially, a blind docking approach was used in order to identify every putative site on the Receptor Binding Domain (RBD) surface. To predict the probable arrangement of multiple monomer molecules around the protein, a detailed cluster analysis was performed and clusters that fall within the contact surfaces between monomeric chains in the trimeric association of the S protein were excluded from further analysis. Subsequently, on the lowest energy and most populated poses, a focused docking protocol has been applied to better refine both pose and its energy. For the Blind docking, the grid map, cantered in the centre of mass of the enzyme (126x126x126 Å3) included all the RBD surface; in the focused docking protocol, the grid map was centred on the ligand in the considered pose and extended around the cleft (40x40x40 Å3) with points spaced equally at 0.375 Å. The number of GA (genetic algorithm) runs was set to 150, the energy evaluations (25 000 000), the maximum number of top individuals that automatically survive (0.1) and the step size for translation (0.2 Å). All the docking calculations were carried out in triplicate using three different CPUs random seed. The final docked RBD-

monomer complexes were ranked according to the predicted binding energy and all the conformations were processed using the built-in clustering analysis with a 2.0 Å cutoff.

Synthesis of molecularly imprinted particles

Molecularly imprinted particles were synthesized as previously described [21], with minor adjustments.

Briefly, the water phase (1.0 mL), containing functional and crosslinking monomers, was sonicated and mixed with the SARS-CoV-2 receptor-binding domain. The oil phase, comprising deoxygenated hexane (22 mL), AOT (0,8 g), Span-80 (1,69 g), and Tween-80 (0,56 g), was prepared separately. The water phase was transferred into a 1 mL syringe, which was fitted with a 0.5-inch 30 G stainless steel needle. This syringe was then mounted onto a syringe pump (NE-1600, New Era Instruments, USA) to facilitate controlled injection into the oil phase. Using the syringe pump, the water phase was injected into the oil phase at a constant flow rate. The pump was calibrated to regulate this flow rate precisely, which was crucial for the formation of uniform spherical water-in-oil (W/O) droplets. By maintaining controlled flow conditions, we were able to optimize the droplet size and uniformity, thereby enhancing the overall stability and efficiency of the emulsion polymerization process. Polymerization was initiated with 10 % APS solution (100 μL) and TEMED (10 μL), and the reaction mixture was stirred for 2 hours. The resulting polymeric nanoparticles were precipitated with ethanol and washed with various solvents to remove unreacted components, surfactants, and templates. The polymeric material was then dried overnight. Non-imprinted polymers (NIPs) were synthesized under the same conditions but without the template.

Template removal

The removal of the template was performed through acid and base hydrolysis of the template molecule. To determine the efficacy of acid and base in degrading the template protein, BSA was used as a study model. BSA samples were placed inside dialysis membranes and immersed in 6 M HCl or 4 M NaOH solutions. Dialysis was conducted for three days against HCl/NaOH and subsequently for three days against water, at two different temperatures: room temperature and 50◦C. The dialysis process was halted when the pH of the dialyzed solution reached neutral, indicating the complete removal of hydrolyzing agents. After dialysis, the BSA content within the membranes was analyzed using spectrophotometry. This approach allowed for the evaluation of the hydrolysis conditions' effectiveness in removing BSA, providing an indirect indication of the protein template removal capability from the nanoparticles. In parallel, the same dialysis protocol was applied to MIP and NIP particles to assess their stability under varying pH and temperature conditions, and their integrity was evaluated using DLS.

Stability studies

Stability assessments were conducted by splitting the nanoparticles into six portions, each of which was then kept under specific conditions: controlled room temperature (25◦C ±2◦C), refrigeration (5◦C ±2◦C) and freezing (-20◦C ±2◦C). These conditions were tested both with and without the addition of 0.02 % (w/v) NaN_3 as a preservative [3]. Stability was also monitored for 24 hours after one day and again after 30 days post-synthesis using the Turbiscan® DNS™. Each 20 mL sample was placed in a cylindrical glass cell and maintained at 25◦C within the Turbiscan. The detection head featured a pulsed near-infrared light source (880 nm) along with synchronous transmission (T) and backscattering (BS) detectors. The T detector captured light that passed through the sample at a 180◦angle from the incident beam. The detection head scanned the entire 65 mm height of the sample cell, recording T values every 40 μm, resulting in 1625 acquisitions per scan.

ACE2: Spike RBD (SARS-CoV-2) inhibitor screening assay

To assess the efficacy of the synthesized MIPs in inhibiting the interaction between ACE2 and the receptor-binding domain of SARS- CoV-2, an Anti-SARS-CoV-2 (BA.2) Neutralizing Antibody Titer Serologic Assay Kit was employed as per the manufacturer's guidelines.

The microplate provided in the kit was pre-coated with Human ACE2 protein, facilitating the binding of relevant components during the experiment. MIPs and NIPs samples, along with Positive and Negative Controls, were carefully added to designated wells of the microplate. Following the addition of samples, HRP-SARS-CoV-2 S protein RBD was introduced into each well, allowing for specific interactions with target molecules. The microplate was then incubated under controlled conditions, allowing for the formation of complexes between the particles and the template. Post-incubation, thorough washing of the wells was performed to remove any unbound materials, ensuring the accuracy of subsequent steps. Substrate Solution was added to each well, initiating the enzymatic reaction. This reaction was terminated by the addition of Stop Solution and the intensity of absorbance was measured at 450 nm/ 630 nm using a microplate reader, providing quantitative data on the interactions within the microplate. The competition between neutralizing nanoparticles in the samples and ACE2 for HRP-SARS-CoV-2 S protein RBD binding was assessed. The intensity of the assay signal decreased proportionally with the concentration of Anti-SARS-CoV-2 neutralizing synthetic antibodies.

Preparation of IP-QCM Sensor and Detection of protein binding via QCM

A cleaned QCM-D chip was placed in a petri dish and submerged in 4 mL of a thiol solution containing 5 mM of 16-Mercaptohexadecanoic acid (MHA) and 5 mM of 11-Mercapto-1-undecanol (MU) dissolved in a 8:2 mixture of absolute ethanol and acetic acid. This process was conducted at room temperature for 18 hours in the dark, allowing the formation of a Self-Assembled Monolayer

(SAM) on the gold surface to enhance subsequent binding interactions. Following the thiol solution treatment, the chip was washed several times with absolute ethanol and dried with N2. To activate the carboxylic groups of MHA, 100 µL of a sulfo-NHS:EDC solution (1:1, 100 mg/mL in ddH2O) was applied for 60 minutes, followed by washing with ddH2O and drying with N2. For the immobilization of Omicron RBD domain, a standard solution was prepared at a concentration of 10 µg/mL in ddH2O. This solution was injected into the QCM-D instrument to confirm the amount of analyte bound to the sensor surface. To validate the specificity of the imprinted nanoparticles, the same immobilization procedure was applied to HSA.

The experiments, designed to investigate the binding interactions of MIP and NIP with Omicron-RBD domain, were conducted using different concentrations of the nanoparticles (12.5, 25, 50, and 100 µg/mL). The fundamental frequency was approximately 5 MHz. To establish a stable baseline, the frequency signal was calibrated by injecting ddH2O for one hour at a flow rate of 10 µL/min until the frequency signal response stabilized within ±0.5 Hz over a ten-minute period. Following this calibration, the samples were introduced into the QCM-D instrument at the same flow rate for 50 minutes for each concentration. The QCM-D instrument recorded the frequency changes, which corresponded to the binding events between the polymers and the analyte, providing insights into the binding affinity and kinetics of these interactions. To further assess the specificity of MIP for detecting RBD domain, additional experiments were conducted where HSA was immobilized on QCM sensor chips. The binding interactions of MIP and NIP with these immobilized proteins were analysed using the same concentrations as in the initial experiments. All experiments were performed in triplicate.

Cytotoxicity test

The cytotoxicity of the nanoparticles was assessed using the MTT assay (1-(4,5-Dimethylthiazol-2-yl)-3,5-diphenyltetrazolium). BALB- 3T3 cells were cultured in 48-well plates with complete media

and allowed to adhere for 24 hours. Following attachment, the cells were treated with varying concentrations of both MIP and NIP nanocarriers to determine their cytotoxic effects. At the conclusion of the treatment period, 200 µl of MTT stock solution (2 mg/mL in PBS) was added to each well and incubated for 3 hours at 37◦C. Post-incubation, the MTT solution was discarded, and 200 µl of DMSO was added to each well to solubilize the formazan crystals. The plate was shaken for 15 minutes, and the absorbance was measured at 570 nm using a Beckman Coulter microplate reader. Cell viability was expressed as a percentage relative to the control cells, which were considered 100 % viable. All experiments were conducted in triplicate, and the data are presented as mean values with standard deviations indicated by error bars.

Human Cell Line Activation Test (h-CLAT)

The Human Cell Line Activation Test (h-CLAT) is designed to determine the potential of substances or mixtures to induce skin sensitization through immune system activation. This assay follows the protocols set by OECD 442E and EURL ECVAM [17]. The THP-1 human leukemia monocytic cell line is used to assess the expression of co-stimulatory molecules CD54 and CD86, with nickel sulfate ($NiSO_4$) serving as a positive control. THP-1 cells were cultured in RPMI 1640 medium supplemented with 10 % FBS, 1 % Penicillin/Streptomycin, and 0.05 mM β-Mercapto-ethanol. To determine the CV75 (concentration causing 25 % mortality) in accordance with Test No. 442E: In Vitro Skin Sensitization, 1.5×10^5 cells per well were plated in a 96-well plate and incubated under standard conditions. After incubation, the cells were treated with the test substances at eight different concentrations. The next day, the treated medium was removed via centrifugation, and the cells were resuspended in FACS buffer containing propidium iodide (PI). The CV75 was calculated using flow cytometry. For the h-CLAT, 5×10^5 cells per well were plated in 24-well plates and incubated for 24 hours. Following incubation, treatments were applied, and the cells were incubated for another 24 hours. Nickel sulfate solution (100 µg/mL) and culture medium served as positive

and negative controls, respectively. Post-incubation, cells were centrifuged, resuspended in FACS buffer, and divided into three aliquots. These aliquots were then treated with a blocking solution (FACS buffer containing 0.01 % γ-globulin) for 15 minutes at 4◦C, followed by incubation with fluorescein-conjugated antibodies against CD86, CD54, or IgG1 (control) for 30 minutes at 4◦C. After antibody incubation, cells were washed twice with FACS buffer to remove unbound antibodies, resuspended in FACS buffer containing PI, and analyzed via flow cytometry. To assess whether the test substance is a sensitizer, the Effective Concentration (EC) values for CD86 and CD54 were determined. The EC represents the concentration at which the Relative Fluorescence Intensity (RFI) equals 150 or 200, respectively. Each experiment was repeated in triplicate on three different days, and the median EC150 and EC200 values from three independent runs were reported. If only two of the three runs met the positive criteria, the higher EC150 or EC200 value was used. An increase in CD54 and CD86 expression on THP-1 cells indicates immune activation in response to a potential allergen.

RESULTS AND DISCUSSION

This study introduces a novel application of MIPs targeting the RBD of the SARS-CoV-2 Omicron variant S protein, presenting MIPs as a promising synthetic alternative to antibodies. Following the already tested computational protocol [21], a rational selection of an appropriate monomer for MIP selectively rebinding the Omicron variant S protein in its RBD domain has been carried out. Molecular docking combined with quantum chemical calculations was used for modeling and comparing different monomers affinity and their ability to polymerize onto the Receptor Binding Motif (RBM) portion of the S protein, thus preventing its binding to ACE2 receptor.

The used approach has foundation on the considerable amount of different functional groups present in the target protein that creates potential premises for multiple noncovalent interactions (H-bond, van der Waals, electrostatic, and/or hydrophobic) between the protein and functional monomers in a pre-polymerization complex before protein- MIP synthesis. It can be assumed that these interactions can orient the polymerization process and play a crucial role in the formation of complementary binding sites after the template protein removal, that is necessary for the subsequent selective rebinding of the target protein to the MIP. On this basis, the evaluation of all possible noncovalent interactions binding sites as well as their strength in the protein-monomer complex must be taken into account for the aim to design MIPs targeting specific proteins with highly selective recognition sites. Here, the aim is to compare, using a molecular modeling approach, the different capability of different functional monomer for building a polymer with macromolecular imprints capable of selectively rebind protein-sized analytes.

Molecular docking was applied to find both energetically favorable binding poses of the selected functional monomer on the model protein and to predict the probable arrangement of multiple monomer molecules around the macromolecular target. A particular attention has been put in partial charges calculation on the functional monomers since the small dimension of the molecules

considered (AAm, AAc/acrylate, NIPAM, nPMA, TBAm), will allow them to easily binds on the protein target surface, and the electron density and charge distribution are primary responsible of the electrostatic/hydrophobic noncovalent complex stabilization.

The approach was based on using the docking of each of the monomers throughout all the RBD surface to determine the energetically favorable binding poses and finally to assess the cumulative strength of H-bond interactions between the monomers and the sterically accessible proton-acceptor groups of RBD, such as polar amino acid. The most populated clusters for all the considered monomers are highlighted in Table 1.

Cluster n.	**AAm**	**Cluster n.**	**AAc**	**Cluster n.**	**NiPAM**	**Cluster n.**	**nPMA**	**Cluster n.**	**TIBAm**
Cl1 (29%)	-14.5	Cl1 (7%)	-16.6	Cl1 (88%)	-18.8	Cl1 (15%)	-22.3	Cl1 (78%)	-20.10
Cl2 (5%)	-14.2	Cl2 (12%)	-.16.0	Cl2 (6%)	-17.0	Cl2 (18%)	-21.8	Cl2-Cl3 (25%)	-19.1
Cl3 (2%)	-14.1	Cl3 (57%)	-15.8			Cl3-Cl6 (15 %)	-20.9/-19.1	Cl4 (8%)	-17.7
Cl4 (16%)	-14.0	Cl4 (24%)	-15.7			Cl7 (37%)	-19.0	Cl5 (9%)	-15.9
Cl5 (18%)	-13.9								

Table 1. Most populated clusters for the considered monomers in kJ/mol. "Close/Near RBM" clusters are highlighted in red, while "Far from RBM" clusters are highlighted in blue.

The results obtained from the docking of AAc identified a close cluster distribution. We excluded those poses that are not accessible to the SAS (Solvent Accessible Surface) surface or that lie at the interface between monomers in the trimeric S protein association (pdb code 6vsb), and we observe that among the selected clusters two zones are covered, being one on the center of the RBM portion of the RBD domain. As can be seen in Fig. 1, they are distributed with cluster population of Cl1 (7 %) far from RBM, Cl2 (12 %) RBM), Cl3 57 % lateral, Cl4 24 % near Cl3. This spread distribution,

together with a comparable population percentage, and comparable binding energy suggest that this monomer can efficiently binds and include the RBM portion of the target protein occupying positions that can efficiently lead to the desired polymerization process.

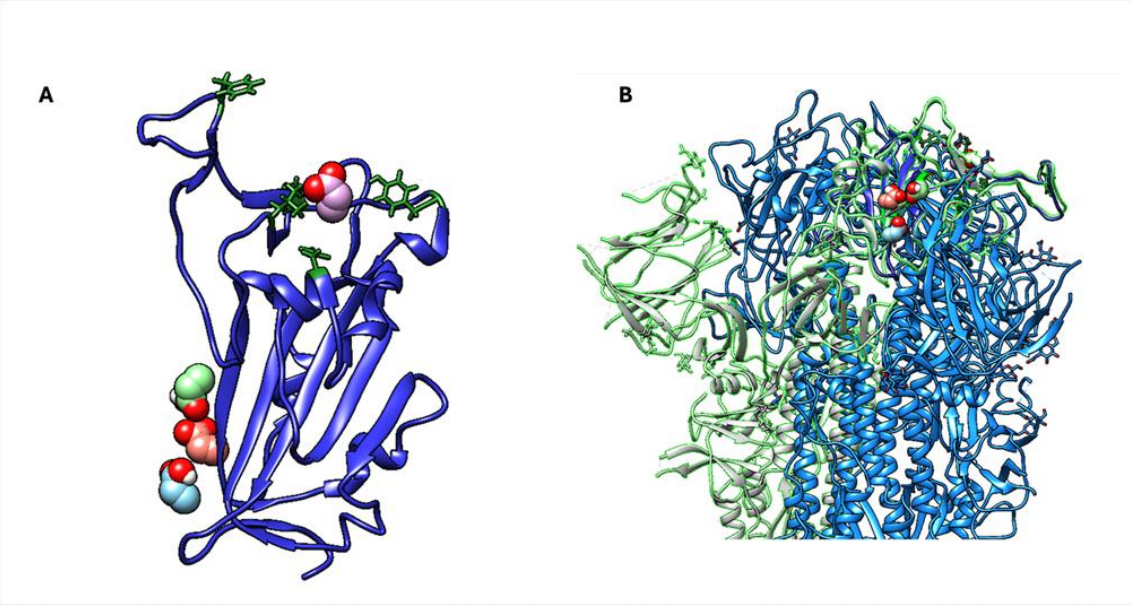

Fig. 1. AAc clusters distributions accessible to solvent surface on RBD domain of spike protein (8uir). (A) In forest green are highlighted the 6 key residues implicated in ACE2 binding (resuled 417,455, 486 493,494, 501). (B) Superimpostion of RBD 7yow with docked clusters for AAm and 8uir.

The results obtained from the docking of AAm showed the existence of several accessible clusters but with high different populations spread all over the RBD surface. The most populated cluster (29%) is located within the RBM-6 residues portion. The other four clusters are dispersed around the RBD, but they are not near the six key residues; instead, they are situated in the outer region relative to the contact surface (Fig. 2). More, the Cl4 has 16% pop and Cl5 18%. The populated distribution of these clusters together with the highest population of the binding pose in the RBM, suggest that AAm is highly suitable to be considered as a promising monomer for targeted polymerization (Fig. 3).

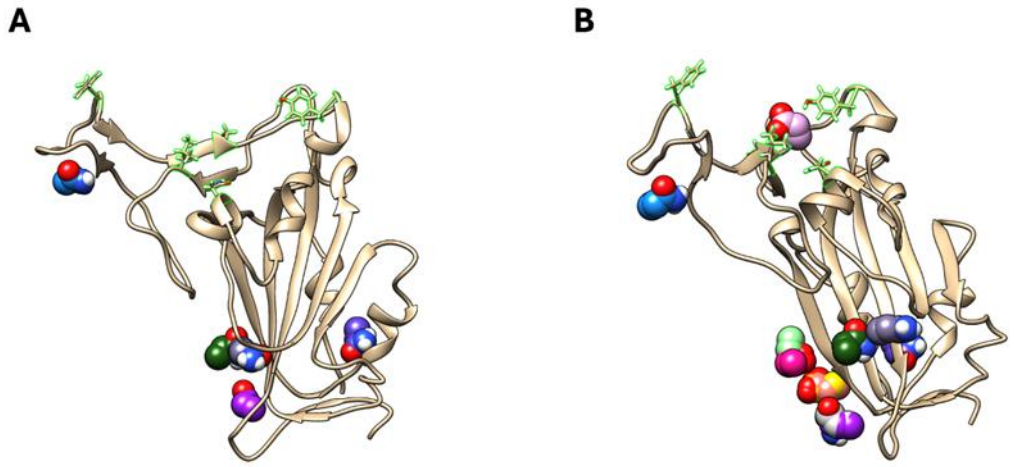

Fig. 2. (A) AAm clusters (spheres) distributions accessible to solvent surface on RBD domain of spike protein (gold ribbons). In green are highlighted the 6 key residues implicated in ACE2 binding (resuled 417,455, 486 493,494, 501). (B) AAm clusters together with AAc ones (CPK spheres, RBD in ribbons).

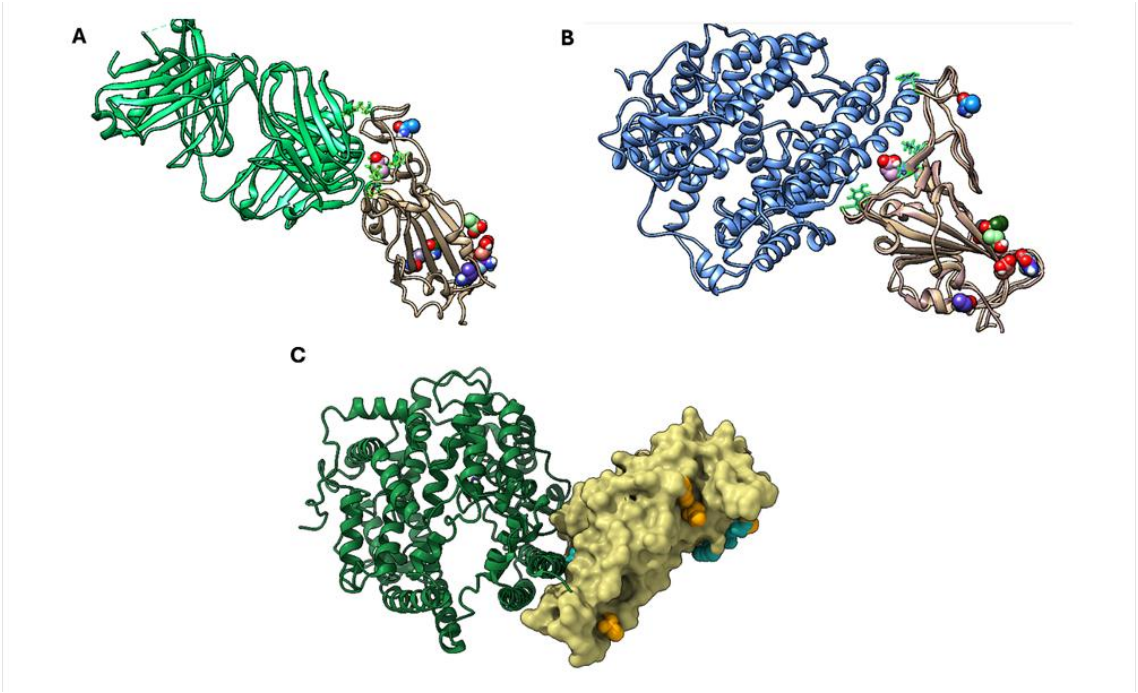

Fig. 3. (A) AAm and AAc clusters (CPK spheres) distributions accessible to solvent surface on RBD domain of spike protein (gold ribbons) in complex with NCV2SG48 Fab (watergreen ribbons) (7yow). In green are highlighted the 6 key residues implicated in ACE2 binding (resuled 417,455, 486 493,494, 501). (B) Aam and AAc clusters (CPK spheres) distributions accessible to solvent surface on RBD domain of spike protein (gold ribbons) in complex with ACE2 receptor (blue ribbons) (7c8d). In green are highlighted the 6 key residues implicated in ACE2 binding (resuled 417,455, 486 493,494, 501). (C) Same as B but RBD is shown with its molecular surface; AAm in yellow CPK, AAc in cyan CPK.

Building on the previous results, an emulsion polymerization reaction was employed to synthesize imprinted nanoparticles with high specificity and functionality using AAm and AAc as functional monomers. Emulsion polymerization offers numerous advantages, including high yield and good reproducibility. Additionally, this method is particularly suitable for protein imprinting due to its ability to produce nanoparticles with specific binding sites for target molecules. MIPs obtained through this process exhibit significant potential in various applications, such as controlled drug release, protein purification, and the development of highly specific sensors [9]. In this work, a water-in-oil emulsion system was utilized, where the aqueous phase contained the monomers, cross-linking agents, and template molecules. These components were meticulously dispersed into the oil phase, which consisted of an immiscible solvent. The role of surfactants was paramount in this setup, as they facilitated the formation of a stable emulsion by reducing the interfacial tension between the aqueous and oil phases. The injection system setup was crucial for forming a stable emulsion and achieving nanosized particles. The fine gauge of the 30G stainless steel needle allowed for precise control over the injection of the water phase into the oil phase, promoting the formation of uniform spherical droplets. Coupled with the syringe pump's ability to regulate flow rates meticulously, this setup ensured consistent droplet size and distribution, which are essential for producing nanosized particles with high stability. This approach not only enhanced the reproducibility of the emulsion but also optimized the overall efficiency of the polymerization process. The careful selection of monomers and cross-linking agents, combined with the optimized emulsion conditions, was crucial in achieving nanoparticles with the desired physical and chemical properties. The obtained nanoparticles were analyzed in terms of size, polydispersity index (PdI), and ζ-potential using DLS. The results for MIPs and NIPs are shown in Table 2and Fig. 4:

	Z-Average	**PdI**	**ζ-potential (mV)**
MIP	40.24 ± 6.383	0.183	-33.3 ± 8.14
NIP	35.95 ± 5.467	0.213	-34.2 ± 5.89

Table 2. Z-Average size, PdI and ζ-Potential Data for MIPs and NIPs

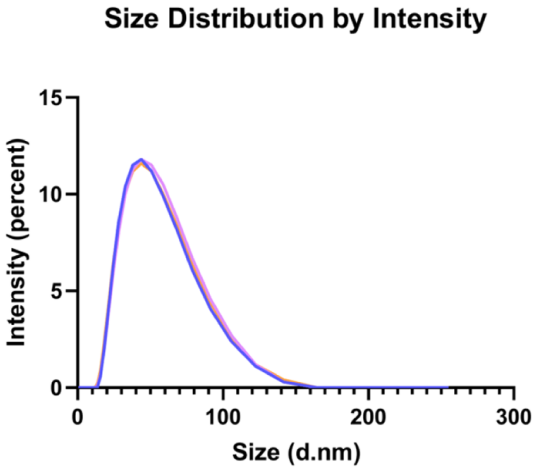

Fig. 4. Hydrodynamic diameter of MIP particles measured by DLS.

The MIP nanoparticles exhibited an average size of 40.24 ±6.383nm, while the NIP nanoparticles had a slightly smaller average size of 35.95 ±5.467nm. Although the difference in average sizes is not substantial, it suggests that MIPs tend to be slightly larger than NIPs, likely due to varying interactions between monomers and the template.

Both MIP and NIP nanoparticles had a PdI of less than 0.3, indicating a relatively narrow size distribution and good size uniformity. In number, the main population of NPs have instead a mean diameter of 124 nm, whereas the peak centered at 60 nm accounts for less than 4 % of the total number of particles (5.98 ×10 8 ±7.6×10 7 particles/mL). NTA analysis also highlighted a small percentage (about 3.7 %) of nanoparticles having a mean diameter of 200 nm (Fig. 5).

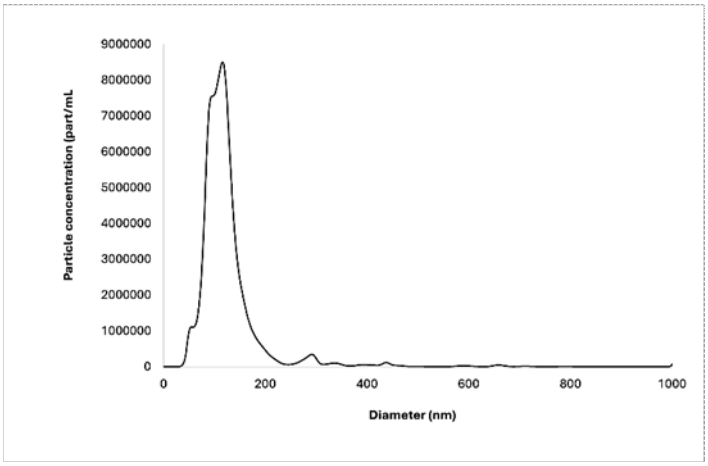

Fig. 5. Exemplification of the NTA pattern of MIP

Additionally, the ζ-potential measurements for both MIP and NIP nanoparticles were negative and of similar magnitude, indicating that both types of nanoparticles are stable in suspension due to sufficient electrostatic repulsion, which prevents aggregation (Table 2). To confirm the consistency of the data, TEM images were used to determine the particle size of MIPs (Fig. 6). The analysis showed that the particles had a spherical shape and sizes comparable to those obtained from DLS measurements.

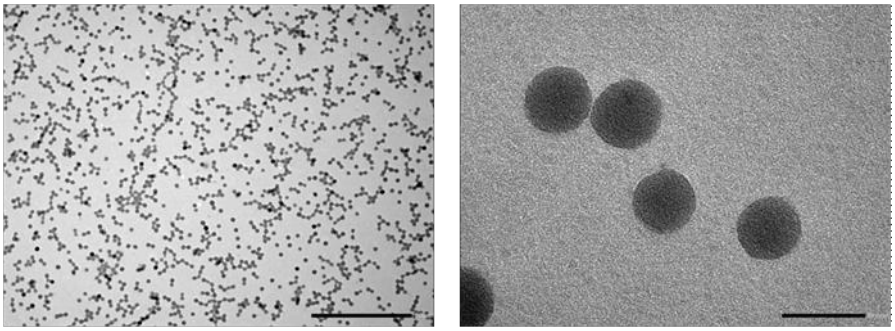

Fig. 6. TEM Micrographs of MIP particles

In summary, the results indicate that MIP and NIP nanoparticles have comparable sizes and stability. MIP nanoparticles are slightly larger with a narrower size distribution compared to NIP nanoparticles. The high stability of the nanoparticles, evidenced by ζ-potential values, confirms their suitability for various applications.

Template removal is a crucial step for the optimal performance of MIPs, ensuring no template molecule residues occupy the active sites within the particle structure, making them available for rebinding the target molecule [8]. Various methods can be used for removal, including protein hydrolysis, which was employed in this work. This method was chosen because the template molecule, in this case, is a protein too large to pass through a common dialysis membrane. Therefore, the protein must first be hydrolyzed into smaller fragments, which can then be dialyzed and removed from the imprinted polymer.

After completing the BSA tests and defining optimal hydrolysis conditions (Fig. 2S), alkaline hydrolysis was performed on particles imprinted with the SARS-CoV-2 RBD and their

corresponding NIP (Fig. 3S). Dialysis waters were lyophilized, concentrated, and analyzed for RBD presence via spectroscopy, indicating a template removal efficiency of 96 ± 2.6 %. These overall results indicate that alkaline hydrolysis at 50◦C is the optimal combination for ensuring both effective template removal and polymer stability. After complete dialysis, the final particles suspension concentrations, based on lyophilized masses, were approximately 14.68 mg/mL for MIP and 9.64 mg/mL for NIP, corresponding to yields of about 82.98 % and 78.21 %, respectively.

Nanomedicines will not achieve success as pharmaceutical products until they undergo comprehensive evaluation of various quality aspects, particularly pharmaceutical stability during storage. Stability testing is essential in drug development to assess how a product's quality changes over time under environmental factors like temperature, humidity, and light. This testing helps establish the drug's shelf life and recommend suitable storage conditions [20]. Stability tests over time were performed in the presence or absence of sodium azide as a preservative, under different temperature conditions [3]. Sodium azide was chosen for its common use in antibody preservation, preventing microbial contamination. The goal was to evaluate variations in dimensional parameters, such as size, PdI, and ζ-potential, under different storage conditions. A PdI value up to 0.3 indicates a relatively narrow size distribution and particles with ζ-potential values of ± 30 mV are considered highly stable. Results after 24 hours and after 30 days are shown in Figs. 4S and 5S, respectively. Results after 24 hours indicate that samples stored at 25◦C with NaN3 show an increase in size and PdI compared to samples stored without NaN_3 at the same temperature, while ζ-potential slightly decreases (Figure 4SA). Samples stored at 4◦C with NaN_3 show a slight difference in both size and PdI, and a significant decrease in ζ-potential compared to those stored without the preservative (Figure 4SB). Finally, samples stored at - 20◦C with NaN_3 show no significant variations in examined parameters (Figure 4SC). These results indicate that NaN_3 presence can influence the dimensional stability and ζ-potential of nanoparticles, with variations depending on storage temperature. Storage at room temperature with NaN_3 leads to an increase in size and PdI,

suggesting possible interactions between the preservative and nanoparticles. Conversely, storage at lower temperatures (4◦C and 20◦C) seems to mitigate these effects, maintaining the nanoparticles' properties more stable over time.

After 30 days of storage at 25◦C, the addition of the preservative has a consistently negative effect on all three parameters, as illustrated in Fig. 5S. Similar detrimental effects are observed during storage at 4◦C. At - 20◦C storage, the presence of NaN_3 results in a slight increase in both size and PdI, while the ζ-potential remains stable. Based on the data obtained, it can be concluded that the developed synthetic antibody in this study demonstrates exceptional stability at room temperature, highlighting its practicality for routine use and storage. The observed dimensional changes over the evaluation period were minimal and statistically insignificant. Moreover, the most favorable results were achieved in the absence of a sodium azide. This characteristic presents a significant advantage over biological antibodies, which necessitate stringent storage conditions, including specific temperatures and the maintenance of a cold chain during transport, as well as the addition of preservatives. Therefore, the synthetic antibody could be a more viable option for various applications where stability and ease of storage are critical.

The stability of nanoparticles suspensions, prepared in both distilled water and PBS at pH 7.4 (10^{-3} M), was further evaluated using a Turbiscan® DNS™. This technique measures changes in the intensity of light transmitted (ΔT%) and backscattered (ΔBS%) by the sample. These measurements are then converted into a global stability kinetics value, represented by the Turbiscan Stability Index (TSI) [5]. Figs. 6S and 7S illustrate the changes in ΔT% and ΔBS% as a function of sample height and time in the suspensions, analyzed at both one day and 30 days post-synthesis. The data reveal that the samples maintained their stability over the observed periods, with variations in both parameters consistently within a 10 % range throughout the 24-hour analysis. The positive variation in ΔT% at the top of the samples, observed consistently at both time points, indicates a creaming phenomenon, which was reversible upon slight agitation. In the midsection of the samples, both

backscattering and transmission measurements remained stable, indicating no significant particle aggregation or size variation. These findings suggest that the observed destabilization is primarily due to the migration of particles, rather than changes in particle size, and that the colloidal stability of the suspensions is preserved even after 30 days.

Moreover, the TSI, a destabilization factor calculated by summing changes in ΔT% or ΔBS% of the light in successive measurements as a function of sample height, remained low (TSI < 0.9), confirming the stability of the imprinted nanoparticles in both water and PBS (Table 3).

	Analysis after one day				**Analysis after 30 days**			
	4 h	**8 h**	**12 h**	**24 h**	**4 h**	**8 h**	**12 h**	**24 h**
H_2O	0.14 ± 0.09	0.15 ± 0.11	0.16 ± 0.14	0.28 ± 0.13	0.32 ± 0.10	0.44 ± 0.09	0.51 ± 0.12	0.60 ± 0.14
PBS	0.52 ± 0.08	0.62 ± 0.011	0.65 ± 0.14	0.76 ± 0.11	0.45 ± 0.07	0.55 ± 0.12	0.58 ± 0.15	0.81 ± 0.06

Table 3. Turbiscan Stability Index (TSI) of imprinted particles in distilled water and PBS at various time intervals, measured one day and 30 days post-synthesis. Results are presented as means ± standard deviation (n = 3).

The stability assessments conducted in this study reinforce the practical viability of MIPs in field and clinical settings. Unlike natural antibodies, MIPs displayed minimal degradation or aggregation over 30 days, maintaining their structural and colloidal integrity, even at room temperature. This stability under ambient conditions could be particularly valuable in low-resource settings, where cold-chain logistics are challenging or impractical. By offering a reliable and durable alternative to biological reagents, MIPs could become central to diagnostic kits and therapeutic formulations.

Once the MIPs were synthesized, their ability to inhibit the interaction between the ACE2 receptor and the SARS-CoV-2 RBD (BA.2) was evaluated using a neutralizing anti-SARS-CoV-2 antibody assay kit. Data were obtained by measuring the absorbance intensity at 450 nm/ 630 nm using a microplate reader. Specifically, the competition between the neutralizing nanoparticles in the sample and ACE2 for binding to the horseradish peroxidase-conjugated SARS-CoV-2 S protein RBD molecules was assessed. Imprinted and non-imprinted nanoparticles were tested at different concentrations ranging from 0.1 ng/µL to 500 ng/µL. The obtained results (Fig. 7A) confirmed the

ability of the developed system to reduce RBD binding to the ACE2 receptor in a concentration-dependent manner. In fact, the graph shows that for the MIP, as the polymer concentration increases, the inhibition percentage also increases; this is expected as the imprinted polymer contains cavities necessary to interact with the SARS-CoV-2 RBD, thus preventing its interaction with the ACE2 receptor. Conversely, the NIPs did not exhibit significant inhibition of the RBD-ACE2 interaction. The absence of specific binding cavities in the NIPs, which are crucial for binding the template molecule, accounts for this lack of inhibition. The minor inhibition observed with the NIPs is likely due to non-specific interactions with the target molecule.

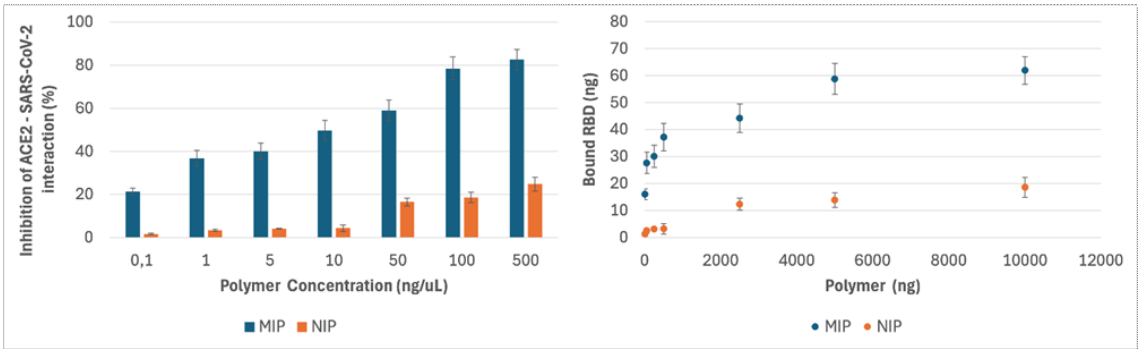

Fig. 7. Inhibitor Screening Assay: (A) Inhibition of ACE2-SARS-CoV-2 RBD interactions and (B) binding isotherms of 1,5 µg/mL SARS-CoV-2 RBD to imprinted and non-imprinted nanoparticles.

Furthermore, the collected data were used to calculate the amount of SARS-CoV-2 RBD bound to the polymers (MIP and NIP). The results are shown in Fig. 7B and confirm that MIPs are capable of binding a greater amount of the template molecule compared to the corresponding non-imprinted particles.

The mechanism by which MIPs inhibit RBD-ACE2 binding suggests that the synthetic polymer matrix successfully mimics the binding characteristics of natural antibodies, a significant achievement in the field of molecular imprinting. The imprinted cavities in MIPs provide a highly selective environment that aligns with the spatial and chemical properties of the RBD, enabling strong and specific interactions. These cavities create a template-like effect that physically blocks the RBD from engaging with the ACE2 receptor, a critical step in viral entry. This selective

inhibition, observed through this competitive binding assays, demonstrates that MIPs can effectively reduce viral infectivity by impeding the initial stages of the virus-host interaction.

To further highlight the functionality of MIP particles, comprehensive binding studies were performed using a QCM-D instrument. The process began with the functionalization of the sensor surface using a SAM composed of a mixture of MHA and MU, which act as spacers to enhance the interaction between the gold coating and the analyte. MHA was then attached using sulfo-NHS:EDC coupling chemistry. Changes in resonant frequency, shown in Fig. 8, were used to monitor the binding progression.

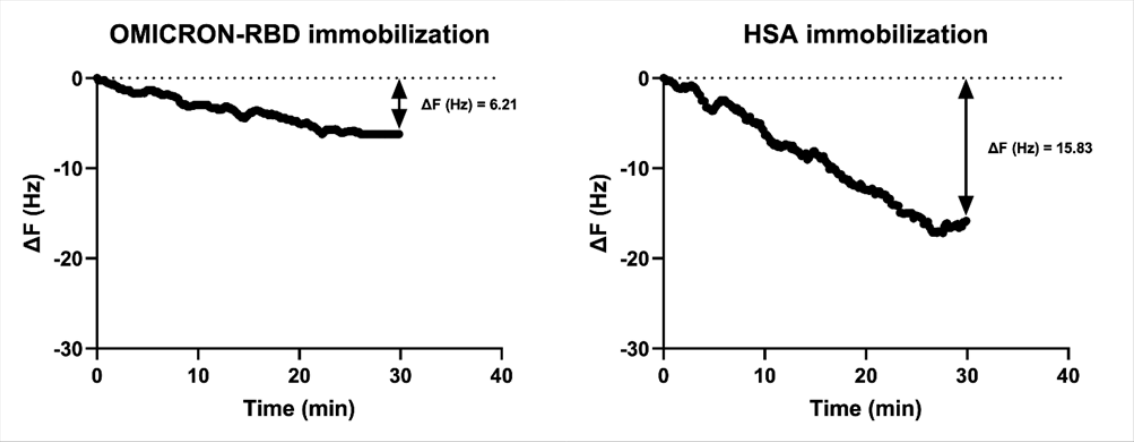

Fig. 8. Analyses of QCM-D sensor modification with RBD domain of Omicron variant and HSA.

Using the Sauerbrey equation [26], the quantities of analytes on the sensor surface were determined, revealing an RBD density of 8.19 $\times 10^{-13}$ mol/cm^2 and an HSA density of 8.43 $\times 10^{-13}$ mol/cm^2. These functionalized QCM chips were then used to evaluate the binding interactions of MIP and NIP with analyte and control. The introduction of varying concentrations of nanoparticles results in a concentration-dependent frequency change, as depicted in Fig. 9.

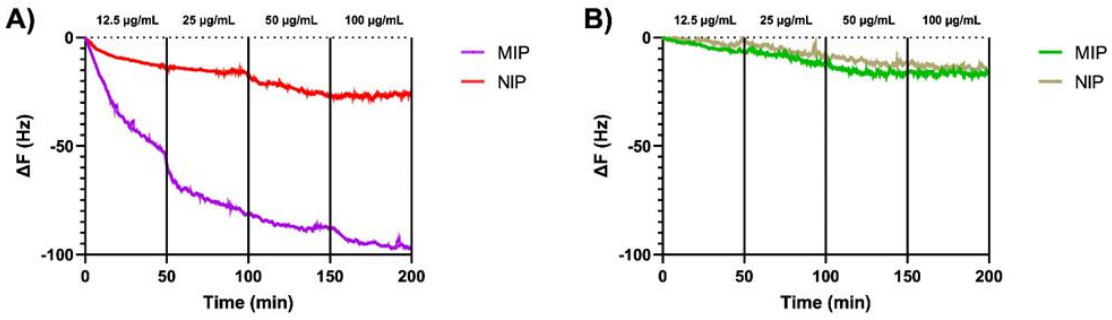

Fig. 9. Real-time changes in resonant frequency (ΔF) after repeated injections of increasing concentrations of MIP and NIP dispersions on functionalized QCM-D sensor chips with (A) RBD and (B) HSA.

The highest resonant frequency changes were observed (Fig. 9A), indicating strong affinity of MIP for Omicron-RBD at low concentrations. As the concentration of MIP increased, the affinity remained stable, reaching saturation after 180 minutes of injection. The introduction of the MIPs resulted in significant decreases in frequency compared to the injection of dispersions containing NIP that have the same chemical composition. This observation underscores the importance of the MIPs cavities in facilitating the recognition of the template molecules. These imprinted cavities are more effective in distinguishing and binding to the target molecules than the non-specific intermolecular interactions that occur on the surface of the nanogel [15]. A different result was observed when MIPs and NIPs were injected onto QCM-D sensors functionalized with HSA, as shown in Fig. 9B. The affinity for HSA was notably low for both MIPs and NIPs, which underscores the high specificity and effectiveness of the selected imprinting technology in distinguishing between different proteins. As depicted in Fig. 10, this result demonstrates that the imprinting technique is highly selective, ensuring that the MIPs are specifically tailored to recognize and bind to their target molecules rather than interacting with non-target proteins like HSA.

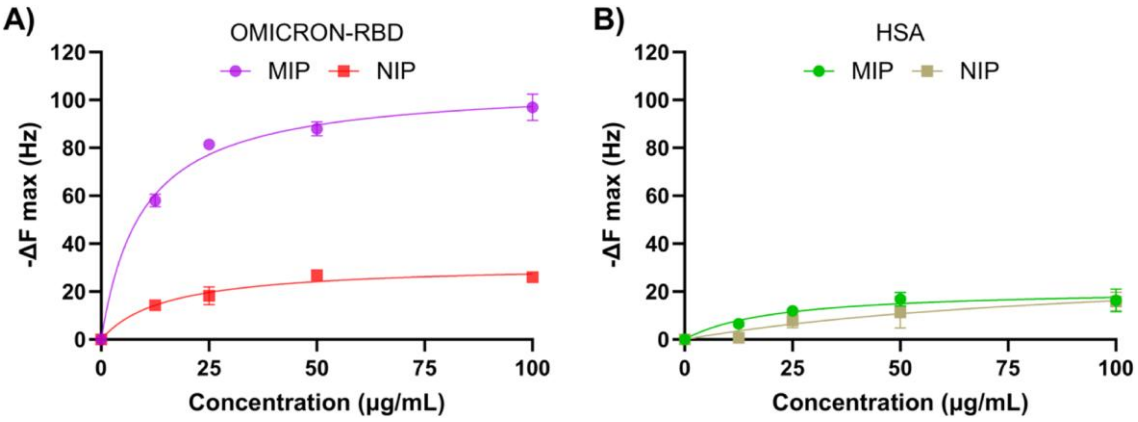

Fig. 10. Binding isotherms of MIP and NIP on OMICRON-RBD (A) and HSA (B) functionalized sensor chip.

Apparent dissociation constants (*KD*) were derived by fitting the Langmuir isotherm to the experimental data collected from the QCM frequency shift measurements (Table 4) [6].

	Omicron-RBD		HSA	
	K_D	R^2	K_D	R^2
MIP	9.5±5.4	0.99	21.0±14.3	0.96
NIP	15.0±8.7	0.97	22.3±15.8	0.94

Table 4. Equilibrium dissociation constant (KD) of MIP and NIP.

These results serve to emphasize and elucidate the considerable promise and effectiveness of MIP particles as a versatile and potent tool for specifically recognizing RBD, compared to NIP, where MIPs demonstrate a higher degree of selectivity towards RBD with an approximative *KD* of 9.5. A higher *KD* was observed for HSA, while R2 was lower than RBD R2 value. This observation underscores the unique capacity of MIPs for precise molecular recognition. Furthermore, MIP exhibit a robust and tailored recognition capability for template, suggesting their substantial potential and applicability in the treatment and prevention of SARS-CoV-2 infection.

Safety evaluations were conducted to assess potential cytotoxicity and immunogenicity of the test substances. These evaluations employed two established in vitro methods: the MTT assay and the human Cell Line Activation Test (h-CLAT).

The MTT assay offers a quick and economical approach to evaluate cell proliferation. This technique hinges on the conversion of the yellow tetrazolium compound into violet/black insoluble

formazan crystals by living cells. Results from MTT assays performed on Balb/3T3 cells, following treatment with escalating concentrations of nanoparticles, showed no notable reduction in cell viability (Fig. 11). The nanocarriers exhibited no toxicity to viable cells, demonstrating their biocompatibility.

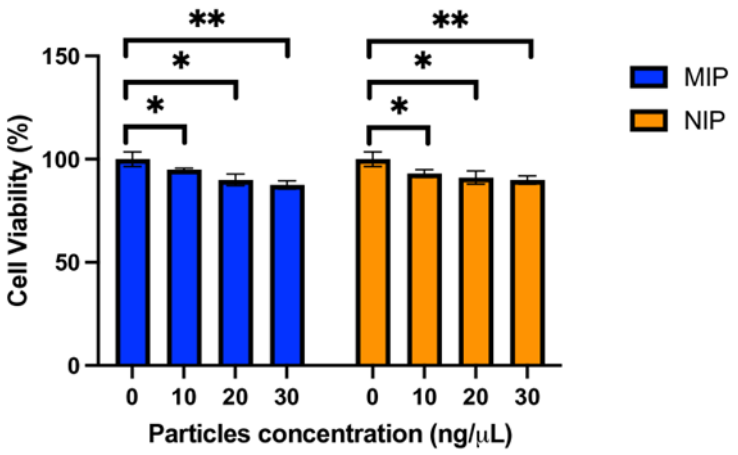

*Fig. 11. Cell viability: the MTT test was conducted on Balb/3T3 cells following a 24-hour exposure to escalating concentrations of MIP and NIP. Data are expressed as means ± SEM, statistical significance: *p < 0.05, **p < 0.01.*

Moreover, to determine the sensitizing potential of MIP and NIP, the h-CLAT was conducted following the guidelines of OECD 442E. This assay measures the expression levels of CD86 and CD54 markers in THP- 1 cells. These levels are assessed based on their activation capacity using flow cytometry after a 24-hour exposure to eight serial concentrations of the test substances. The concentrations used are derived from a preliminary cytotoxicity study that identifies the CV75 of the compound on the cells.

The sensitization potential of the test items was evaluated using the Relative Fluorescence Intensity (RFI%) values for CD86 and CD54. A substance is predicted to be a sensitizer if the RFI% value for CD86 is ≥150 % and/or the RFI% value for CD54 is ≥200 % in at least two independent runs. Conversely, a negative prediction for sensitization is made if the RFI% value for CD86 is <150 % and/or the RFI% value for CD54 is <200 %.

The results, presented in Table 5, indicate that the tested samples did not exhibit skin sensitizing properties, affirming the overall safety and biocompatibility of the nanoparticles.

In summary, the adaptability of MIPs makes them a versatile platform for managing infectious diseases, especially zoonotic diseases with high mutation rates. In this study, the methodology used to imprint SARS-CoV-2 RBD can be applied to other pathogens, suggesting that MIPs could serve as a foundational technology in pandemic preparedness. By altering the imprinting process to reflect different viral proteins or epitopes, MIPs can be readily adapted to recognize new targets, providing a rapid-response solution that could accelerate diagnostics and therapeutic interventions in future outbreaks.

SAMPLES	**CD54**	**CD86**
MIP	141	121
NIP	133	119
NEGATIVE CONTROL	110	101
POSITIVE CONTROL	301	277
CUT-OFF	200	150

Table 5. RFI% value of CD54 and CD86 on THP-1 monocytes.

CONCLUSION

The development of MIPs as synthetic antibody alternatives represents a significant advancement in the fight against rapidly evolving pathogens, like SARS-CoV-2. This study focused on engineering MIPs to selectively bind the RBD of the Omicron variant S protein, demonstrating that MIPs can serve as both diagnostic and potential therapeutic tools in controlling viral spread.

Stability assessments demonstrated that these MIPs remained well- dispersed and stable under various conditions, including room temperature, refrigeration, and freezing, over a 30-day period. The stability was consistently confirmed by stable TSI values, indicating that the MIPs preserved their functional properties throughout this time frame and emphasizing their suitability for long-term storage and scalability. MIPs exhibited significantly higher binding efficacy compared to NIPs, due to the specific imprinting of the RBD during their synthesis. This process endowed the MIPs with enhanced binding capabilities, whereas NIPs lacked these specific binding sites, leading to much lower affinity for the RBD. Additionally, MIPs demonstrated a concentration-dependent inhibition of the interaction between the ACE2 receptor and the RBD, with higher concentrations resulting in greater inhibition. Quantitative analysis of binding affinity demonstrated that MIPs achieved an apparent dissociation constant of 9.5 for the RBD, showcasing a strong and specific interaction with the target protein, which contrasts markedly with the limited binding efficacy of NIPs. The QCM-D studies underscored the MIPs significant potential for precise molecular recognition and application in SARS-CoV-2 detection and treatment, compared to NIPs and non-target proteins like HSA.

Further tests confirmed the biocompatibility of MIPs, as shown by the MTT assay on Balb/3T3 cells, which indicated that neither MIPs nor NIPs were significantly cytotoxic, suggesting their potential for therapeutic applications. The h-CLAT also indicated no sensitizing potential, thus supporting the MIPs' safety for biomedical applications. Further studies should evaluate their performance in biological systems, specifically their pharmacokinetics, biodistribution, and

potential for immune system activation. Moreover, conducting in vivo studies with animal models could provide critical data on MIPs' safety and efficacy, paving the way for clinical trials.

Overall, the findings highlight MIPs as a promising platform for creating synthetic antibodies with high specificity, efficacy, and stability. Unlike traditional biological antibodies, which may struggle with effectiveness, stability, and production speed as new virus variants emerge, MIPs offer significant advantages. Their flexibility and adaptability allow for rapid design and production, making them a valuable tool in addressing novel viral threats. The demonstrated stability and biocompatibility of MIPs further enhance their practical utility, positioning them as a reliable alternative to conventional antibodies in the ongoing fight against COVID-19 and future viral outbreaks.

Acknowledgements

O. I. P. and F. P. (Francesco Patitucci) were funded by PON ‘‘Ricerca e Innovazione’’ 2014–2020, Asse IV ‘‘Istruzione e ricerca per il recupero’’, Azione IV.4—‘‘Dottorati e contratti di ricerca su tematiche dell'innovazione’’.

M. D. was funded by the National Plan for NRRP Complementary Investments (PNC, established with the decree-law 6 May 2021, n. 59, converted by law n. 101 of 2021) in the call for the funding of Research Initiatives for Technologies and Innovative Trajectories in the Health and Care Sectors (Directorial Decree n. 931 of 6 June 2022)—project n. PNC0000003—AdvaNced Technologies for Human-centrEd Medicine (project acronym: ANTHEM).

REFERENCES

[1] A. Bajaj, J. Trimpert, I. Abdulhalim, Z. Altintas, Synthesis of molecularly imprinted polymer nanoparticles for SARS-CoV-2 virus detection using surface plasmon resonance, Chemosensors 10 (2022) 459.

[2] T.S. Bedwell, M.J. Whitcombe, Analytical applications of MIPs in diagnostic assays: future perspectives, Anal. Bioanal. Chem. 408 (2016) 1735–1751.

[3] C. Contardi, D. Rubes, M. Serra, R. Dorati, M. Dattilo, L. Mavliutova, M. Patrini, R. Guglielmann, Br Sellergren, E. De Lorenzi, Affinity Capillary Electrophoresis as a Tool To Characterize Molecularly Imprinted Nanogels in Solution, Anal. Chem. 96 (2024) 3017–3024.

[4] M. Dattilo, M.F. Motta, F. Patitucci, C. Ferraro, O.I. Parisi, F. Puoci, Exploring Crosslinker Effects on Fluorescent Molecularly Imprinted Polymers for Improved Gefitinib Delivery in Lung Cancer Theranostics, Mater. Adv. (2024).

[5] R.M. Derbali, V. Aoun, G. Moussa, G. Frei, S.F. Tehrani, J.C. Del'Orto, P. Hildgen, V.G. Roullin, J.L. Chain, Tailored nanocarriers for the pulmonary delivery of levofloxacin against Pseudomonas aeruginosa: a comparative study, Mol. Pharm. 16 (2019) 1906–1916.

[6] E.A. Dubiel, B. Martin, S. Vigier, P. Vermette, Real-time label-free detection and kinetic analysis of Etanercept—Protein A interactions using quartz crystal microbalance, Colloids Surf. B: Biointerfaces 149 (2017) 312–321.

[7] J. García-Calz´on, M. Díaz-García, Characterization of binding sites in molecularly imprinted polymers, Sens. Actuators B: Chem. 123 (2007) 1180–1194.

[8] M. Garg, N. Pamme, Strategies to remove templates from molecularly imprinted polymer (MIP) for biosensors, TrAC Trends Anal. Chem. (2023) 117437.

[9] K. Haupt, P.X. Medina Rangel, B.T.S. Bui, Molecularly imprinted polymers: Antibody mimics for bioimaging and therapy, Chem. Rev. 120 (2020) 9554–9582.

[10] C. Herrera Le´on, N.A. Kalacas, A. Mier, P. Sakhaii, F. Merlier, E. Prost, I. Maffucci, V. Montagna, H. Mora-Rad´o, P.K. Dhal, Synthetic Peptide Antibodies as TNF-α Inhibitors: Molecularly Imprinted Polymer Nanogels Neutralize the Inflammatory Activity of TNF-α in THP-1 Derived Macrophages, Angew. Chem. 135 (2023) e202306274.

[11] C.B. Jackson, M. Farzan, B. Chen, H. Choe, Mechanisms of SARS-CoV-2 entry into cells, Nat. Rev. Mol. Cell Biol. 23 (2022) 3–20.

[12] J. Jiang, G. Oberd¨orster, P. Biswas, Characterization of size, surface charge, and agglomeration state of nanoparticle dispersions for toxicological studies, J. Nanopart. Res. 11 (2009) 77–89.

[13] R. Khandia, S. Singhal, T. Alqahtani, M.A. Kamal, A. Nahed, F. Nainu, P.A. Desingu, K. Dhama, Emergence of SARS-CoV-2 Omicron (B. 1.1. 529) variant, salient features, high global health concerns and strategies to counter it amid ongoing COVID-19 pandemic, Environ. Res. 209 (2022) 112816.

[14] N.D. Kushwaha, J. Mohan, B. Kushwaha, T. Ghazi, J.C. Nwabuife, N. Koorbanally, A.A. Chuturgoon, A comprehensive review on the global efforts on vaccines and repurposed drugs for combating COVID-19, Eur. J. Med. Chem. (2023) 115719.

[15] A. Lamaoui, A.A. Lahcen, A. Amine, Unlocking the Potential of Molecularly Imprinted Polydopamine in Sensing Applications, Polymers 15 (2023) 3712.

[16] Z.Q. Liu, X. Yang, Q. Zhang, TURBISCAN: history, development, application to colloids and dispersions, Adv. Mater. Res. 936 (2014) 1592–1596.

[17] R. Malivindi, F. Patitucci, S. Prete, M. Dattilo, A.E. Leonetti, N. Scigliano, O. I. Parisi, F. Puoci, Efficacy and safety assessment of PIMIN050 raft-forming system as medical device based on Citrus sinensis and Crassostrea gigas for the management of gastroesophageal reflux disease, J. Drug Deliv. Sci. Technol. 78 (2022) 103986.

[18] S. Moneshwaran, D. Macrin, N. Kanagathara, An unprecedented global challenge, emerging trends and innovations in the fight against COVID-19: A comprehensive review, Int. J. Biol. Macromol. (2024) 131324.

[19] G.M. Morris, R. Huey, W. Lindstrom, M.F. Sanner, R.K. Belew, D.S. Goodsell, A. J. Olson, AutoDock4 and AutoDockTools4: Automated docking with selective receptor flexibility, J. Comput. Chem. 30 (2009) 2785–2791.

[20] M.S. Muthu, S.-S. Feng, Pharmaceutical stability aspects of nanomedicines, Nanomedicine 4 (2009) 857–860.

[21] O.I. Parisi, M. Dattilo, F. Patitucci, R. Malivindi, S. Delbue, P. Ferrante, S. Parapini, R. Galeazzi, M. Cavarelli, F. Cilurzo, Design and development of plastic antibodies against SARS-CoV-2 RBD based on molecularly imprinted polymers that inhibit in vitro virus infection, Nanoscale 13 (2021) 16885–16899.

[22] O.I. Parisi, F. Francomano, M. Dattilo, F. Patitucci, S. Prete, F. Amone, F. Puoci, The evolution of molecular recognition: From antibodies to molecularly imprinted polymers (MIPs) as artificial counterpart, J. Funct. Biomater. 13 (2022) 12.

[23] E.F. Pettersen, T.D. Goddard, C.C. Huang, G.S. Couch, D.M. Greenblatt, E.C. Meng, T.E. Ferrin, UCSF Chimera—a visualization system for exploratory research and analysis, J. Comput. Chem. 25 (2004) 1605–1612.

[24] A. Raziq, A. Kidakova, R. Boroznjak, J. Reut, A. ¨Opik, V. Syritski, Development of a portable MIP-based electrochemical sensor for detection of SARS-CoV-2 antigen, Biosens. Bioelectron. 178 (2021) 113029.

[25] S.H. Shahcheraghi, J. Ayatollahi, A.A. Aljabali, M.D. Shastri, S.D. Shukla, D. K. Chellappan, N.K. Jha, K. Anand, N.K. Katari, M. Mehta, An overview of vaccine development for COVID-19, Ther. Deliv. 12 (2021) 235–244.

[26] A.N. Stephen, S.R. Dennison, M. Holden, S.M. Reddy, Rapid sub-nanomolar protein determination in serum using electropolymerized molecularly imprinted polymers (E-MIPs), Analyst 148 (2023) 5476–5485.

[27] C. Tian, K. Kasavajhala, K.A. Belfon, L. Raguette, H. Huang, A.N. Migues, J. Bickel, Y. Wang, J. Pincay, Q. Wu, ff19SB: amino-acid-specific protein backbone parameters trained against quantum mechanics energy surfaces in solution, J. Chem. Theory Comput. 16 (2019) 528–552.

[28] S.S. Toussi, J.L. Hammond, B.S. Gerstenberger, A.S. Anderson, Therapeutics for COVID-19, Nat. Microbiol. 8 (2023) 771–786.

[29] W.H.O. WHO, Classif. omicron (B. 1. 1. 529): SARS-CoV-2 Var. Concern. (2021).

[30] W.H.O. WHO, Corona Dis. (COVID-19) Epidemiol. Updates Mon. Oper. Updates (2024).

[31] J. Zhou, L. Wang, X. Liu, Y. Gai, M. Dong, C. Wang, M.M. Ali, M. Ye, X. Yu, L. Hu, Glycan-Imprinted Nanoparticle as Artificial Neutralizing Antibody for Efficient HIV-1 Recognition and Inhibition, Nano Lett. 24 (2024) 4423–4432.

Supplementary Material

Molecularly Imprinted Polymers (MIPs) for SARS-CoV-2 Omicron variant inhibition: an alternative approach to address the challenge of emerging zoonoses

Marco Dattilo, Francesco Patitucci, Marisa Francesca Motta, Sabrina Prete, Roberta Galeazzi, Silvia Franzè, Ida Perrotta, Mariangela Caravelli, Ortensia Ilaria Parisi*, Francesco Puoci

DOCKING STUDIES RESULTS ON NIPAM, nPMA, TBAm MONOMERS

NIPAM docking results

NIPAM monomer cluster analysis results in the identification of only two clusters, with the first one being most populated (Cl1 88%). Both are located far from the RBM and thus it cannot be considered adequate for polymer imprinting; eventually it can be considered as linker due to its specificity of binding in one single RBD region (Figure 1S).

nPMA docking results

As already noticed for NIPAM, also nPMA shows cluster population only far from RBM, with three main populated clusters (overall seven) Cl1(15%), Cl2 (18%), and Cl7 (37%). All are located in the lateral faces of RBD, making this monomer not adequate for polymer imprinting (Figure 1S).

TBAm docking results

For this monomer, the lowest energy and most populated clusters (Cl1 60% and Cl2 22 %, Cl3 8%) are located in a RBD portion already observed for NIPAM, and far from RBM. Here, we can point out the presence of Cl4 (6%) located close to the RBM. Thus, this monomer appears potentially suitable for polymer imprinting, even if it would be best used in combination with other monomers, whose lowest energy poses are identified near the RBM (i.e acrylamide or acrylic acid).

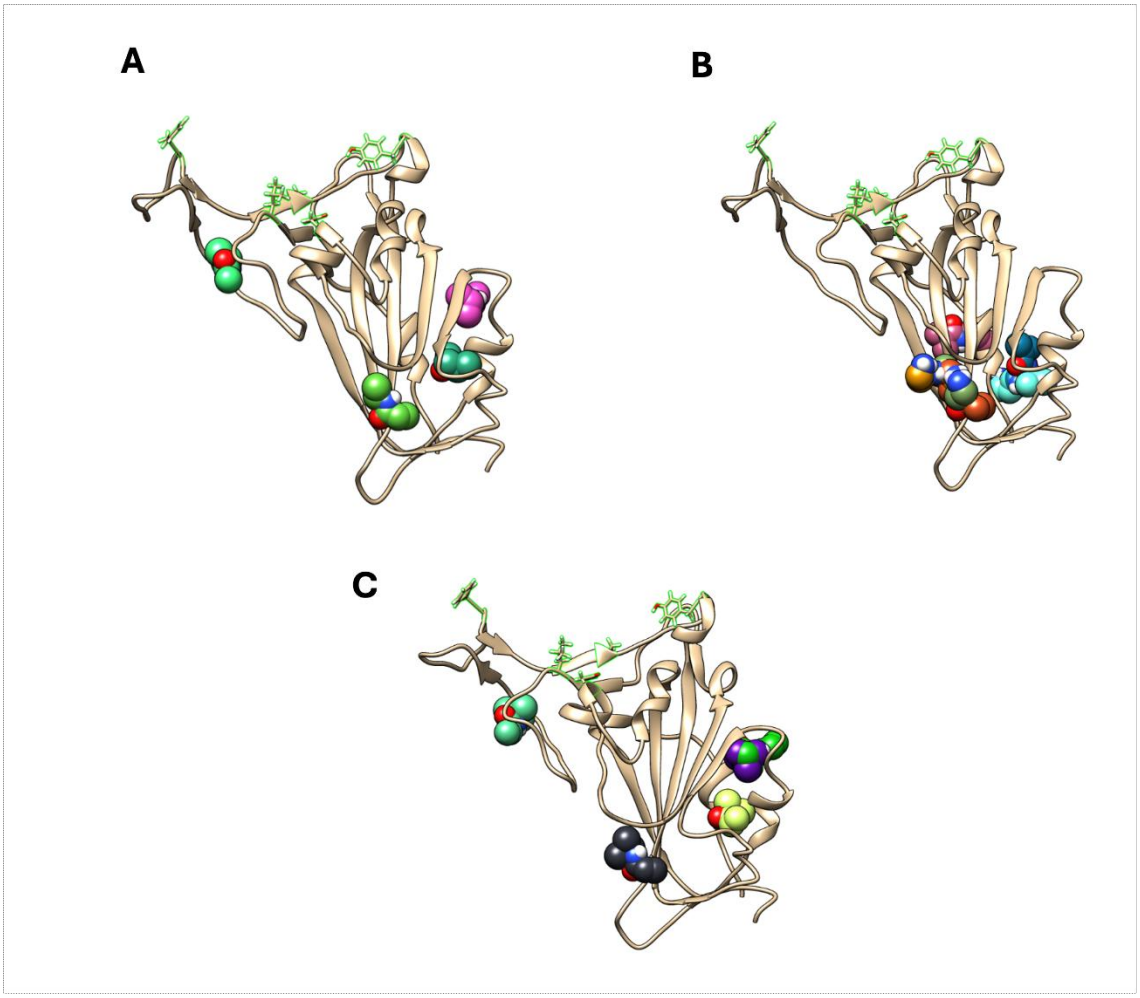

Fig. 1S. (A) NIPAM (CPK spheres) distributions accessible to solvent surface on RBD domain of spike protein (gold ribbons). In green are highlighted the 6 key residues implicated in ACE2 binding (resuled 417,455, 486 493,494, 501). (B) nPAM (CPK spheres) distributions accessible to solvent surface on RBD domain of spike protein (gold ribbons). In green are highlighted the 6 key residues implicated in ACE2 binding (resuled 417,455, 486 493,494, 501). (C) TBAm (CPK spheres) distributions accessible to solvent surface on RBD domain of spike protein (gold ribbons). In green are highlighted the 6 key residues implicated in ACE2 binding (resuled 417,455, 486 493,494, 501).

TEMPLATE REMOVAL

Cleaning trials were conducted under acidic (6M HCl) and alkaline (4M NaOH) conditions, at both room temperature and 50°C, using BSA as model protein to determine the most effective method and evaluate the polymer's response (Hou et al., 2022). The results are shown in Figure 2S.

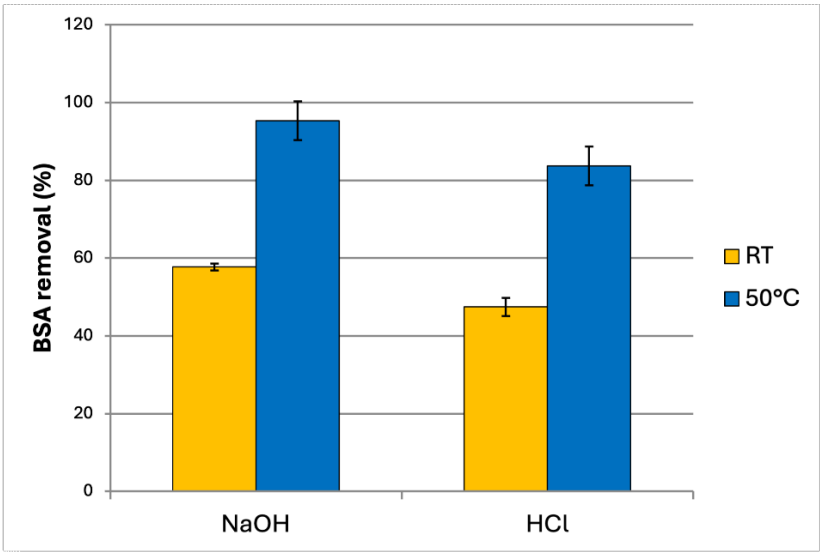

Fig. 2S. BSA removal (%) under alkaline (NaOH) and acidic (HCl) conditions at two different temperatures: room temperature (RT) and 50°C.

Spectrophotometric analysis of BSA content within dialysis membranes indicated a decrease in protein concentration relative to the initial amount. Among the tested hydrolysis conditions, the alkaline condition demonstrated greater efficacy, achieving BSA removal exceeding 90%. Additionally, of the two tested temperatures, heating at 50°C was the most effective, yielding greater hydrolysis and significant removal of the template protein. These results highlight that basic hydrolysis at elevated temperature is the optimal combination for template removal from the imprinted polymer.

Simultaneously, similar tests were conducted on MIP and NIP samples to evaluate their stability under hydrolysis conditions. The results are shown in Figure 3S.

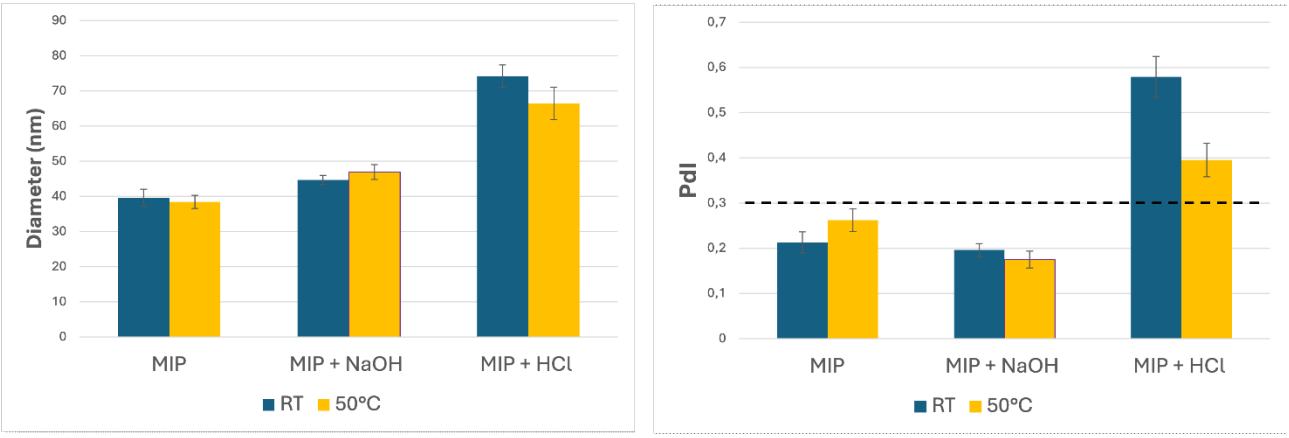

Fig. 3S. Z-Average size and PdI of MIP particles under different hydrolysis conditions. Dashed lines indicate the accepted thresholds for PDI (< 0.3) (Danaei et al., 2018). Data are expressed as mean ± SD (n=3).

DLS analysis revealed that acid hydrolysis led to a significant increase in size and PdI, likely due to the presence of H+ and Cl- ions in solution creating an osmotic effect, drawing water into the particles and causing expansion. Furthermore, interactions of H+ ions with gel functional groups and potential breaking of weak bonds could contribute to this effect. Consequently, consistent with previous results, alkaline hydrolysis proved the best choice for template removal. Regarding the different temperatures, the polymer's stability varied minimally between tested conditions. However, the 50°C method was chosen for its superior efficacy in BSA removal.

STABILITY STUDIES

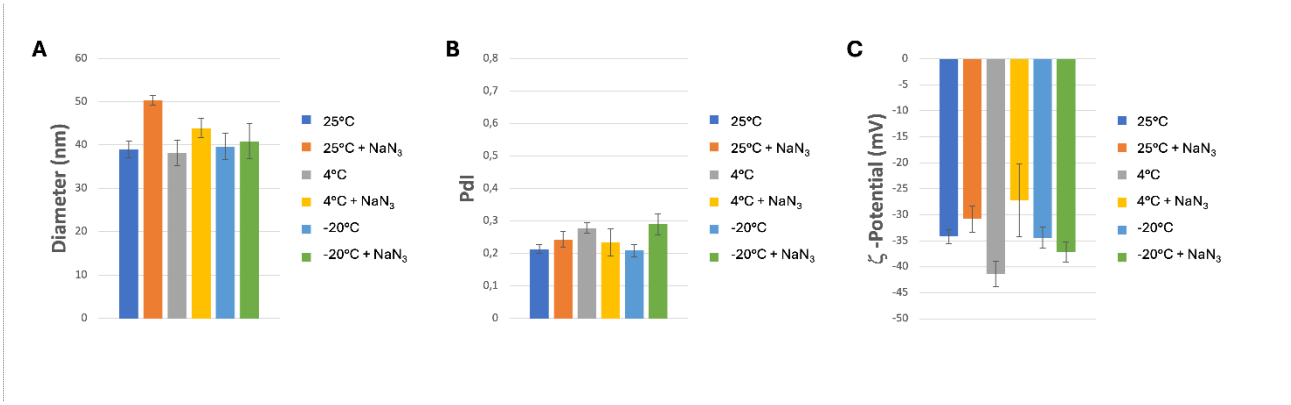

Fig. 4S. Stability tests of MIP nanoparticles under different storage conditions after one day from synthesis: (A) mean diameter, (B) polidispersity index and (C) ζ-potential. Data are expressed as mean ± SD (n=3).

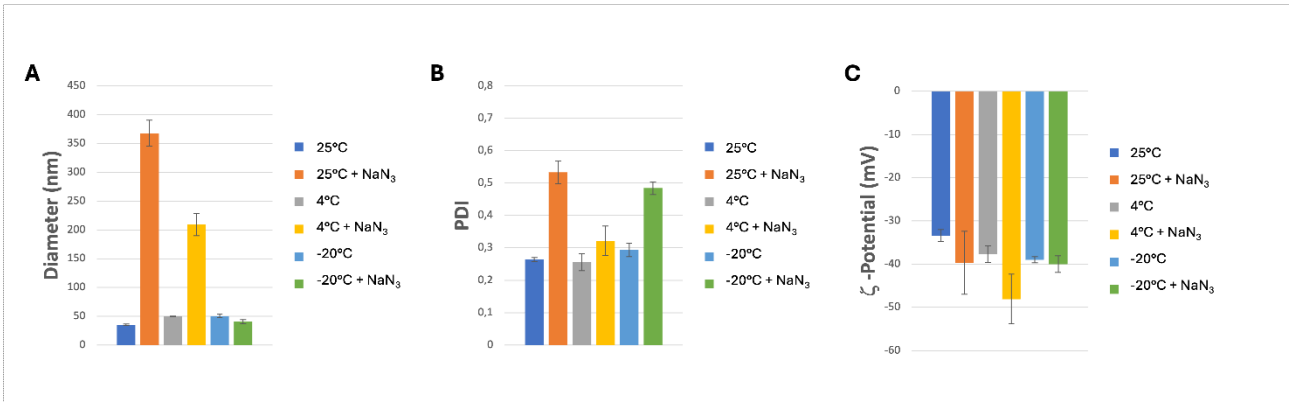

Fig. 5S. Stability tests of MIP nanoparticles under different storage conditions after 30 days from synthesis: (A) mean diameter, (B) polidsipersity index and (C) ζ-potential. Data are expressed as mean ± SD (n=3).

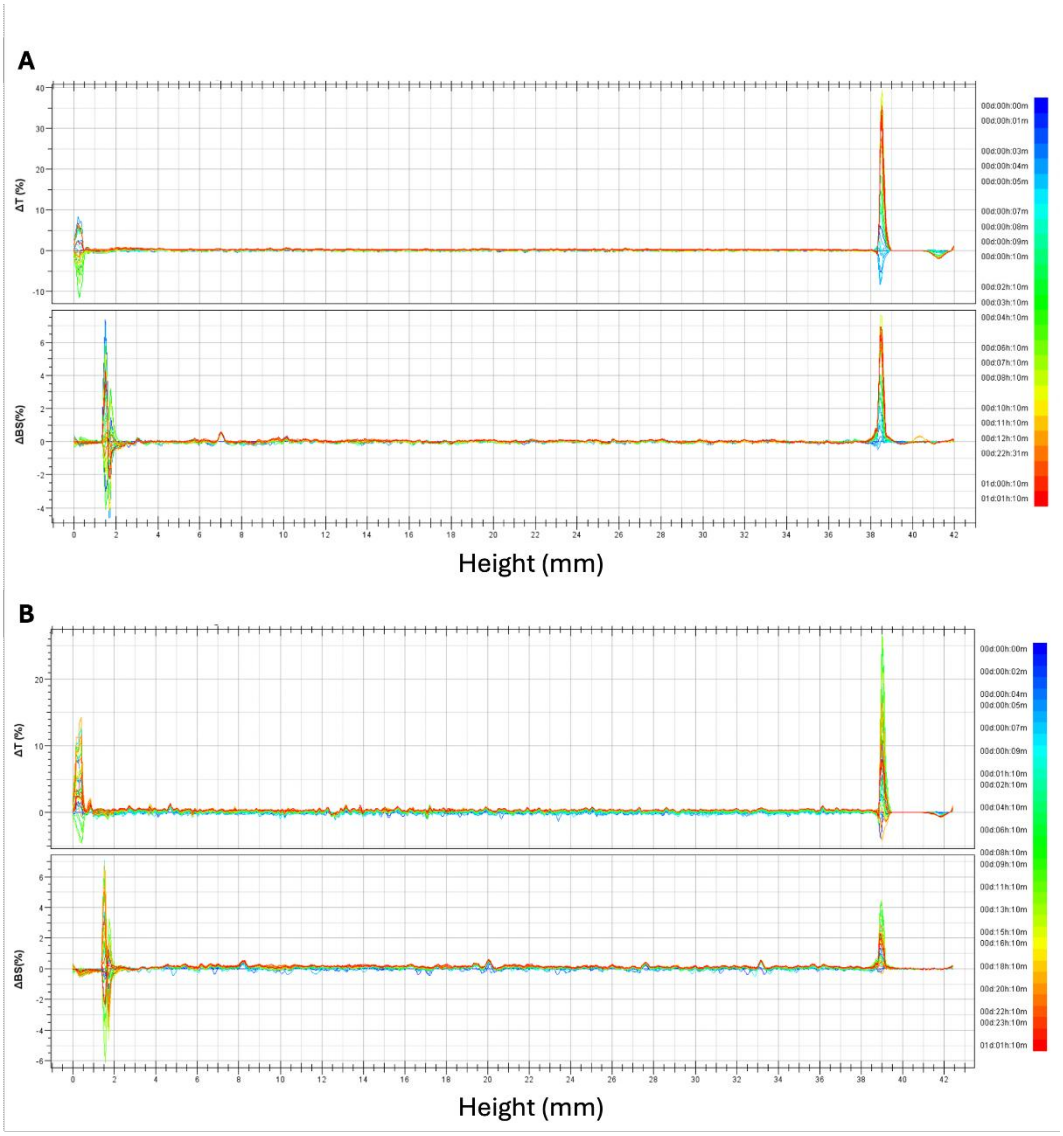

Fig. 6S. Transmission intensity (ΔT%) and backscattering (ΔBS%) profiles of imprinted nanoparticles in distilled water (A) and PBS (B) in function of time after one day from synthesis.

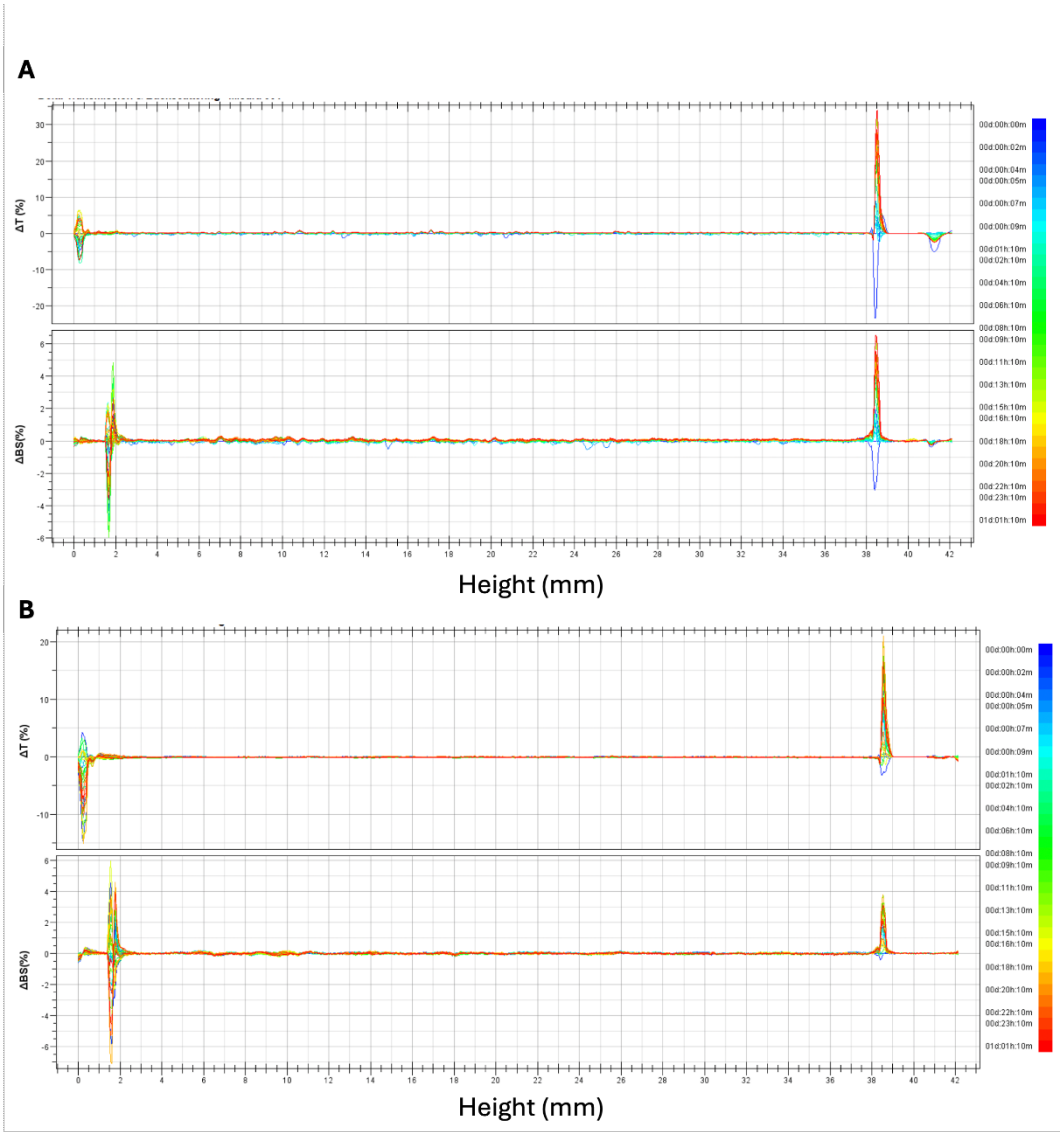

Fig. 7S. Transmission intensity (ΔT%) and backscattering (ΔBS%) profiles of imprinted nanoparticles in distilled water (A) and PBS (B) in function of time after 30 days from synthesis.

REFERENCES

Hou, Yongqing, et al. "Protein hydrolysates in animal nutrition: Industrial production, bioactive peptides, and functional significance." Bioactive Peptides from Food (2022): 209-232.

III

Biopolymeric Nanoparticles as MIPs for Zika Virus Recognition

Francesco Patitucci [a], Carla Orlando [b,c], Marisa Francesca Motta [a], Marco Dattilo [a], Federica Arrigoni [b], Rocco Malivindi [a,d], Ortensia Ilaria Parisi [a,d], Francesco Puoci [a,d]

[a] Department of Pharmacy, Health and Nutritional Sciences, University of Calabria, Rende, CS 87036, Italy

[b] Department of Biotechnology and Biosciences, University of Milano-Bicocca, Milan, 20126, Italy

[c] Department of Chemistry and Chemical Technologies, Università della Calabria, Rende, CS 87036, Italy

[d] Macrofarm s.r.l., c/o Department of Pharmacy, Health and Nutritional Sciences, University of Calabria, Rende, CS 87036, Italy

ABSTRACT

This study introduces molecularly imprinted polysaccharide-based nanoparticles (MIPs) as innovative synthetic platforms for precise molecular recognition, specifically designed to target the Zika virus envelope protein (ZIKV-E). Biocompatible and biodegradable sodium alginate and chitosan were strategically chosen as base materials, undergoing controlled depolymerization with hydrogen peroxide to achieve optimal molecular weight and enhanced solubility. Advanced formulation and process optimization resulted in nanoparticles with exceptional stability, uniform size distribution, and high reproducibility.

The synthesized nanoparticles demonstrated robust stability, as confirmed by stable TSI values, ensuring their viability for long-term storage and scalable production. Binding isotherms and Quartz Crystal Microbalance with Dissipation monitoring (QCM-D) revealed the superior binding capacity and specificity of MIPs for ZIKV-E compared to non-imprinted polymers (NIPs). Furthermore, in vitro evaluations, including cell viability assays and the human Cell Line Activation Test (h-CLAT), validated their excellent biocompatibility and absence of sensitizing effects, confirming their suitability for biomedical applications.

These findings position molecularly imprinted polysaccharide nanoparticles as a highly promising and versatile platform for combating Zika virus infections, with the potential to address a broader spectrum of emerging viral threats, paving the way for future advancements in targeted therapeutic solutions.

INTRODUCTION

Zika virus (ZIKV), a member of the Flaviviridae family, emerged as a significant global health concern and became the first major infectious disease in over half a century to be linked to human birth defects.[1,2] First isolated in 1947, with initial human infections documented in 1964, ZIKV remained relatively obscure until a major outbreak in 2007 in the Federated States of Micronesia affected over 70% of Yap's population.[3] The virus gained widespread attention following its introduction to the Americas in 2015, starting in Brazil and rapidly spreading to at least 33 countries and territories by March 2016.[1,4] ZIKV is primarily transmitted through Aedes mosquitoes, particularly A. aegypti and A. albopictus, in a human-mosquito-human transmission cycle, but uniquely among flaviviruses, it can also spread through sexual contact, blood transfusions, and vertical transmission from mother to fetus.[5] The virus is structurally characterized as an enveloped icosahedral particle containing a positive single-stranded RNA genome of approximately 11 kb, which encodes three structural proteins (capsid, pre-membrane, and envelope) and seven non-structural proteins.[6,7] The envelope (E) protein, particularly its glycosylation at N154, plays a crucial role in viral entry and pathogenesis, facilitating attachment to host cells through various receptors, including DC-SIGN, L-SIGN, and phosphatidylserine receptors.[8,9] ZIKV infection typically manifests with mild symptoms lasting 2-7 days, including fever, maculopapular rash, arthralgia, and conjunctivitis, but its ability to cause severe neurological complications, particularly microcephaly in developing fetuses and Guillain-Barré syndrome in adults, has raised significant public health concerns.[5,10] The virus demonstrates notable cellular tropism, targeting various cell types including skin cells, monocytes, and neural cells, with cellular entry occurring through clathrin-mediated endocytosis.[7,11] Despite its significant impact on global health, particularly during the 2015-2016 outbreak in Brazil that led to thousands of cases of microcephaly, no specific antiviral treatment currently exists, and management remains largely supportive.[12] The

development of effective therapeutic strategies is complicated by ZIKV's structural and immunological similarities to other flaviviruses, particularly dengue virus, which raises concerns about antibody-dependent enhancement in areas where both viruses circulate.[13,14] This unprecedented combination of transmission routes, severe neurological complications, and lack of specific treatment options highlights the critical need for continued research into ZIKV pathogenesis and the development of targeted therapeutics and vaccines.

In this context, Molecularly Imprinted Polymers (MIPs) offer a groundbreaking approach that has gained significant recognition for their ability to create highly specific synthetic recognition elements.

Molecular Imprinting Technology (MIT) is an innovative technology that allows the synthesis of polymer matrices with specific molecular recognition capabilities, designed to selectively interact with a target molecule. This process involves the copolymerization of functional monomers and cross-linkers in the presence of a template molecule, which serves as a model for the formation of specific binding sites. Once the template molecule is removed, the resulting polymer matrix contains cavities complementary in shape, size, and chemical functionality to the target, enabling selective recognition with affinity comparable to that of antibodies.[15,16]

This technology finds applications in various fields, including the development of chemical sensors, substance separation, biomolecule purification, and even targeted drug therapy. Molecular imprinting stands out for its flexibility in adapting to a wide range of target molecules, from small drugs to viruses, and represents a powerful tool for creating highly efficient synthetic receptors.[17–19]

In particular, MIT has proven particularly promising for detecting the Zika virus (ZIKV). MIPs have been developed to detect ZIKV with high sensitivity and selectivity. A notable example includes electrochemical biosensors employing graphene oxide composites and imprinted surface polymers, which have demonstrated exceptional sensitivity to the virus and suitability for early-

stage diagnostics.[20] Another approach utilizes self-assembled monolayers (SAMs) on gold-coated chips to generate imprinted matrices, enabling detection even in biological samples such as human saliva. The integration of these devices into point-of-care (POC) diagnostics highlights their ability to provide rapid and accurate screening for ZIKV.[21] Furthermore, the use of 3D substrates and gold-sulfur covalent bonds has facilitated the design of high-selectivity “lock-and-key” complexes, distinguishing ZIKV from similar viruses like dengue (DENV), both in buffer solutions and biological matrices.[22]

Here, we developed an advanced synthesis protocol for molecularly imprinted polysaccharide-based nanoparticles, significantly enhancing their stability, size control, and distribution. Through careful optimization of formulation and process conditions, we achieved nanoparticles that are both uniform and highly reproducible. Polysaccharide materials like sodium alginate and chitosan are increasingly favoured in protein delivery due to their biocompatibility, biodegradability, and versatility in design.[23–25] These nanoparticles effectively encapsulate drugs, genes, and hydrophobic substances, improving both their bioavailability and chemical stability.[26] Notable formulations, such as drug-loaded alginate nanocapsules and chitosan-based nanoparticles, have shown promising results in applications ranging from antimicrobial to anticancer treatments.[27] Chitosan-alginate nanoparticles, in particular, exhibit high encapsulation efficiency and hold significant potential for the oral delivery of protein-based drugs, offering a highly versatile and effective approach for targeted therapeutic applications.[28–30]

However, despite their advantages, challenges persist in the use of these polysaccharides, particularly in achieving nanoparticles with uniform size and proper dispersion. To overcome this, alginate and chitosan can undergo depolymerization through chemical, enzymatic, or oxidative methods, with acid hydrolysis and oxidative degradation being the most commonly used techniques.[31,32] For instance, hydrogen peroxide effectively reduces the molecular weight of alginate, producing oligosaccharides.[33–35] Similar methods are applied to chitosan, where acid

hydrolysis or oxidative degradation with hydrogen peroxide breaks it into smaller fragments.[34,35] These depolymerization processes yield oligosaccharides with various biological activities, such as antioxidant, anti-inflammatory, and antimicrobial properties, with lower molecular weight derivatives showing improved solubility and bioactivity.[36–41]

To demonstrate the versatility of our approach, we used the envelope protein of the Zika virus (ZIKV-E) as the template molecule, addressing the ongoing need for effective tools against emerging viral infections. A variety of experimental techniques were employed to evaluate the physicochemical properties, binding performance and biocompatibility of the synthesized MIPs.

EXPERIMENTAL SECTION

Reagents

The Zika virus Envelope protein (His Tag) was purchased from Sino Biological Inc. (Beijing, China). Sodium Alginate, Chitosan, Calcium Chloride, Sodium Tripolyphosphate, Span-80, Seed oil, Disodium Hydrogen Phosphate, Sodium Dihydrogen Phosphate, Human Serum Albumin (HSA), 3-Sulfo-N-Hydroxysuccinimide (Sulfo-NHS), 1-ethyl-3-(3-dimethylaminopropyl)carbodiimide (EDC), 16-Mercaptohexadecanoic acid (MHA), 11-Mercapto-1-undecanol (MU), Dulbecco's Modified Eagle Medium (DMEM), Penicillin/Streptomycin, β-Mercaptoethanol, Fetal Bovine Serum (FBS), Bovine Calf Serum (BCS), Neutral Red (NRU), Nickel Sulfate (Product No. 1.06726), Propidium Iodide, FACS buffer (PBS, 0.5–1 % BSA or 5–10 % FBS, 0.1 % sodium azide), Sodium Azide, Bovine Serum Albumin (BSA), and γ-globulin were purchased from Sigma-Aldrich s.r.l. (Milan, Italy). RPMI 1640 medium was obtained from ATCC (Manassas, VA, USA). All solvents were of reagent or HPLC grade and obtained from VWR (Milan, Italy). 5 MHz Au-coated QCM sensors were obtained from Novaetech S.r. l. (Italy).

Cell cultures

BALB/3T3 cells were purchased from the American Type Culture Collection (ATCC, Manassas, VA, USA) and maintained in DMEM medium (containing 2 mM L-glutamine, 1 % penicillin-streptomycin, and 1 % sodium pyruvate 1 mM) supplemented with 10 % bovine calf serum (BCS) at 37◦C in a humidified atmosphere consisting of 5 % CO2 in air.

THP-1 cells were purchased from the American Type Culture Collection (ATCC, Manassas, VA, USA) and cultured in RPMI 1640 medium supplemented with 10 % FBS, 1 %

Penicillin/Streptomycin, and 0.05 mM β-Mercaptoethanol at 37◦C in a humidified atmosphere consisting of 5 % CO_2 in air.

Depolymerization of Sodium Alginate and Chitosan

For the preparation of depolymerized polymers, a protocol was adapted with appropriate modifications. A 2% (w/v) solution of Sodium Alginate was prepared by dissolving the polymer in double-distilled water (ddH_2O) under magnetic stirring. Once fully solubilized, Hydrogen Peroxide (H_2O_2) was added at a 2:1 (w/w) ratio relative to the Alginate. Depolymerization was carried out at 80°C for 3 hours under continuous agitation at 1000 rpm. The depolymerized Alginate was recovered through ethanol-induced precipitation and collected by centrifugation at 5000 rpm.

A similar procedure was applied to Chitosan, with the exception that precipitation was achieved using a mixture of ethanol and 1 M NaOH in a 95:5 (v/v) ratio.

To analyze the molecular weight distribution of the depolymerized products, dialysis was performed using membranes with different Molecular Weight Cut-Offs (MWCOs). The polymer solutions were dialyzed against either ddH_2O or 1% (v/v) Acetic Acid using dialysis tubes with MWCOs of 3.5 kDa and 12–14 kDa.

To further evaluate the reduction in polymer chain length, viscosity measurements were conducted. The viscosity of 2.5% (w/v) polymer solutions was measured before and after the depolymerization process, as well as before and after the dialysis steps. A Brookfield viscometer (PCE-RVI 4, PCE Instruments, Manchester, UK) was used for these measurements, employing 20 mL samples at room temperature. The results were expressed in milliPascal second (mPa·s).

Design of the Experimental Approach

To refine the synthesis protocol for alginate-chitosan nanoparticles, experiments were conducted both in the presence and absence of a model protein, bovine serum albumin (BSA), using polymer fractions with varying molecular weight distributions obtained through depolymerization, as depicted in Table 1. Additionally, non-depolymerized polymers were included as comparative controls to assess the impact of the depolymerization process on nanoparticle formation. The synthesis process followed is detailed in the subsequent section.

Sample	NPs_1	NPs_2	NPs_3	NPs_4
NDSA	0.5% (w/v)			
DSA > 12 kDa		0.5% (w/v)		
3,5 kDa < DSA < 12 kDa			0.5% (w/v)	
DSA < 3,5 kDa				0.5% (w/v)
NDC	0.5% (w/v)			
DC > 12 kDa		0.5% (w/v)		
3,5 kDa < DC < 12 kDa			0.5% (w/v)	
DC < 3,5 kDa				0.5% (w/v)

Table1. Experimental design summarizing the use of depolymerized Sodium Alginate (DSA) and depolymerized Chitosan (DC) fractions with defined molecular weight ranges. Non-depolymerized Sodium Alginate (NDSA) and non-depolymerized Chitosan (NDC) were used as controls.

The produced nanoparticles were characterized in terms of size, polydispersity index (PDI), and binding efficiency.

The particle size and polydispersity index (PDI) of produced nanoparticles were measured using Dynamic Light Scattering (DLS) with a Zetasizer Nano ZS (Malvern Instruments Ltd., UK), operating at 25°C with a red light laser (λ = 633 nm) and backscatter detection at 173°. The hydrodynamic diameters were calculated using the Stokes-Einstein equation and the viscosity and

refractive index of pure water as constants, while the PDI, evaluated to ensure a monodisperse population, was determined by fitting the autocorrelation function generated from intensity fluctuations of the scattered light.

Binding efficiency was determined by incubating a fixed concentration of nanoparticles (0.1 mg/mL) with a known amount of template (10 μg/mL) for 2 hours. After incubation, the template-nanoparticle complexes were separated via centrifugation at 13,000 rpm, and the unbound template in the supernatant was measured using a BCA protein assay kit. The BCA Protein Assay Kit (Pierce, Bonn, Germany) was utilized according to the manufacturer's guidelines: 25 μL of the sample was combined with 200 μL of the BCA working reagent, and the mixture was incubated at 37°C for 30 minutes. Absorbance was then measured at 562 nm. To ensure the accuracy and reproducibility of the results across different experiments, a standard BSA dilution curve, ranging from 0 to 2000 μg/mL, was included in each microplate assay. The final binding efficiency was calculated based on the amount of template bound to the nanoparticles, as determined from the absorbance measurements.

Computational methods and analysis

Molecular docking

The envelope Zika virus protein coordinates were obtained from the X-ray structure ID: 5JHM.[42]

In the case of the studied polymer (Chitosan and Sodium Alginate fragments), a representative model was adopted, 6 chains, considering 4 monomers for each chain that compose the substrate. Several types of complexes were evaluated, with different percentages of Chitosan (CHT) and Alginate (ALG) as shown in Table 2.

Sample	Ratio	ALG	CHT
Mix_1	100:0	100	0
Mix_2	67:33	67	33
Mix_3	50:50	50	50
Mix_4	33:67	33	67
Mix_5	0:100	0	100

Table 2. Different ratio of Alginate and Chitosan for computational analysis

Molecular docking was performed using Autodock Vina [43], in the proximity of the fusion loop (R98-K109). We evaluated the reliability of the docking protocol by performing molecular recognition of known ligands, such as the flavivirus broadly protective antibody.[42] At this point, each representative structure was prepared by assigning atom types and adding Gasteiger charges. The docking area was established using AutoGrid. A size of 45 × 45 × 45 Å was chosen for each fragment and the grid was centred on the Nitrogen of the side chain of Tryptophan 101. Lamarckian Genetic Algorithm (LGA) was used for the conformational search of the substrate, to allow for a sampling of the peptides' conformational space within the protein pocket. Docking simulations of ligands were performed, with a population size of 150, random initial position and conformation, local search rate of 0.6, and 2,500,000 energy evaluations. The final docked poses were clustered using an RMSD tolerance of 2 Å.

To obtain a more accurate estimate of the binding affinity to the ligand, Molecular Mechanics Poisson-Boltzmann Surface Area (MMPBSA) analysis was performed using the AmberTools code23.[44]

Finally, for the best-docked pose, in all systems with different ratios of the two polymers (67:33, 50:50 and 33:67), the stability of the polymers in the fusion loop was evaluated using molecular dynamics (MD) simulations of 200 ns in triplicate.

Molecular dynamics

MD was performed with the GROMACS 2020 package.[45] A combination of SB14ff/GAFF2 force field and TIP3P water model was used for the simulations, protein was placed in a 10 Å cubic box from the protein, containing the water molecules buffer and with counter-ions to make the total charge zero.[46,47] Starting from 3D protein model, classical MDs were performed on protein in apo-form and complexes.

The solvated systems were first minimized and relaxed by applying positional harmonic constraints on all atoms (50 kcal mol−1 Å2) using 5000 steps of steepest descent (SD), followed by 5000 steps of conjugate gradient (CG). In the second minimization step, the entire system was released unconstrained. Then, progressive heating was performed up to 300 K for 50 ps, followed by 10 ns at 300 K using a Langevin thermostat in the NVT ensemble. The system was also maintained at a constant pressure using an NPT ensemble at 1 bar pressure using the Berendsen barostat with a time constant τp = 2.0 ps. The production phase was performed for 200 ns of MDs selecting an integration step of 2 fs, the SHAKE algorithm coupling.

Preparation of nanoparticles

An emulsification-gelation technique, with modifications, was employed to synthesize alginate-chitosan nanoparticles.[48,49] For the organic phase, 18.8 mL of seed oil containing 0.06% (v/v) of Span80 was prepared at room temperature. The aqueous phase was prepared by dropwise addition of 2 mL of a 2% (w/v) depolymerized Chitosan solution (in 1% (v/v) Acetic Acid, pH 5.4) into 2 mL of a 2% (w/v) depolymerized Alginate solution (pH 5.2) at a flow rate of 0.5 mL/min using a

syringe pump. The resulting mixture was magnetically stirred under vortex motion for 15 minutes to ensure uniformity.

The prepared aqueous phase was then added dropwise into the organic phase using the same syringe pump flow. The resulting emulsion was stirred continuously at room temperature for 30 minutes to achieve stable phase mixing.

Crosslinking was performed sequentially by adding 1.5 mL of a 2% (w/v) $CaCl_2$ aqueous solution, followed 15 minutes later by 1.5 mL of a 2% (w/v) TPP aqueous solution. Both solutions were introduced dropwise into the emulsion, while the mixture was stirred under vortex motion for an additional 30 minutes.

To obtain oil-free nanoparticles, the collected precipitate was rinsed three times with methanol containing 0.15% (v/v) glycerol, followed by centrifugation at 8000 rpm for 10 minutes. The resulting precipitate was thoroughly rinsed with ddH2O to remove residual alcohols.

Molecularly imprinted polymer (MIP) nanoparticles were prepared using similar steps, also incorporating 100 μg of template into the alginate solution. To remove residual template molecules from the MIPs, the prepared nanoparticles were putted in a dialysis bag (MWCO=100 kDa) and rinsed with 10 mM phosphate-buffered saline (PBS, pH 7.4) at room temperature for 3 days.

Characterization of nanoparticles

The particle size and polydispersity index (PDI) of the produced nanoparticles were measured as described above. In addition to size and PDI characterization, the stability of the samples was monitored for 24 hours after one day and again after 30 days post-synthesis using the Turbiscan® DNS™. Each 20 mL sample was placed in a cylindrical glass cell and maintained at 25°C during the analysis. The detection system, consisting of a pulsed near-infrared light source (880 nm) and transmission (T) and backscattering (BS) detectors, measured light passing through the sample at a

180° angle from the incident beam. The device scanned the entire 65 mm height of the sample cell, recording measurements every 40 μm, resulting in a total of 1625 acquisitions per scan.

Binding studies

Binding Efficiency Evaluation Using BCA Protein Assay

The binding experiments were conducted as described above, using a fixed amount of polymer (60 mg) and increasing concentrations of the template. To gain deeper insights into the adsorption properties of the synthesized MIP and NIP nanoparticles, the experimental binding data were subsequently analyzed using theoretical models.

Preparation of QCM Sensor and Detection of protein binding via QCM-D

For the preparation of the QCM-D sensor, a cleaned chip was placed in a petri dish and immersed in 4 mL of a thiol solution containing 1 mM 16-Mercaptohexadecanoic acid (MHA) and 1 mM 11-Mercapto-1-undecanol (MU), dissolved in a 90:10 ethanol-acetic acid mixture. This process was carried out in the dark at room temperature overnight, allowing the formation of a Self-Assembled Monolayer (SAM) on the gold surface to enhance subsequent binding interactions. After treatment, the chip was thoroughly washed with absolute ethanol and dried with nitrogen (N_2). To activate the carboxyl groups of MHA, a sulfo-NHS:EDC solution (1:1 ratio, 100 mg/mL in ddH_2O) was applied for 60 minutes, followed by rinsing with ddH_2O and drying with nitrogen.

For the immobilization of the Zika virus envelope protein (ZIKV-E), a standard solution was prepared at a concentration of 10 μg/mL in ddH_2O and injected into the QCM-D instrument to assess the amount of analyte bound to the sensor surface.

The binding interactions between the MIP and NIP with ZIKV-E were examined using varying nanoparticle concentrations (12.5, 25, 50, and 100 μg/mL). The QCM-D system was calibrated to a fundamental frequency of approximately 5 MHz. Baseline stabilization was achieved by introducing ddH_2O at a flow rate of 10 μL/min for one hour, ensuring that the frequency signal remained stable within ±0.5 Hz over a 10-minute period. After stabilization, the samples were introduced into the QCM-D instrument at the same flow rate for 50 minutes at each concentration. The system recorded the frequency shifts resulting from binding events between the nanoparticles and the analyte, providing insights into the binding affinity and kinetics. To verify the specificity of the MIP for detecting ZIKV-E, additional experiments were conducted by immobilizing Human Serum Albumin (HSA) on the QCM sensor chips. The binding interactions of MIP and NIP with these immobilized proteins were analyzed at the same nanoparticle concentrations.

Cytotoxicity evaluation

The cytotoxicity of the tested sample was evaluated using the Neutral Red Uptake (NRU) assay, in accordance with the ISO 10993-5:2009 guidelines, which provide methods for assessing the in vitro cytotoxicity of medical devices.[50] Balb/3T3 Clone A31 cells were plated at a density of 2.5×10^4 cells per well and exposed to varying concentrations of the tested sample (0.025 mg/mL, 0.0125 mg/mL, 0.00625 mg/mL, 0.00312 mg/mL, 0.0156 mg/mL, 0.00078 mg/mL) in DMEM for 24 hours at 37°C in a 5% CO_2 atmosphere. Following treatment, the cells were incubated with a 50 μg/mL Neutral Red (NR) solution for 3 hours. Afterward, the NR solution was removed, and the cells were subjected to an extraction process using a solvent mixture composed of ethanol, water, and acetic acid in a 50:49:1 ratio. Absorbance was measured at 540 nm using an Epoch microplate reader (BioTek, Winooski, VT, USA), and cell viability was reported as a percentage compared to the control cells, which were regarded as 100% viable.

Human Cell Line Activation Test (h-CLAT)

The Human Cell Line Activation Assay (h-CLAT) is employed to evaluate the potential of chemicals or mixtures to induce skin sensitization by activating the immune response. This assay adheres to the protocols outlined in the OECD 442E and EURL ECVAM guidelines.[51] The THP-1 human monocytic leukemia cell line is utilized for assessing the expression of key co-stimulatory molecules, including CD54 and CD86, which are indicative of immune system activation. Nickel sulfate ($NiSO_4$) is used as a positive control in this assay.

For the determination of the CV75 (the concentration that induces 25% cell mortality), the cells are seeded at a density of 1.5×10^5 cells per well in 96-well plates and incubated under standard conditions. Following treatment with the test substances, the cells are centrifuged to remove the medium. The remaining cells are resuspended in FACS buffer containing propidium iodide (PI), and CV75 is calculated through flow cytometry analysis to evaluate cell viability.

In the h-CLAT protocol, 5×10^5 cells are plated in 24-well plates and incubated for 24 hours. After the treatment period, the cells are further incubated for another 24 hours. Nickel sulfate (100 μg/mL) and culture medium are used as positive and negative controls, respectively. After incubation, the cells are subjected to centrifugation, resuspended in FACS buffer, and divided into three aliquots. These aliquots are treated with a blocking solution (FACS buffer containing 0.01% γ-globulin) for 15 minutes at 4°C. The cells are then exposed to fluorescein-conjugated antibodies targeting CD86, CD54, or IgG1 (control) for 30 minutes at 4°C. Following antibody incubation, the cells are washed to remove any unbound antibodies, resuspended in FACS buffer containing PI, and analyzed by flow cytometry.

RESULTS AND DISCUSSION

Impact of Depolymerization on Polymer Viscosity and Nanoparticle Synthesis and Characterization

Hydrogen peroxide was used to depolymerize Sodium Alginate and Chitosan by generating free radicals that cleave their glycosidic bonds, producing oligosaccharides with reduced molecular weight and enhanced solubility. The extent of depolymerization was influenced by the concentration of hydrogen peroxide, reaction time, and temperature. Adjusting these parameters allowed for control over the molecular weights of the oligosaccharides, with temperature specifically depending on the concentration of hydrogen peroxide used [20,21]. Although lower molecular weight oligosaccharides are typically preferred to enhance solubility, a shorter reaction time was chosen to obtain polymer chains of varying lengths and molecular weights, with the goal of producing different nanoparticles. A preliminary characterization was performed by evaluating the viscosity, as shown in Table 2.

Sample	Yield (%)	Viscosity (mPas)
NDSA	-	1008 ± 26
DSA > 12 kDa	52 ± 3	357 ± 31
3.5 kDa < DSA < 12 kDa	31 ± 5	57 ± 9
DSA < 3.5 kDa	17 ± 4	13 ± 6
NDC	-	2462 ± 21
DC > 12 kDa	47 ± 2	572 ± 33
3.5 kDa < DC < 12 kDa	30 ± 4	80 ± 20
DC < 3.5 kDa	23 ± 8	34 ± 4

Table2. Yields and viscosity measurements of non-depolymerized and depolymerized Sodium Alginate (NDSA and DSA) and Chitosan (NDC and DC) fractions, each with defined molecular weight ranges.

Samples spanning different molecular weight ranges displayed distinct viscosities. A marked decrease in viscosity was evident for both polymers when their molecular weight dropped below 12–14 kDa. Notably, depolymerized polymers with molecular weights below 3.5 kDa exhibited an almost 1000-fold reduction in viscosity compared to native polymers. This substantial decline highlights the profound impact of molecular weight on polymer behavior, as lower molecular weight chains are associated with enhanced solubility and increased chain flexibility. These observations align with the Mark-Houwink equation, which describes the relationship between molecular weight and viscosity in polysaccharides.[52,53] A reduction in molecular weight typically leads to shorter polymer chains and reduced intermolecular entanglements, resulting in a significant decrease in viscosity. The depolymerization process also produced varying yields across molecular weight ranges (Table 2). The highest yield corresponded to polymers with molecular weights above 12–14 kDa, demonstrating that the chosen reaction time was not sufficient to extensively degrade the polymers into lower molecular weight fractions. A reaction time of 10 hours is recommended to achieve polymers with molecular weights below 3.5 kDa.

Following the evaluation of the depolymerization process and its impact on the molecular weight of the polymers, additional experiments were conducted to refine the synthesis protocol for alginate-chitosan nanoparticles and to select the optimal polymer molecular weight ranges. These experiments were carried out both in the presence and absence of a model protein, bovine serum albumin (BSA), using polymer fractions with varying molecular weight distributions, as detailed in Table 1. The aim was to investigate how the molecular weight of the depolymerized alginate and chitosan polymers influences nanoparticle formation, specifically examining properties such as size, PDI, and protein binding efficiency. The results of these experiments are presented in Figure 1 and Figure 2.

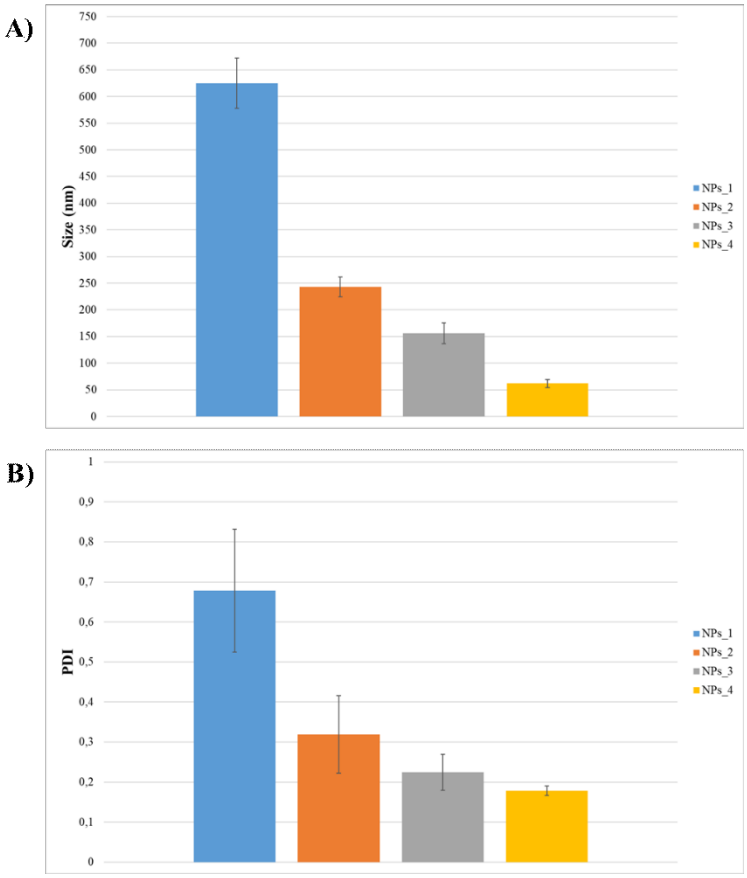

Fig. 1. Hydrodynamic diameter and PDI of NPs based on NDSA and NDC (NPs_1), DSA and DC at different MW (NPs_2, NPs_3 and NPs_4).

As illustrated in Figure 1, the size and PDI of the nanoparticles (NPs) are strongly influenced by the molecular weight of the polymers used in their synthesis. For the methodology employed, the most favorable sizes were observed in NPs synthesized from polymers with molecular weights below 12–14 kDa. A clear distinction emerged between NPs formed using 3.5 kDa and 12 kDa polymers: NPs_4 exhibited a z-average size of approximately 62 nm, whereas NPs_3 displayed a z-average size of about 156 nm. This trend underscores the critical role of polymer molecular weight, as even small variations can significantly affect the resulting nanoparticle dimensions.

In terms of PDI, polymers with molecular weights above 12–14 kDa tended to produce NPs with PDI values exceeding 0.3, indicating a less uniform size distribution. It is worth noting that a PDI value of approximately 0.3 is generally considered the upper threshold for a monodisperse population of polysaccharide-based NPs.[54] Conversely, NPs synthesized using polymers with

molecular weights below 12–14 kDa consistently exhibited PDI values under 0.3, signifying a more homogeneous population. Notably, these lower-molecular-weight polymers resulted in nanoparticles with similar PDI trends, reinforcing the notion that polymer chain flexibility and reduced molecular entanglement contribute to the formation of uniform nanoparticle populations.

To assess the protein binding efficiency of the synthesized alginate-chitosan nanoparticles, their re-binding capability was evaluated. The nanoparticles were incubated with a BSA protein solution, and the unbound protein in the supernatant was quantified using a BCA assay, as illustrated in Figure 2.

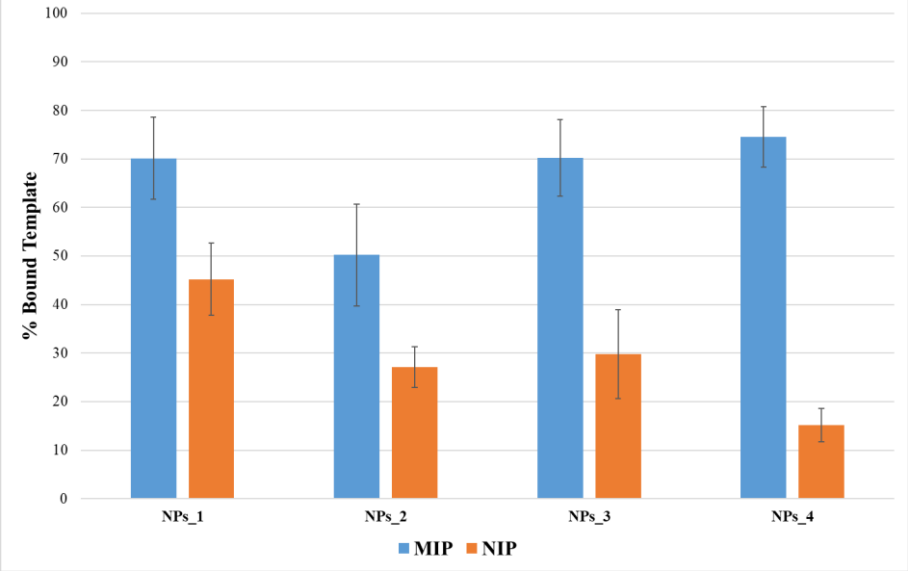

Fig. 2. Binding test of NPs based on NDSA and NDC (NPs_1), DSA and DC at different MW (NPs_2, NPs_3 and NPs_4).

The binding studies revealed a clear correlation between the molecular weight of the polymers and the protein binding efficiency. Nanoparticles synthesized from low molecular weight polymers exhibited significantly higher specificity for BSA, as evidenced by the superior binding efficiencies shown in Figure 2. Specifically, nanoparticles prepared with polymers below 3.5 kDa consistently outperformed those synthesized with higher molecular weight polymers. This suggests that shorter polymer chains not only favor smaller nanoparticle sizes and lower PDI values, but also increase the availability of binding sites, thereby enhancing the interaction with the target protein.

These results strongly support the selection of polymers with molecular weights around 3.5 kDa for subsequent nanoparticle production, as they offer an optimal balance between desirable physicochemical properties and effective protein binding capacity.

To provide useful information about the binding of these polymers near the fusion loop, several molecular docking studies were initially conducted using mixtures of two polymers, Chitosan (CHT) and Sodium Alginate (ALG), in varying amounts. The process began with 100% CHT and progressively reduced its proportion until reaching 100% ALG. The molecular docking studies were performed near the catalytic site, and the binding energy was calculated within a range of -4 to -5 kcal/mol.

Samples	**Docking ranking (Kcal·mol^{-1})**	**Best pose (Kcal·mol^{-1})**
Mix_1	from -4.4 to -4.9	-4,90
Mix_2	from -4.5 to 5.0	-5,00
Mix_3	from -4.70 to -5.20	-5,20
Mix_4	from -4.70 to -5.30	-5,30
Mix_5	from -4.8 to -5.4	-5,40

Table 3. Values from rigid Molecular Docking with flexible ligands

From the results obtained (Table 3), molecular docking suggests that increasing the ALG percentage enhanced its affinity for the protein, and more cationic residues are present laterally in the fusion ring (R98, K109), allowing better interaction with the alginate chains. This finding was later confirmed through MMPBSA decomposition analysis (Figure 3).

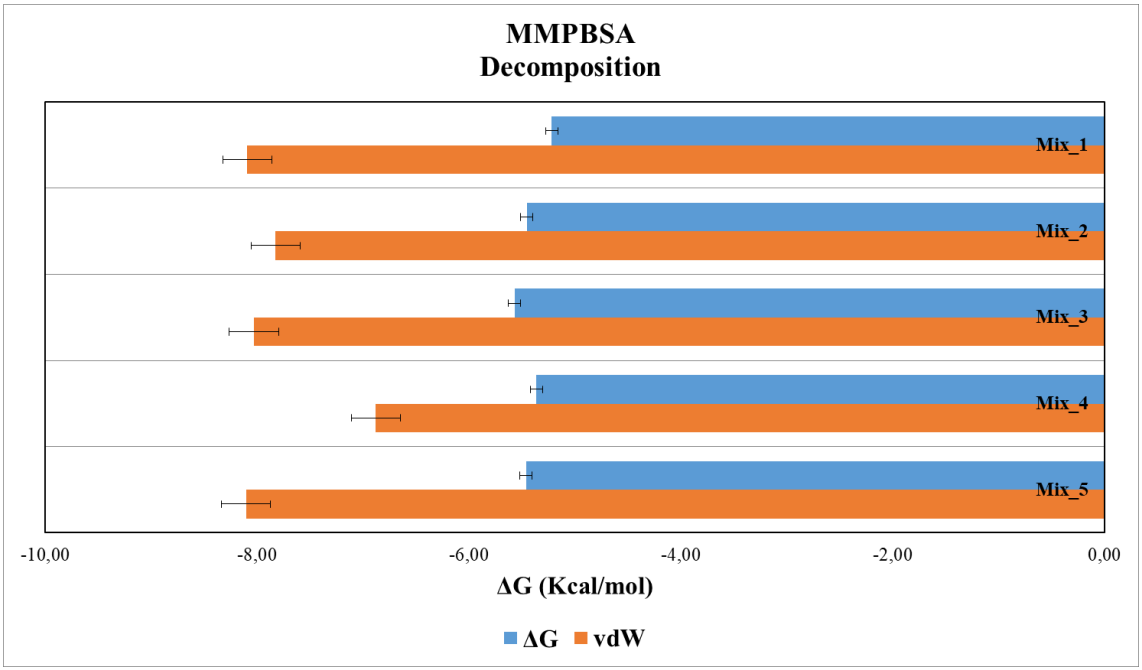

Fig. 3. Values of vdW energy and ΔG total from MMPBSA decomposition of all complexes

Through the MMPBSA energy decomposition, the specific contribution of the fusion loop in the interaction with the polymers was verified. The obtained values all settled around -5 kcal/mol, with a slight improvement in the case of Mix_3. From these results, it can be inferred that the interaction between the loop and the ligand stabilizes, thereby enhancing its binding affinity.

This stabilization is particularly relevant when considering the role of polymer mixtures in molecular imprinting. These mixtures are known to improve molecular recognition by accommodating a wider range of conformations, thus allowing greater interaction with multiple targets. This increased flexibility contributes to enhanced stability. Based on these observations, molecular dynamics simulations were performed on the three systems with both polymers in different ratios (Mix_2, Mix_3, Mix_4).

Subsequently, for these mixtures, the best docking pose was selected and Molecular Dynamics (MD) simulations were carried out for 200 ns in triplicate to accurately evaluate the affinity between the protein and the polymers. A structural analysis of the protein was performed, focusing on the fusion loop, the protein's binding site. To this end, the interactions were analyzed through a

minimum distance analysis of the residues in the fusion loop relative to the alginate and chitosan fragments, identifying specific interactions with these components (Figure 4).

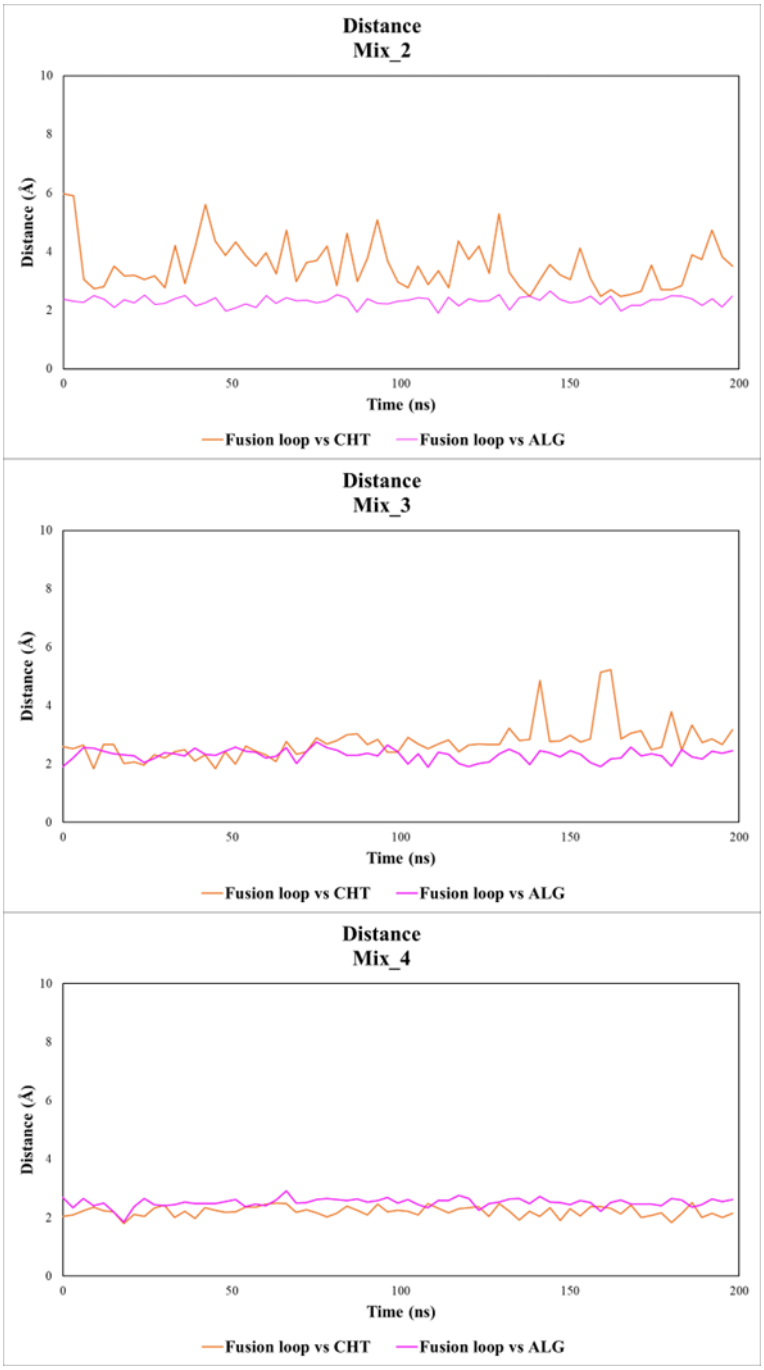

Fig. 4. Minimum distance between Fusion loop and CHT (in orange) and ALG (in violet)

In all cases, the distances between the ALG fragments and the residues of the fusion loop remained stable over time, stabilizing around 2-3 Å. This suggests strong interactions, such as hydrogen bonds and Van der Waals forces, which contribute to the stabilization of the complex. As previously

noted, the MMPBSA decomposition corroborates this observation, as shown in Figure 3. In contrast, for CHT, different behaviours were observed: stable interactions with the fusion loop were only detected when the CHT ratio exceeded that of ALG. In the case of Mix_2 and Mix_3 (highlighted in orange in Figure 4), the distances were unstable, with a preference for direct interactions with the alginate fragments instead. This finding aligns with the MMPBSA results obtained earlier.

Based on the Molecular Docking and Molecular Dynamics, it was decided to proceed with the preparation of the particles using a 50:50 ratio (Mix_3). For this reason, an emulsion-gelation technique was utilized to synthesize alginate-chitosan nanoparticles for the specific binding of the Zika virus envelope protein. This method was chosen due to its high yield, reproducibility, and ability to generate nanoparticles with specific binding sites for target proteins, making it ideal for the development of protein-imprinted nanoparticles.[55]

In this study, a modified ionotropic gelation (IG) method was employed to create molecularly imprinted nanoparticles (MIPs) using the Zika virus envelope protein as a template. The formulation was optimized by fine-tuning the concentrations of depolymerized Chitosan (CS) and Sodium Alginate (SA) solutions, along with the cross-linking agents Calcium Chloride ($CaCl_2$) and Sodium Tripolyphosphate (TPP). The use of depolymerized polymers necessitated elevated polymer concentrations compared to conventional protocols, leading to smaller particle sizes and minimized aggregation, as evidenced by Figure 5.

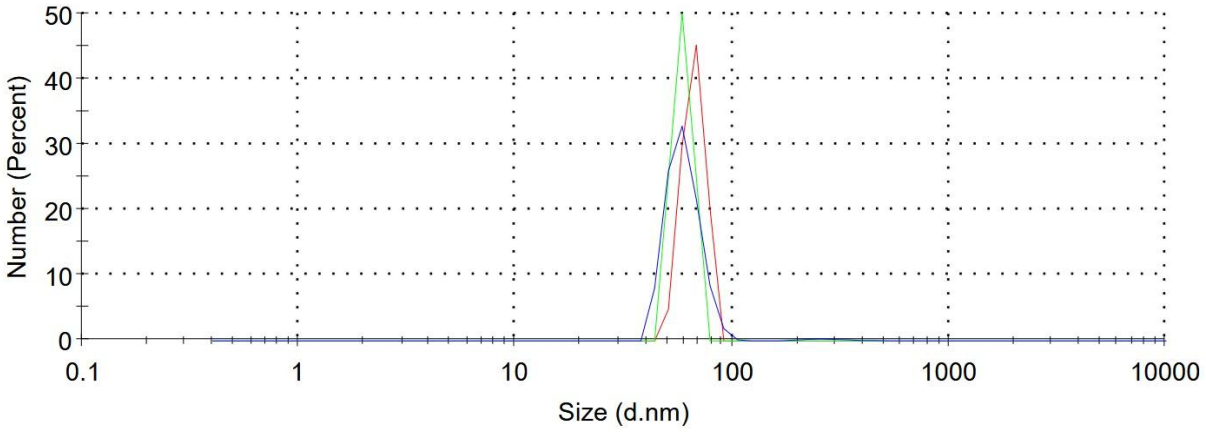

Fig. 5. Hydrodynamic diameter of MIP particles measured by DLS

The nanoparticles were characterized by dynamic light scattering (DLS) to determine their size and polydispersity index (PDI). MIP nanoparticles exhibited an average size of approximately 67 nm with a PDI of 0.232, while non-imprinted particles (NIPs) had a slightly smaller size of around 59 nm with a PDI of 0.211. The slight size increase in MIPs was likely due to interactions between the template protein and the polymer matrix during formation.

These nanoparticles were notably smaller than typical alginate or chitosan nanoparticles reported in the literature, a size reduction attributed to the controlled depolymerization process, which enhanced polymer dispersion and uniformity.[56,57] In addition, the pH used in synthesis process helped address issues of size variability and aggregation.[58] Within this range, the Zika virus envelope protein adopted a conformation with its fusion loop exposed, promoting optimal interactions with the polymer matrix.[59]

This study highlights the potential of the modified ionotropic gelation method and depolymerized polymers to overcome common challenges in nanoparticle synthesis, achieving more uniform particles with improved stability and performance.

The stability of nanoparticle suspensions in PBS at pH 7.4 (10^{-3} M) was assessed using the Turbiscan® DNS™ system, which measures changes in light transmission (ΔT%) and backscattering (ΔBS%) as a function of sample height and over time. These measurements were

then analyzed to obtain a global parameter reflecting the overall stability kinetics of the suspension, known as the Turbiscan Stability Index (TSI).[60] The analysis was carried out at two time points, after 24 hours and after 30 days, to evaluate any potential variation in the stability of the nanoparticles during both short- and long-term storage, as shown in Figure 6.

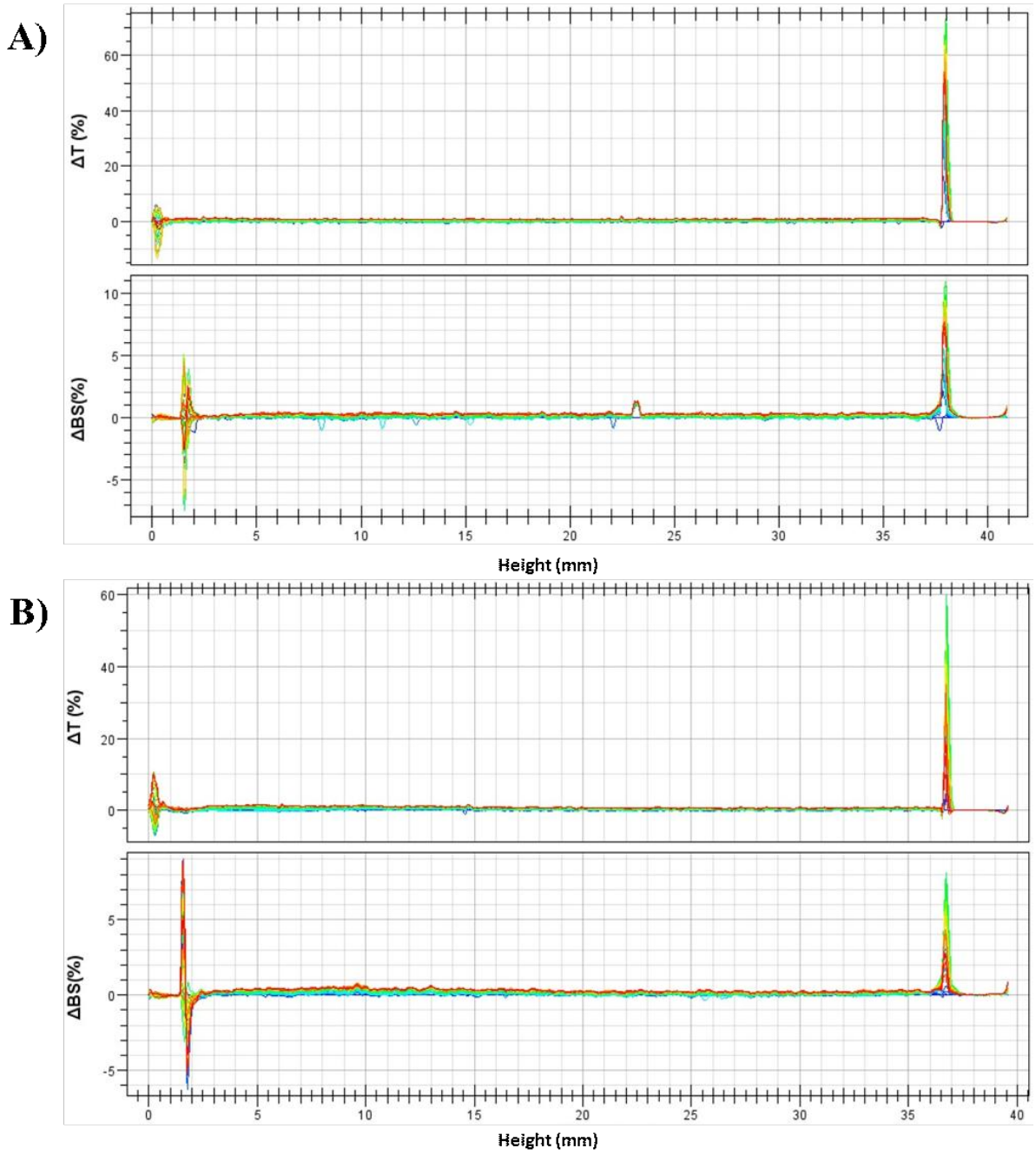

Fig. 6. Transmission intensity (ΔT%) and backscattering (ΔBS%) profiles of imprinted nanoparticles in PBS in function of time after one day (A) and 30 days (B) from synthesis.

The results demonstrated that the nanoparticle suspensions maintained excellent stability over both time points. Throughout the 24-hour and 30-day periods, variations in ΔBS% remained within a ±10% range, which is considered optimal for ensuring colloidal stability. This indicated that there were no substantial changes in the particles' size or aggregation behaviour, even after 30 days.

During the analysis, three distinct regions of the sample were observed. At the top of the vial, a positive variation in ΔT% was detected, suggesting a slight creaming phenomenon. This effect was reversible by gentle agitation, confirming that no permanent structural changes had occurred. In the middle of the vial, the measurements of both ΔT% and ΔBS% remained stable, indicating no significant aggregation or particle size alteration. In the lower section of the vial, similar stability was observed, reinforcing the conclusion that the nanoparticles did not undergo significant aggregation or size changes during the evaluation.

The observed destabilization was largely attributed to the migration of particles, rather than permanent changes in their structure or size. This migration was reversible and did not affect the overall colloidal stability. Furthermore, the Turbiscan Stability Index (TSI), calculated from the cumulative changes in ΔT% and ΔBS% along the sample height, remained low (< 0.8) at both 24 hours and 30 days, further confirming the stability of the molecularly imprinted nanoparticles.

Following the stability assessment, the molecularly imprinted nanoparticles (MIPs) were subjected to binding tests to evaluate their affinity and selectivity toward the Zika virus envelope protein, which served as the template for their synthesis. The binding performance of the MIPs was tested using 2 mg of nanoparticles mixed with standard ZIKV-E solutions at concentrations ranging from 0.1 to 1 mM. The amount of protein captured by the nanoparticles was measured using a BCA assay to evaluate their ability to specifically recognize and bind to the target protein, in comparison to the non-imprinted nanoparticles (NIPs), which were synthesized in the absence of the template protein.

The adsorption isotherms were studied to investigate the equilibrium binding capacity of the synthesized Molecularly Imprinted Nanoparticles (MIPs) and Non-Imprinted Nanoparticles (NIPs).

These experiments provide critical insights into the specific interactions between the nanoparticles and the template molecule, as well as their selectivity towards the target protein.

The equilibrium binding capacity (Q_e, mmol/g) was calculated using the equation:

$$Q_e = \frac{(C_i - C_e) \cdot V}{m}$$

where C_i and C_e (mM) represent the initial and equilibrium concentrations of ZIKV-E in solution, respectively, V (L) is the solution volume, and m (g) is the mass of nanoparticles.

To assess the selectivity of MIPs for ZIKV-E, binding experiments were also conducted using Human Serum Albumin (HSA), a non-target protein. This comparison enabled the evaluation of the specific recognition capacity of the imprinted nanoparticles. The Q_e values for both ZIKV-E and HSA were determined and compared for MIPs and NIPs, as depicted in Figure 7.

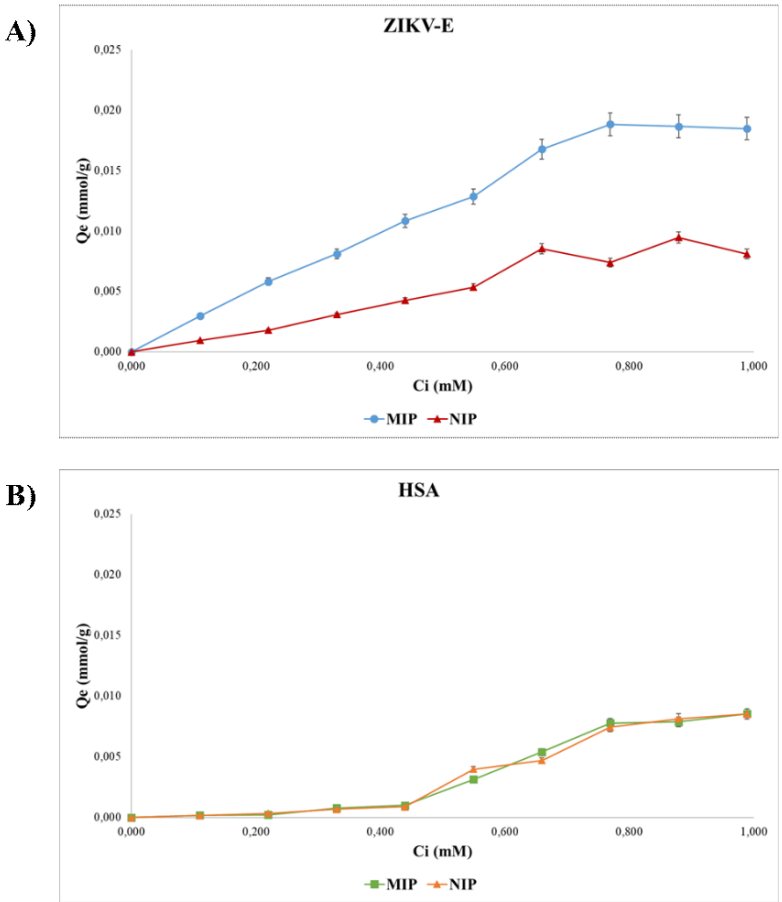

Fig. 7. Adsorption isotherms of (A) ZIKV-E and (B) HSA on MIPs and NIPs.

The results demonstrated a significantly higher binding capacity of MIPs for ZIKV-E compared to NIPs, confirming the presence of specific binding sites within the MIPs that are complementary in shape, size, and functionality to the ZIKV-E protein. In contrast, the binding capacity of MIPs for HSA was notably lower, indicating high selectivity of the imprinted sites for the target protein. The NIPs, synthesized in the absence of the template molecule, exhibited minimal and non-specific interactions with both ZIKV-E and HSA.

The results demonstrate the high capacity of MIPs to selectively recognize and bind to the ZIKV-E protein, attributed to the presence of specific cavities created during the molecular imprinting process. These cavities, complementary in terms of size, shape, and chemical functionality, ensure efficient interaction with the target, significantly surpassing the nonspecific interactions observed in NIPs. As reported in Table 4, analysis of the imprinting factor (α) consistently revealed values greater than 1.0 for ZIKV-E, confirming the superior binding capacity of MIPs compared to NIPs. Similarly, the selectivity coefficient (ε) highlighted a clear preference for ZIKV-E over HSA, further validating the high specificity of the imprinted sites.

C_i (mM)	Bound ZIKV-E (%)		Bound HSA (%)		α ZIKV-E	α HSA	ε
	MIP	NIP	MIP	NIP			
0.11	80.8 ± 1.2	25.8 ± 1.1	4.9 ± 0.3	4.3 ± 0.1	3.1	1.1	16.4
0.22	79.5 ± 1.4	24.4 ± 0.7	3.1 ± 0.1	4.8 ± 0.2	3.2	0.6	25.3
0.33	73.9 ± 1.7	28.0 ± 0.8	7.1 ± 0.2	6.2 ± 0.4	2.6	1.1	10.4
0.44	74.0 ± 0.9	29.0 ± 1.1	6.9 ± 0.1	6.0 ± 0.8	2.5	1.1	10.7
0.55	70.2 ± 1.1	29.3 ± 1.2	17.2 ± 0.5	21.8 ± 1.3	2.4	0.8	4.1
0.66	76.3 ± 1.7	38.9 ± 0.6	24.7 ± 0.9	21.4 ± 1.4	2.0	1.1	3.1
0.77	73.5 ± 1.9	28.8 ± 0.8	30.4 ± 1.1	29.1 ± 1.4	2.5	1.0	2.4
0.88	63.7 ± 2.7	32.3 ± 0.9	27.0 ± 0.6	27.9 ± 1.2	2.0	1.0	2.4
0.99	56.1 ± 1.7	24.6 ± 0.7	26.0 ± 0.7	26.0 ± 1.1	2.3	1.0	2.1

Table 4. Percentages of bound Zika virus envelope protein (ZIKV-E) and Human Serum Albumin (HAS) by imprinted (MIP) and non-imprinted (NIP) nanoparticles and α and ε values for different C_i.

To better understanding the adsorption properties of the synthesized MIP and NIP nanoparticles, the experimental binding data were evaluated using multiple theoretical models, including the Scatchard, Langmuir, and Freundlich isotherms.[61]

The Scatchard analysis, described by Equation (1), was employed to distinguish between homogeneous and heterogeneous binding sites. According to the Scatchard equation:

$$\frac{Q_e}{C_e} = (B_{max} - Q_e)\, K_a \qquad (1)$$

where Q_e represents the analyte bound per gram of polymer at equilibrium, C_e is the analyte concentration at equilibrium, B_{max} is the apparent maximum binding capacity and K_a is the association constant. The Scatchard plot of MIP exhibited two linear regions with different slopes, indicating the presence of high- and low-affinity binding sites, a hallmark of heterogeneous recognition cavities. Conversely, the NIP data showed a single straight line, confirming homogeneous binding sites.

The Langmuir model, described by Equation (2), assumes adsorption on homogeneous surfaces with uniform binding sites, resulting in a monolayer coverage of analyte molecules:

$$\frac{1}{Q_e} = \frac{1}{Q_{max}\, C_e\, K_L} + \frac{1}{Q_{max}} \qquad (2)$$

where, Q_{max} represents the maximum adsorption capacity and K_L is the Langmuir constant related to the adsorption affinity. The linearity of the Langmuir plots for MIP and NIP allowed for the determination of these parameters, indicating the maximum surface coverage achievable under equilibrium conditions.

In contrast, the Freundlich isotherm, an empirical model described by Equation (3) and Equation (4), accounts for adsorption on heterogeneous surfaces, where binding affinity varies across sites:

$$Q_e = K_F\, {C_e}^m \qquad (3)$$

or in its linearized form:

$$log(Q_e) = \log(K_F) + m \log (C_e) \qquad (4)$$

where, K_F indicates the adsorption capacity, and *m*, the heterogeneity index, reflects the variability of binding sites. The Freundlich plots for MIP and NIP showed good linearity, with mm values suggesting a cooperative adsorption mechanism.

Based on the R^2 values, the Langmuir model better described the adsorption of ZIKV-E on the prepared MIP, with an R^2 value of 0.98, indicating a preference for homogeneous binding sites and monolayer adsorption. However, the Freundlich model provided additional insights into the heterogeneity of the binding sites, particularly in the case of the NIP. This comprehensive evaluation underscores the nuanced binding behaviour of the imprinted materials.

In addition to the adsorption isotherms, further binding studies were conducted using Quartz Crystal Microbalance with Dissipation (QCM-D) to provide deeper insights into the interactions of ZIKV-E with the synthesized MIPs. QCM-D offers the advantage of monitoring real-time changes in mass and viscoelastic properties of the polymer surface, allowing for a more detailed understanding of the binding dynamics.[62]

Initially, the sensor surface was functionalized with a Self-Assembled Monolayer (SAM) of mercaptohexadecanoic acid (MHA) and mercaptoundecanol (MU), which acted as spacers to enhance the interaction between the gold coating and the analyte. The next step involved immobilizing the target analyte, ZIKV-E, on the sensor surface using sulfo-NHS:EDC coupling chemistry. Changes in resonant frequency during the immobilization process were monitored to track the progression of binding events. The analyte quantities on the sensor surface were determined using the Sauerbrey equation, revealing a ZIKV-E surface concentration of 1.2×10^{-12} $mol \cdot cm^{-2}$ and a HSA concentration of 1.3×10^{-12} $mol \cdot cm^{-2}$. These similar values indicate comparable surface coverage for the two proteins, suggesting that the immobilization process was consistent and reproducible.

After immobilizing ZIKV-E and HSA, the binding interactions of the prepared nanoparticles were investigated. Binding isotherms for both MIPs and non-imprinted polymers (NIPs) were obtained

by injecting increasing concentrations of MIPs onto the functionalized sensor surfaces and monitoring the corresponding frequency shifts in real time (Figure 8).

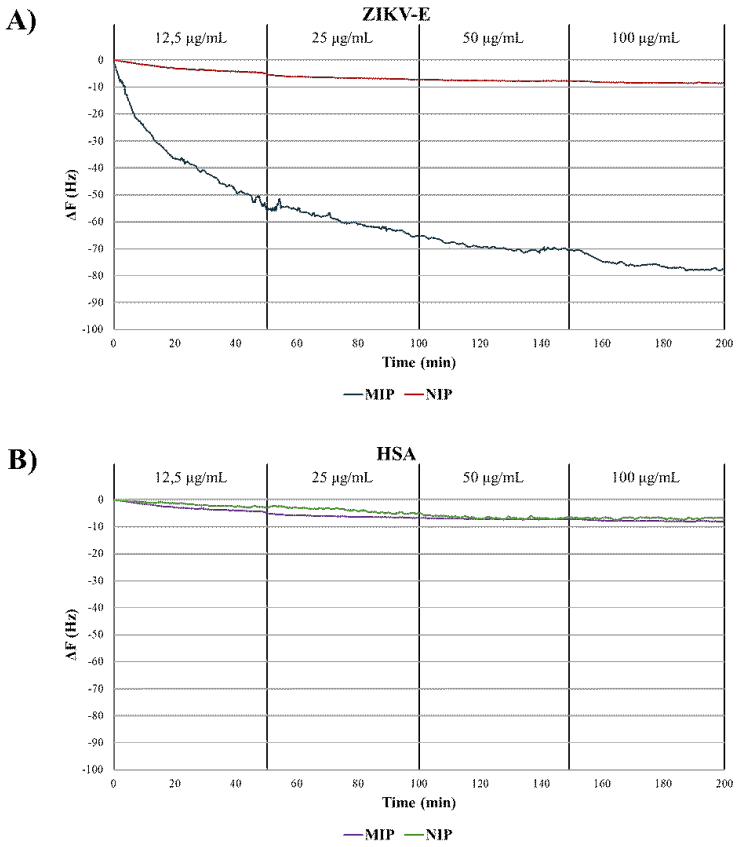

Fig. 8. Real-time resonant frequency changes ΔF (Hz) after repeated injections of MIP and NIP dispersions of increasing concentration on functionalized QCM-D sensor chips with (A) ZIKV-E and (B) HSA

As depicted in Figure 8A, the MIPs displayed a pronounced concentration-dependent binding trend toward ZIKV-E. The significant frequency shifts observed with increasing MIP concentrations were indicative of strong and specific interactions between the imprinted cavities of the MIPs and the ZIKV-E protein. In contrast, the NIPs showed much weaker binding, with minimal frequency shifts, suggesting non-specific interactions that were not mediated by imprinting.

Similarly, when the sensor surface was functionalized with HSA (Figure 8B), the MIPs exhibited very low binding, further corroborating their specificity for ZIKV-E. The NIPs also demonstrated negligible binding to HSA, confirming that the imprinted MIPs do not interact non-specifically with non-target proteins, even at elevated concentrations.

To quantify binding affinity, the experimental data were fitted to a Langmuir adsorption model (Figure 9). From these fits, the dissociation constant (K_D) for MIP binding to ZIKV-E was calculated as 5.65 ± 0.2 nM, indicating high binding affinity for the target molecule. In contrast, the K_D value for NIP binding was significantly higher, reinforcing the notion that MIPs are highly selective for ZIKV-E.

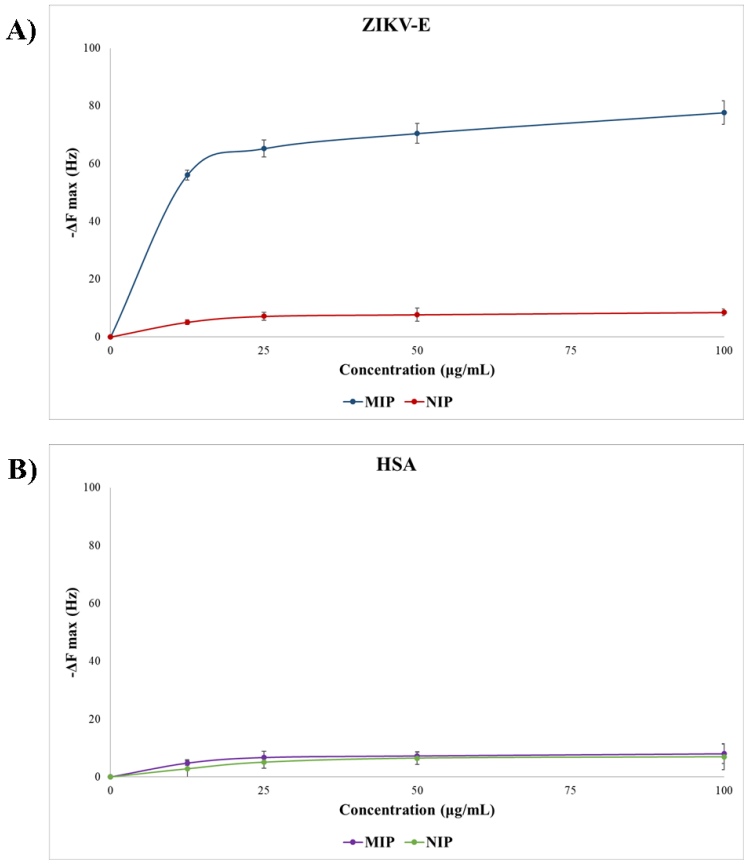

Fig. 9. Apparent non-equilibrium binding isotherms of MIP and NIP on a ZIKV-E (A) and HSA (B) functionalized sensor chip.

These results underscore the considerable potential of MIPs as selective binding agents for ZIKV-E, with strong specificity and minimal off-target interactions. The use of HSA as a control further highlights the selectivity of MIPs, as they preferentially bound to the target antigen with minimal interaction with non-target proteins. This demonstrates the utility of MIPs in highly specific molecular recognition applications, such as diagnostics and sensing technologies.

Safety assessments were performed to evaluate the potential cytotoxic and immunogenic effects of the test substances. The evaluations utilized two well-established in vitro methodologies: the NRU assay and the Human Cell Line Activation Test (h-CLAT).

The cytotoxic potential of the tested sample was evaluated using the Neutral Red Uptake (NRU) assay, in accordance with the ISO 10993-5:2009 guidelines.[50] Prior to the assay, cell culture integrity was examined microscopically after 24 hours of incubation with the nanoparticle dispersion and the positive control (1% SDS). The evaluation focused on cell morphology and any signs of biological reactivity, including cellular abnormalities or degeneration, which were graded on a scale from 0 (no reactivity) to 4 (severe reactivity).

Microscopic observations revealed that BALB/3T3 fibroblast cells maintained normal morphology when exposed to the test sample, showing no signs of cellular degeneration or abnormalities. The biological reactivity grade for these conditions was consistently 0, indicating no observable adverse effects. In contrast, cells treated with the positive control exhibited significant degeneration, including pronounced cell rounding and detachment, resulting in a reactivity grade of 4.

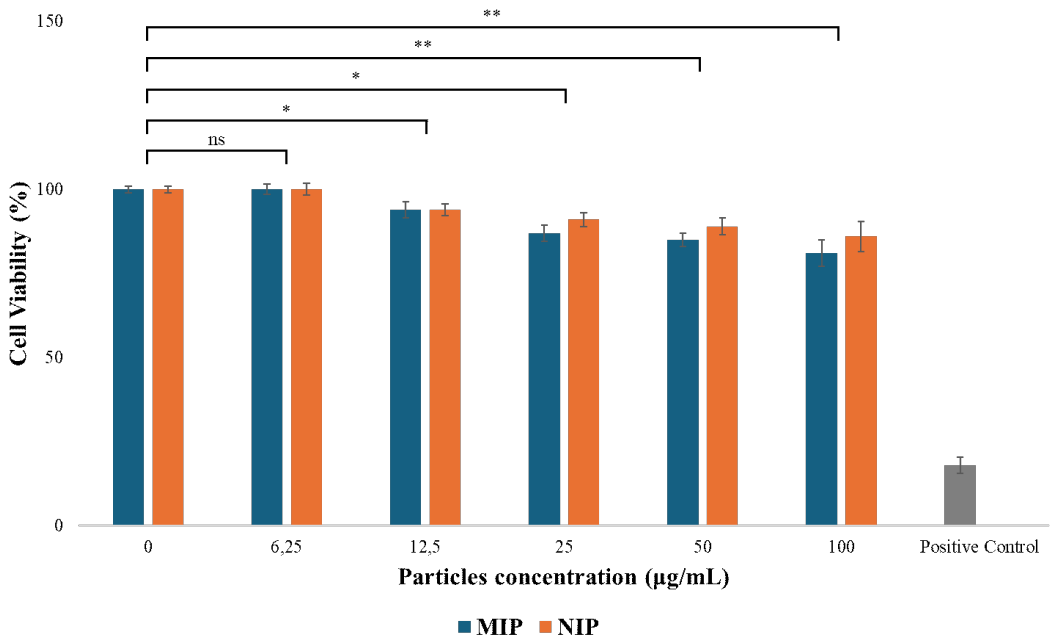

*Fig. 10. Cell viability: the NRU test conducted on Balb/3T3 cells following a 24-hour exposure to escalating concentrations of MIP and NIP. Data are expressed as means ± SEM, statistical significance: *p < 0.05, **p < 0.01.*

Quantitative analysis of cell viability, presented in Figure 10, demonstrated that exposure to the nanoparticle dispersion resulted in cell viability exceeding 75% across all experimental conditions. This viability threshold is consistent with non-cytotoxic behaviour, as defined by ISO standards. Conversely, treatment with the positive control led to a marked reduction in cell viability, confirming its cytotoxicity and validating the assay.

These findings confirm that the nanoparticles are non-toxic to BALB/3T3 fibroblast cells under the tested conditions. The absence of cytotoxicity and cellular abnormalities highlights the biocompatibility of the sample, suggesting its potential for applications that require safe interaction with biological systems.

To evaluate the potential for sensitization of the nanoparticle dispersion, the h-CLAT assay was performed according to the OECD 442E guidelines. This assay measures the activation of THP-1 cells by assessing the expression levels of CD86 and CD54, which are crucial markers for immune cell activation. The cells were exposed to high concentrations of the test substance for 24 hours, with concentration levels selected based on preliminary cytotoxicity data to determine the CV75 values.

The sensitization potential of the test substances was assessed by determining the Effective Concentration (EC) values for CD86 and CD54. The EC represents the concentration at which the Relative Fluorescence Intensity (RFI) reaches thresholds of 150% for CD86 or 200% for CD54. Each experiment was conducted in triplicate across three independent days, and the median EC150 and EC200 values were calculated. If two out of three independent runs met the positive criteria, the highest EC value (either EC150 or EC200) was used to determine the final result. An increase in CD86 and CD54 expression on THP-1 cells indicates immune system activation, suggesting a potential sensitizing effect of the tested substance.

SAMPLES	CD54	CD86
MIP	167	125
NIP	145	112
NEGATIVE CONTROL	109	104
POSITIVE CONTROL	331	286
CUT-OFF	200	150

Table 5. RFI% value of CD54 and CD86 on THP-1 monocytes.

The results, presented in Table 5, show that none of the tested high concentrations of the sample caused an RFI% for CD86 ≥150% or CD54 ≥200%. This confirms that the sample did not induce sensitization. These findings emphasize the non-sensitizing nature of the tested material and further support its biocompatibility and safety for biological applications.

CONCLUSION

The development of molecularly imprinted polysaccharide-based nanoparticles marks a significant advancement in creating highly specific, stable, and biocompatible nanomaterials for molecular recognition. This study emphasizes the successful synthesis and optimization of these nanoparticles, which demonstrate improved stability, uniformity, and reproducibility through careful formulation and process control. The choice of sodium alginate and chitosan, with their intrinsic biocompatibility and biodegradability, further bolsters the potential of these nanoparticles for therapeutic applications.

The depolymerization of these polysaccharides using hydrogen peroxide proved effective for fine-tuning the molecular weight and enhancing the solubility of the resulting oligosaccharides. This method enabled the preparation of nanoparticles with smaller sizes and optimal monodispersity. The stability of these nanoparticles was further evidenced by stable TSI values, confirming their ability to be stored for extended periods without loss of functionality. These findings suggest the nanoparticles' suitability for scalable production and long-term storage, enhancing their utility in various biomedical applications.

Binding isotherms and QCM-D analysis revealed that the molecularly imprinted polysaccharide nanoparticles (MIPs) exhibited significantly higher binding capacity and specificity for the ZIKV-E target molecule compared to non-imprinted polymers (NIPs), highlighting their potential for precise molecular recognition. Additionally, the biocompatibility and non-sensitizing properties of these MIPs, demonstrated through cell viability assays and the human Cell Line Activation Test (h-CLAT), underscore their safety for biomedical applications.

These findings support the potential of these nanoparticles as a promising platform for combating Zika virus infections and other emerging viral outbreaks.

REFERENCES

[1] L.R. Petersen, D.J. Jamieson, A.M. Powers, M.A. Honein, Zika Virus, New England Journal of Medicine 374 (2016) 1552–1563.

[2] A. Gulland, Zika virus is a global public health emergency, declares WHO, BMJ (2016) i657.

[3] M. Mercado-Reyes, J. Acosta-Reyes, E. Navarro-Lechuga, S. Corchuelo, A. Rico, E. Parra, N. Tolosa, L. Pardo, M. González, J. Martìn-Rodriguez-Hernández, L. Karime-Osorio, M. Ospina-Martinez, H. Rodriguez-Perea, G. Del Rio-Pertuz, D. Viasus, Dengue, chikungunya and zika virus coinfection: results of the national surveillance during the zika epidemic in Colombia, Epidemiol Infect 147 (2019) e77.

[4] G. Venturi, L. Zammarchi, C. Fortuna, M.E. Remoli, E. Benedetti, C. Fiorentini, M. Trotta, C. Rizzo, A. Mantella, G. Rezza, A. Bartoloni, An autochthonous case of Zika due to possible sexual transmission, Florence, Italy, 2014, Eurosurveillance 21 (2016).

[5] A. Miranda-López, O. González-Ortega, D.O. Govea-Alonso, L. Betancourt-Mendiola, M. Comas-García, S. Rosales-Mendoza, Rational design and production of a chimeric antigen targeting Zika virus that induces neutralizing antibodies in mice, Vaccine 42 (2024) 3674–3683.

[6] H. Zhao, E. Fernandez, K.A. Dowd, S.D. Speer, D.J. Platt, M.J. Gorman, J. Govero, C.A. Nelson, T.C. Pierson, M.S. Diamond, D.H. Fremont, Structural Basis of Zika Virus-Specific Antibody Protection, Cell 166 (2016) 1016–1027.

[7] A. Qadir, M. Riaz, M. Saeed, S. Shahzad-ul-Hussan, Potential targets for therapeutic intervention and structure based vaccine design against Zika virus, Eur J Med Chem 156 (2018) 444–460.

[8] C.R. Fontes-Garfias, C. Shan, H. Luo, A.E. Muruato, D.B.A. Medeiros, E. Mays, X. Xie, J. Zou, C.M. Roundy, M. Wakamiya, S.L. Rossi, T. Wang, S.C. Weaver, P.-Y. Shi, Functional Analysis of Glycosylation of Zika Virus Envelope Protein, Cell Rep 21 (2017) 1180–1190.

[9] D.L. Carbaugh, R.S. Baric, H.M. Lazear, Envelope Protein Glycosylation Mediates Zika Virus Pathogenesis, J Virol 93 (2019).

[10] F. Giovannoni, I. Bosch, C.M. Polonio, M.F. Torti, M.A. Wheeler, Z. Li, L. Romorini, M.S. Rodriguez Varela, V. Rothhammer, A. Barroso, E.C. Tjon, L.M. Sanmarco, M.C. Takenaka, S.M.S. Modaresi, C. Gutiérrez-Vázquez, N.G. Zanluqui, N.B. dos Santos, C.D. Munhoz, Z. Wang, E.B. Damonte, D. Sherr, L. Gehrke, J.P.S. Peron, C.C. Garcia, F.J. Quintana, AHR is a Zika virus host factor and a candidate target for antiviral therapy, Nat Neurosci 23 (2020) 939–951.

[11] D. Michlmayr, P. Andrade, K. Gonzalez, A. Balmaseda, E. Harris, CD14+CD16+ monocytes are the main target of Zika virus infection in peripheral blood mononuclear cells in a paediatric study in Nicaragua, Nat Microbiol 2 (2017) 1462–1470.

[12] W. Shuaib, H. Stanazai, A.G. Abazid, A.A. Mattar, Re-Emergence of Zika Virus: A Review on Pathogenesis, Clinical Manifestations, Diagnosis, Treatment, and Prevention, Am J Med 129 (2016) 879.e7-879.e12.

[13] L. Priyamvada, K.M. Quicke, W.H. Hudson, N. Onlamoon, J. Sewatanon, S. Edupuganti, K. Pattanapanyasat, K. Chokephaibulkit, M.J. Mulligan, P.C. Wilson, R. Ahmed, M.S. Suthar, J. Wrammert, Human antibody responses after dengue virus infection are highly cross-reactive to Zika virus, Proceedings of the National Academy of Sciences 113 (2016) 7852–7857.

[14] E.A. Bhat, T. Ali, N. Sajjad, R. kumar, P. Bron, Insights into the structure, functional perspective, and pathogenesis of ZIKV: an updated review, Biomedicine & Pharmacotherapy 165 (2023) 115175.

[15] M. Dattilo, M.F. Motta, F. Patitucci, C. Ferraro, O.I. Parisi, F. Puoci, Exploring crosslinker effects on fluorescent molecularly imprinted polymers for improved gefitinib delivery in lung cancer theranostics, Mater Adv 5 (2024) 6446–6457.

[16] B. Tse Sum Bui, A. Mier, K. Haupt, Molecularly Imprinted Polymers as Synthetic Antibodies for Protein Recognition: The Next Generation, Small 19 (2023).

[17] S. Scorrano, L. Mergola, R. Del Sole, G. Vasapollo, Synthesis of Molecularly Imprinted Polymers for Amino Acid Derivates by Using Different Functional Monomers, Int J Mol Sci 12 (2011) 1735–1743.

[18] M. Włoch, J. Datta, Synthesis and polymerisation techniques of molecularly imprinted polymers, in: 2019: pp. 17–40.

[19] O.I. Parisi, F. Francomano, M. Dattilo, F. Patitucci, S. Prete, F. Amone, F. Puoci, The Evolution of Molecular Recognition: From Antibodies to Molecularly Imprinted Polymers (MIPs) as Artificial Counterpart, J Funct Biomater 13 (2022) 12.

[20] G. Jamalipour Soufi, S. Iravani, R.S. Varma, Molecularly imprinted polymers for the detection of viruses: challenges and opportunities, Analyst 146 (2021) 3087–3100.

[21] A.K. Yadav, D. Verma, N. Dalal, A. Kumar, P.R. Solanki, Molecularly imprinted polymer-based nanodiagnostics for clinically pertinent bacteria and virus detection for future pandemics, Biosens Bioelectron X 12 (2022) 100257.

[22] V. Ricotta, Y. Yu, N. Clayton, Y.-C. Chuang, Y. Wang, S. Mueller, K. Levon, M. Simon, M. Rafailovich, A chip-based potentiometric sensor for a Zika virus diagnostic using 3D surface molecular imprinting, Analyst 144 (2019) 4266–4280.

[23] J. Yang, S. Han, H. Zheng, H. Dong, J. Liu, Preparation and application of micro/nanoparticles based on natural polysaccharides, Carbohydr Polym 123 (2015) 53–66.

[24] R. Hasanzadeh, P. Mihankhah, T. Azdast, A. Rasouli, M. Shamkhali, C.B. Park, Biocompatible tissue-engineered scaffold polymers for 3D printing and its application for 4D printing, Chemical Engineering Journal 476 (2023) 146616.

[25] L.A. Picos-Corrales, A.M. Morales-Burgos, J.P. Ruelas-Leyva, G. Crini, E. García-Armenta, S.A. Jimenez-Lam, L.E. Ayón-Reyna, F. Rocha-Alonzo, L. Calderón-Zamora, U. Osuna-Martínez, A. Calderón-Castro, G. De-Paz-Arroyo, L.N. Inzunza-Camacho, Chitosan as an Outstanding Polysaccharide Improving Health-Commodities of Humans and Environmental Protection, Polymers (Basel) 15 (2023) 526.

[26] A. Plucinski, Z. Lyu, B.V.K.J. Schmidt, Polysaccharide nanoparticles: from fabrication to applications, J Mater Chem B 9 (2021) 7030–7062.

[27] J. Kurczewska, Recent Reports on Polysaccharide-Based Materials for Drug Delivery, Polymers (Basel) 14 (2022) 4189.

[28] P. Tran, J.-S. Park, Alginate-coated chitosan nanoparticles protect protein drugs from acid degradation in gastric media, J Pharm Investig 52 (2022) 465–476.

[29] J. Cao, J. Cheng, S. Xi, X. Qi, S. Shen, Y. Ge, Alginate/chitosan microcapsules for in-situ delivery of the protein, interleukin-1 receptor antagonist (IL-1Ra), for the treatment of dextran sulfate sodium (DSS)-induced colitis in a mouse model, European Journal of Pharmaceutics and Biopharmaceutics 137 (2019) 112–121.

[30] B. Zhao, N.F. Alonso, J. Miras, S. Vílchez, M.J. García-Celma, G. Morral, J. Esquena, Triggered protein release from calcium alginate/chitosan gastro-resistant capsules, Colloids Surf A Physicochem Eng Asp 693 (2024) 133998.

[31] T.M. Aida, T. Yamagata, M. Watanabe, R.L. Smith, Depolymerization of sodium alginate under hydrothermal conditions, Carbohydr Polym 80 (2010) 296–302.

[32] I. Aranaz, A.R. Alcántara, M.C. Civera, C. Arias, B. Elorza, A. Heras Caballero, N. Acosta, Chitosan: An Overview of Its Properties and Applications, Polymers (Basel) 13 (2021) 3256.

[33] S. Mao, T. Zhang, W. Sun, X. Ren, The depolymerization of sodium alginate by oxidative degradation, Pharm Dev Technol 17 (2012) 763–769.

[34] M.F.J.D.P. Tanasale, C.M. Bijang, E. Rumpakwara, Preparation of Chitosan with Various Molecular Weight and Its Effect on Depolymerization of Chitosan with Hydrogen Peroxide using Conventional Technique, Int J Chemtech Res 12 (2019) 112–120.

[35] F. Tian, Y. Liu, K. Hu, B. Zhao, Study of the depolymerization behavior of chitosan by hydrogen peroxide, Carbohydr Polym 57 (2004) 31–37.

[36] M. Xing, Q. Cao, Y. Wang, H. Xiao, J. Zhao, Q. Zhang, A. Ji, S. Song, Advances in Research on the Bioactivity of Alginate Oligosaccharides, Mar Drugs 18 (2020) 144.

[37] M. Wang, L. Chen, Z. Zhang, Potential applications of alginate oligosaccharides for biomedicine – A mini review, Carbohydr Polym 271 (2021) 118408.

[38] F.C. MacLaughlin, R.J. Mumper, J. Wang, J.M. Tagliaferri, I. Gill, M. Hinchcliffe, A.P. Rolland, Chitosan and depolymerized chitosan oligomers as condensing carriers for in vivo plasmid delivery, Journal of Controlled Release 56 (1998) 259–272.

[39] N. Maganti, P.K.C. Venkat Surya, W.W. Thein-Han, T.C. Pesacreta, R.D.K. Misra, Structure–Process–Property Relationship of Biomimetic Chitosan-Based Nanocomposite Scaffolds for Tissue Engineering: Biological, Physico-Chemical, and Mechanical Functions, Adv Eng Mater 13 (2011).

[40] C. Knill, J. Kennedy, J. Mistry, M. Miraftab, G. Smart, M. Groocock, H. Williams, Acid hydrolysis of commercial chitosans, Journal of Chemical Technology & Biotechnology 80 (2005) 1291–1296.

[41] S. Lu, K. Na, J. Wei, L. Zhang, X. Guo, Alginate oligosaccharides: The structure-function relationships and the directional preparation for application, Carbohydr Polym 284 (2022) 119225.

[42] L. Dai, J. Song, X. Lu, Y.-Q. Deng, A.M. Musyoki, H. Cheng, Y. Zhang, Y. Yuan, H. Song, J. Haywood, H. Xiao, J. Yan, Y. Shi, C.-F. Qin, J. Qi, G.F. Gao, Structures of the Zika Virus Envelope Protein and Its Complex with a Flavivirus Broadly Protective Antibody, Cell Host Microbe 19 (2016) 696–704.

[43] O. Trott, A.J. Olson, AutoDock Vina: Improving the speed and accuracy of docking with a new scoring function, efficient optimization, and multithreading, J Comput Chem 31 (2010) 455–461.

[44] D.A. Case, H.M. Aktulga, K. Belfon, D.S. Cerutti, G.A. Cisneros, V.W.D. Cruzeiro, N. Forouzesh, T.J. Giese, A.W. Götz, H. Gohlke, S. Izadi, K. Kasavajhala, M.C. Kaymak, E. King, T. Kurtzman, T.-S. Lee, P. Li, J. Liu, T. Luchko, R. Luo, M. Manathunga, M.R. Machado, H.M. Nguyen, K.A. O'Hearn, A. V. Onufriev, F. Pan, S. Pantano, R. Qi, A. Rahnamoun, A. Risheh, S. Schott-Verdugo, A. Shajan, J. Swails, J. Wang, H. Wei, X. Wu, Y. Wu, S. Zhang, S. Zhao, Q. Zhu, T.E. Cheatham, D.R. Roe, A. Roitberg, C. Simmerling, D.M. York, M.C. Nagan, K.M. Merz, AmberTools, J Chem Inf Model 63 (2023) 6183–6191.

[45] S. Pronk, S. Páll, R. Schulz, P. Larsson, P. Bjelkmar, R. Apostolov, M.R. Shirts, J.C. Smith, P.M. Kasson, D. van der Spoel, B. Hess, E. Lindahl, GROMACS 4.5: a high-throughput and highly parallel open source molecular simulation toolkit, Bioinformatics 29 (2013) 845–854.

[46] J.A. Maier, C. Martinez, K. Kasavajhala, L. Wickstrom, K.E. Hauser, C. Simmerling, ff14SB: Improving the Accuracy of Protein Side Chain and Backbone Parameters from ff99SB, J Chem Theory Comput 11 (2015) 3696–3713.

[47] J. Wang, R.M. Wolf, J.W. Caldwell, P.A. Kollman, D.A. Case, Development and testing of a general amber force field, J Comput Chem 25 (2004) 1157–1174.

[48] M.A. Azevedo, A.I. Bourbon, A.A. Vicente, M.A. Cerqueira, Alginate/chitosan nanoparticles for encapsulation and controlled release of vitamin B2, Int J Biol Macromol 71 (2014) 141–146.

[49] M.A. Hosseini, M. Kharaziha, Design of molecularly imprinted alginate microgels for topical release of insulin, Mater Today Commun 39 (2024) 109285.

[50] Biological Evaluation of Medical Devices—Part 5: Tests for In Vitro Cytotoxicity, (2009).

[51] R. Malivindi, F. Patitucci, S. Prete, M. Dattilo, A.E. Leonetti, N. Scigliano, O.I. Parisi, F. Puoci, Efficacy and safety assessment of PIMIN050 raft-forming system as medical device based on Citrus sinensis and Crassostrea gigas for the management of gastroesophageal reflux disease, J Drug Deliv Sci Technol 78 (2022).

[52] K.I. Draget, G. Skjåk Bræk, O. Smidsrød, Alginic acid gels: the effect of alginate chemical composition and molecular weight, Carbohydr Polym 25 (1994) 31–38.

[53] M.R. Kasaai, Calculation of Mark–Houwink–Sakurada (MHS) equation viscometric constants for chitosan in any solvent–temperature system using experimental reported viscometric constants data, Carbohydr Polym 68 (2007) 477–488.

[54] S. Pistone, D. Qoragllu, G. Smistad, M. Hiorth, Multivariate analysis for the optimization of polysaccharide-based nanoparticles prepared by self-assembly, Colloids Surf B Biointerfaces 146 (2016) 136–143.

[55] K. Haupt, P.X. Medina Rangel, B.T.S. Bui, Molecularly Imprinted Polymers: Antibody Mimics for Bioimaging and Therapy, Chem Rev 120 (2020) 9554–9582.

[56] T. Wu, C. Wu, S. Fu, L. Wang, C. Yuan, S. Chen, Y. Hu, Integration of lysozyme into chitosan nanoparticles for improving antibacterial activity, Carbohydr Polym 155 (2017) 192–200.

[57] M. Hamidi, A. Azadi, P. Rafiei, Hydrogel nanoparticles in drug delivery, Adv Drug Deliv Rev 60 (2008) 1638–1649.

[58] B. Sarmento, D.C. Ferreira, L. Jorgensen, M. van de Weert, Probing insulin's secondary structure after entrapment into alginate/chitosan nanoparticles, European Journal of Pharmaceutics and Biopharmaceutics 65 (2007) 10–17.

[59] Y. Modis, S. Ogata, D. Clements, S.C. Harrison, Structure of the dengue virus envelope protein after membrane fusion, Nature 427 (2004) 313–319.

[60] R.M. Derbali, V. Aoun, G. Moussa, G. Frei, S.F. Tehrani, J.C. Del'Orto, P. Hildgen, V.G. Roullin, J.L. Chain, Tailored Nanocarriers for the Pulmonary Delivery of Levofloxacin against Pseudomonas aeruginosa : A Comparative Study, Mol Pharm 16 (2019) 1906–1916.

[61] O.I. Parisi, M. Ruffo, R. Malivindi, A.F. Vattimo, V. Pezzi, F. Puoci, Molecularly Imprinted Polymers (MIPs) as Theranostic Systems for Sunitinib Controlled Release and Self-Monitoring in Cancer Therapy, Pharmaceutics 12 (2020) 41.

[62] M.C. Dixon, Quartz Crystal Microbalance with Dissipation Monitoring: Enabling Real-Time Characterization of Biological Materials and Their Interactions, 2008..

CONCLUSION

This thesis explores the potential of Molecularly Imprinted Polymers (MIPs) as versatile synthetic platforms, offering a promising alternative to traditional antibody-based technologies. Antibodies have limitations—such as high cost, low stability, and immunogenicity—highlighting the need for alternative solutions. The studies presented in this work demonstrate how MIPs can address these challenges across various applications.

A preliminary study conducted during this research period focused on the development of MIP nanogels for detecting human Chorionic Gonadotropin (hCG), a hormone commonly used in pregnancy tests. This study laid the foundation for the subsequent development and characterization of MIP nanoparticles. By designing MIP nanogels to bind two distinct epitopes of hCG, the research introduced an innovative, sensitive, and specific detection system. The results demonstrate how MIPs can overcome the limitations of traditional antibody-based tests, such as challenges in production and storage, offering a reusable and scalable alternative. Moreover, the potential of MIP nanogels extends beyond pregnancy testing, establishing a framework for applying the production and characterization technologies developed in this study to create nanoparticles. This knowledge could play a crucial role in producing targeting systems for the treatment of infectious diseases.

The flexibility of MIPs was further demonstrated in their application against emerging infectious diseases. Specifically, the development of MIPs targeting the Receptor-Binding Domain (RBD) of the SARS-CoV-2 Spike protein showcased their potential as a therapeutic alternative to traditional antibody treatments. These MIPs effectively inhibited the interaction between the viral RBD and the human ACE2 receptor, without cytotoxic effects, positioning them as a promising solution for both therapeutic and prophylactic applications.

In addition, the development of MIP nanoparticles for recognizing the Zika virus Envelope protein (ZIKV-E) demonstrated the capacity of MIPs to combat other viral threats. By using biocompatible and biodegradable materials like sodium alginate and chitosan, stable and non-cytotoxic MIP

nanoparticles were synthesized, showing excellent binding affinity for ZIKV-E. These biopolymer-based nanoparticles offer a rapid, cost-effective, and safe solution for detecting and treating Zika and other viral diseases. Moreover, their use could overcome the limitations of synthetic polymers, paving the way for future advancements and clinical applications. As molecular imprinting technology continues to evolve, focusing on more complex targets and enhanced specificity, future research should aim at optimizing the properties of these biopolymer-based MIPs. Additionally, scaling up production will be crucial for transitioning from laboratory studies to large-scale industrial manufacturing.

Despite the promising potential of MIP-based therapies, challenges such as immunogenicity, toxicity, and clearance rates must be carefully addressed to ensure their safety and effectiveness. Further research into their application in treating viral infections could open new avenues for clinical intervention. Continued investment in MIP research will be essential to unlocking their full potential, establishing them as sustainable, adaptable, and effective tools in the fight against emerging health threats.